Raman spectroscopy study of epitaxially integrated polar GaP on non-polar Si and Ge substrates

By
Rahul Aggarwal
Enrolment No: PHYS03201404005

Raja Ramanna Centre for Advanced Technology
Indore-452013, India

A thesis submitted to the
Board of Studies in Physical Sciences
In partial fulfillment of requirements
for the Degree of

DOCTOR OF PHILOSOPHY
of
HOMI BHABHA NATIONAL INSTITUTE

January, 2021

Homi Bhabha National Institute

Recommendations of the Viva Voce Committee

As members of the Viva Voce Committee, we certify that we have read the dissertation prepared by **Rahul Aggarwal** entitled **"Raman spectroscopy study of epitaxially integrated polar GaP on non-polar Si and Ge substrates"** and recommend that it may be accepted as fulfilling the thesis requirement for the award of Degree of Doctor of Philosophy.

Chairman - **Prof. Aparna Chakrabarti**	Aparna Chakrabarti 19.7.2021
Guide / Convener - **Prof. Alka A. Ingale**	19/7/2021
Examiner - **Prof. Chandrabhas Narayana**	Chandrabhas 19/07/2021
Member 1 (External) - **Prof. G. Ravikumar**	19/07/2021.
Member 2- **Prof. Tarun K. Sharma**	19/07/2021
Member 3- **Prof. M. K. Chattopadhyay**	M K Chattopadhyay 19/07/2021
Member 4- **Prof. Anil K. Sinha**	AKSinha **19/07/2021**

Final approval and acceptance of this thesis is contingent upon the candidate's submission of the final copies of the thesis to HBNI.

I hereby certify that I have read this thesis prepared under my direction and recommend that it may be accepted as fulfilling the thesis requirement.

Date: 20/07/2021

Place: RRCAT, Indore

Prof. Alka A. Ingale

Guide

STATEMENT BY AUTHOR

This dissertation has been submitted in partial fulfillment of requirements for an advanced degree at Homi Bhabha National Institute (HBNI) and is deposited in the Library to be made available to borrowers under rules of the HBNI.

Brief quotations from this dissertation are allowable without special permission, provided that accurate acknowledgement of source is made. Requests for permission for extended quotation from or reproduction of this manuscript in whole or in part may be granted by the Competent Authority of HBNI when in his or her judgment the proposed use of the material is in the interests of scholarship. In all other instances, however, permission must be obtained from the author.

Rahul Ag

Rahul Aggarwal

DECLARATION

I, hereby declare that the investigation presented in the thesis has been carried out by me. The work is original and has not been submitted earlier as a whole or in part for a degree / diploma at this or any other Institution / University.

Rahul Ag

Rahul Aggarwal

List of Publications arising from the thesis

Journal

1. Raman spectroscopy and atomic force microscopy study of interfacial polytypism in GaP/Ge(111) hetero-structures, **R. Aggarwal**, A. A. Ingale and V. K. Dixit, *Appl. Surf. Sci.*, **2018**, 427, 754-762
2. Raman spectroscopy investigation of inter-diffusion in GaP/Ge(111) hetero-structures, **R. Aggarwal**, A. A. Ingale, V. K. Dixit, and V. Sathe, *Superlatt. Microstruct.* **2019**, 125, 190-197
3. Investigations on the origin of strain variation in the zinc-blende phase along the depth of GaP/Si(111) using spatially resolved polarized and wavelength dependent Raman spectroscopy, **R. Aggarwal**, A. A. Ingale and V. K. Dixit, *Appl. Surf. Sci.* **2020**, 514, 145933(1)-145933(6)
4. Elucidating the interfacial nucleation of higher-index defect facets in technologically important GaP/Si(001) by azimuthal angle-resolved polarized Raman spectroscopy, **R. Aggarwal**, A. A. Ingale and V. K. Dixit, *Appl. Surf. Sci.* **2021**, 554, 149620(1)-149620(10)

Conferences

1. Raman mapping of stress distribution in GaP layer grown on Ge(111), **R. Aggarwal**, A. A. Ingale and V. K. Dixit, Proceedings of National conference on Optics Photonics and Synchrotron Radiation for technological applications (OPSR)-2018, **(2018)** 139.

2. Investigation of relative content of zinc-blende and wurtzite phases in GaP/Ge(111) using Raman spectroscopy, **R. Aggarwal**, A. A. Ingale and V. K. Dixit, 63rd DAE-SSPS (2018), AIP conference proceedings 2115 **(2019)** 030322.

Rahul Ag

Rahul Aggarwal

ACKNOWLEDGEMENTS

Undertaking this doctoral programme has been a far-reaching journey for me and arriving at the destination could not have been possible without the guidance and support of many people.

First and foremost, I would like to convey my sincere gratitude and a very big thank to my Guide Dr. Alka A. Ingale whose role in my life has been consequential. My understanding of spectroscopy, developed over the years, rests on foundation she laid. During all these years she always supported me and taught me the importance of self-expression, something I was lacking in my personality. On few occasions she tried extremely hard to push me beyond some of my reservations. This thesis would not have materialized, if she had not shown the faith in me, and granted the conceptual guidance and freedom to explore into the new things.

The very second name which rushes through my brain is of our collaborator, Dr. V. K. Dixit, whose contribution in enriching my understanding of materials has been immense. His valuable conceptual inputs on growth have enhanced the quality and impact of research work presented in this thesis.

I convey my sincere gratitude to all members of the Doctoral committee; Dr. Aparna Pal, Dr. T. K. Sharma, Dr. M. K. Chattopadhyay, Dr. A. K. Sinha, Dr. G. Ravikumar, Dr. S. R. Mishra, Dr. Tapas Ganguly, Dr. Arup Banerjee, Dr. Vinit Kumar, Dr. Anand Moorti, Dr. S. M. Gupta, Dr. M. H. Modi, and Dr. S.B. Roy, who monitored the progress of my research work during these years and provided their valuable suggestions for its betterment. I am also thankful to Dr. Arup Banerjee, Dean-Academic HBNI, RRCAT and Dr. C. P. Paul, Dean Students’ Affairs for their academic and administrative guidance.

I am also very grateful to Dr. Himanshu Srivastava for finding time to perform electron microscopy measurements and helping me in analysis of the data. I also acknowledge the guidance of Shri Mahendra Babu for TEM sample preparation. I am thankful to my colleague Shri Chandrashekhar for his assistance in the lab in many ways during the course of the work.

I am highly thankful to Dr. S. R. Mishra (Head LPAS), Dr. T. K. Sharma (Head MSS), Dr. A. K. Srivastav (Head, LML) and Dr. Tapas Ganguly (Head SUS and ESML), for their support and encouragement during the course of this work.

Finally, I convey my warmest thanks to my family for their persistent and unparalleled love and support during this journey. Accomplishement of this milestone would not have been possible without the support, encouragement and blessings of my family.

Contents

List of Figures

List of Tables

Chapter 6: Conclusion and future outlook

6.1 Summary of the thesis work

The work presented in this thesis is principally motivated with the necessity to understand nature and origin of structural complexities associated with epitaxial integration of polar III-V compound semiconductors on non-polar group IV substrates using a contact-less, nondestructive and relatively expeditious optical technique *i.e.*, Raman spectroscopy. A way further, atomic force microscopy (AFM) is coupled with Raman spectroscopy measurements to explore into the correlation between the vibrational signatures and surface topology of grown epilayer. Furthermore, the results of Raman spectroscopy measurements are also substantiated by high resolution transmission electron microscopy (HRTEM) study of hetero-structures. In order to combine the best of both *i.e.*, III-V compound semiconductors and group IV substrates for technological and economical interests, the hetero-polar epitaxial integration of GaP on Si and Ge is undertaken. The interest in studying the structural and topographical intricacies is driven by the fact that they determine the functional properties of opto-electronic devices based on these technologically significant GaP/Si and GaP/Ge hetero-structures. Effect of polar/non-polar and lattice mismatch, surface energy and growth kinetics on crystalline (structural), physical, physico-chemical and surface properties of these hetero-structures is investigated. The Nucleating (~60 nm) and thick (~820 nm) layer GaP/Ge(111), GaP/Si(111) and GaP/Si(001) hetero-structures for this investigation are grown (Collaborator: Dr. V. K. Dixit, SML, RRCAT) by MOVPE technique using a two step approach. The nucleation layer for each of these hetero-structures is investigated to comprehend the role of nucleating surface on the growth and properties of overgrown thick GaP layer.

In the beginning, GaP epilayer grown on Ge(111) substrate is investigated to delineate the role of large lattice-mismatch and hetero-polar interface in determining the properties of combined structure. The lack of sufficient reports on the study of GaP-on-Ge material combination was another driving force for addressing these hetero-structures first. Until the investigations presented in this thesis, very few reports existed on GaP/Ge hetero-structures, and these reports discuss about the charge transport and electronic band alignment behavior of GaP/Ge hetero-junction [26, 95]. Probing deeper, sub-micron level strain variations in the grown epilayers are discovered and determined by spatially resolved Raman spectroscopy. The origin of additional spectral feature in the TO phonon band, and its correlation with surface topology is investigated by same-site Raman spectroscopy and scanning probe microscopy measurements. It is shown that unique conjunction of AFM and Raman mapping performed on the same sites gives a cutting-edge to the analysis of micro/nano-structured epilayer, while advancing the understanding of the origin of additional phonon mode/s. The inferences of this combinational study effectuated the spatially resolved polarization dependent Raman spectroscopy of the cross-sectional surface of hetero-structures. Spatially resolved polarized measurements enabled the revelation of the coexisting structural allotropes of GaP, with predominance of wurtzite (WZ) phase in proximity to the hetero-junction interface and that of zinc-blende (ZB) phase near the surface. The additional asymmetric feature in TO phonon envelope is shown to stem from the wurtzite phase of GaP. This study based on Raman spectroscopy is the first direct experimental evidence for the occurrence of thermodynamically less favorable wurtzite phase at the GaP/Ge(111) interface.

Furthermore, physico-chemical aspects of GaP/Ge hetero-interface governed by growth kinetics, precursor flow rate and phosphine passivation are investigated. It is observed that Ge-optical phonon mode of underlying substrate of nucleating layer is anomalously broadened and softened. Using wavelength dependent Raman spectroscopy, the cause of this peculiar effect is elucidated in terms of the occurrence of shallow inter-diffused Ge layer (thickness ~20 nm) underneath the GaP epilayer nucleated at ~425°C under high V/III (~1725) ratio. From thermal treatment of hetero-structures and qualitative evaluation of probable mechanisms responsible for inter-diffusion, it is established that vacancy mediated diffusion of phosphorous in Ge substrate give rise to disordered shallow layer of Ge in the close vicinity of GaP-Ge hetero-interface. The result bears particular importance as it signifies that growth challenges for polar/non-polar epitaxy can be resolved by diffusing the phosphorous in group IV substrates for nucleation, and growth of actual structures can be performed after desorption of phosphorous at high temperature.

Following the thread of findings on GaP/Ge(111), we then examined the technologically important and closely lattice-matched GaP/Si(111) material combination wherein hetero-polarity is expected to be the key determinant of the structural aspects of epilayer. Significant spatial non-uniformity in strain and crystalline quality of grown layer is corroborated with variations along the depth of hetero-structure by spatially resolved- and wavelength dependent-Raman measurements from growth surface. Strain-distributed zinc-blende GaP phases are discovered along-the-depth of hetero-structure via nanometer-scale (~100 nm) spatially resolved Raman sampling of cross-sectional surface. These variations in physical properties are analyzed to originate from the deeply co-existing wurtzite phase GaP along the depth of hetero-structure. It is found that the ZB crystal in proximity to WZ phase, having predominance near the hetero-interface, is additionally strained. The co-dominance of wurtzite phase is further substantiated by polarization dependent Raman spectroscopy and AFM study of nucleating layer. The experimental findings manifest the effective implementation of Raman spectroscopic tool for resolving and probing the sub-micron level variation of physical, structural and optical properties *e.g.*, strain, crystal structure, crystalline quality, etc., even along the depth of hetero-structures. In order to delineate the impact of interplay between hetero-polarity and surface energy on nucleation during initial stages of epitaxy, surface properties and polytypic behavior, the work is extended to the investigation of GaP layer grown on (001) oriented Si substrate, another most widely used Si wafer in micro-electronic processing. The emergence of symmetry forbidden TO phonon of GaP is examined using polarize Raman imaging and AFM, which helped in realizing the contribution of non-(001) crystal facets to Raman scattering. The mechanisms responsible for significantly large scattering cross-section of forbidden optical phonon are identified with locally existing higher-index {111} and {112} defect facets using azimuthal angle-resolved polarized Raman spectroscopy. It is revealed that the orientation moderated coalescence of faceted micro/nanosized islands crystallized in nucleating layer results in the structural defects lying on energetically favorable higher-index planes in overgrowth layer. Furthermore, highly intriguing WZ/ZB crystal phase coexistence in the vicinity of GaP-Si(001) interface is inferred via Raman spectroscopy of cross-sectional surface under carefully chosen polarization configurations. It is further substantiated via cross-sectional HRTEM that WZ/ZB stacking faults along nearly indistinguishable $(111)_{ZB}/(0001)_{WZ}$ planes gives rise to forbidden and additional spectral features in the Raman spectra. The novel implementation of angle-dependent polarized Raman spectroscopy elevates this optical technique to a different level for determining the orientation of defect-exposed facets in other advanced semiconductor hetero-structures.

Based on Raman spectroscopy and AFM study of GaP/Si(001), it is ascertained that initial nucleation plays the key role in evolution and bulk propagation of structural defects in the thick epilayer grown atop the nucleated surface. Eventually, the two step MOVPE growth of GaP layer on Si and Ge substrates is undertaken afresh by tweaking the kinetics of the nucleation in controlled manner in a well-thought-out temperature range. Using the understanding developed on earlier hetero-structures, and through the application of Raman spectroscopy, it is shown that nucleation at intermediate (~525°C) temperature results in nearly two-dimensional and high crystalline quality overgrowth layer with reduced density of defect facets and WZ discontinuity in equilibrium ZB phase of GaP. It is understood that the kinetics-controlled mobility and adsorption of adatoms on growth template influences the charge-neutrality along interface and hence the nature of growth and crystalline properties of epilayer.

We could thus resolve the sub-micron length scale defect-structures nucleating at the hetero-polar interface and their propagation into the overgrown epitaxial layer via innovative applications of a fully optical technique *i.e.*, Raman spectroscopy, which was the primary motivation behind this thesis. Crystalline and surface properties of these hetero-structures are shown to follow the thread of interplay between hetero-polarity, lattice mismatch, surface energy and growth kinetics. The information thus extracted from Raman spectroscopy in conjunction with AFM can be used as an immediate feedback for the improvement of hetero-interface/s of the epitaxially integrated structures. The study proposes Raman spectroscopy and its variants as non-invasive, non-destructive and expeditious alternative to time-consuming and cumbersome HRTEM/*in situ* reflection anisotropy spectroscopy measurements for probing the surface and interface properties of such hetero-structures.

6.2 Future work

During the course of work presented in this thesis, the efficacy of a purely optical technique in comprehending the nature of interface-originated defect structures, which control the functional properties of GaP/group-IV hetero-structures, is established. As a logical outcome of the present study, the succeeding experimental work would involve to further establish the one-to-one correspondence between Raman spectroscopy and HRTEM. This will establish Raman spectroscopy as a standard and expeditious methodology to obtain important information on hetero-structures as well as in their evaluation for device fabrication. Another future study could be to ascertain the nature and orientation of interfacial defect-structures in GaP/Si and GaP/Ge hetero-structures grown under kinetically controlled growth conditions, by angle-resolved polarized Raman spectroscopy. This would be beneficial for gaining further insight into the role of nucleation kinetics on surface reconstructions at hetero-polar interface so that hetero-structures with enhanced functionality could be designed.

Summary

The work presented in this thesis is based on Raman spectroscopy study of bulk, crystallographic morphed surfaces and interfaces of polar/non-polar GaP/Si and GaP/Ge hetero-structures, which shows the intriguing physical, structural and physico-chemical properties governed by hetero-polar interface, lattice mismatch, surface energy and growth kinetics. Raman spectroscopy measurements are also facilitated by atomic force microscopy (AFM) to obtain correlation between spectral and topological features, further advancing the comprehensive analysis of micro/nano-structured layers.

The best of both the III-V (*e.g.*, GaP) and group IV (Si, Ge) semiconductors for technological and economical interest can be combined through their epitaxial integration, and tremendous efforts are being made for many years to actualize this. However, the epitaxial integration of high quality III-V compound semiconductors (*e.g.*, GaP) on Si and Ge substrates is challenging due to polar/non-polar interface and lattice mismatch. Therefore, to understand the nature and origin of various complexities associated with hetero-polar integration, the epitaxially grown GaP nucleating (~60 nm) and thick (~820 nm) layers on Ge(111) and Si(111) and Si(001) are investigated using variants of Raman spectroscopy.

Raman and AFM mapping on the same site, spatially resolved polarized Raman measurements from the cross-sectional surface, and wavelength-dependent Raman spectroscopy are employed to resolve the wurtzite (WZ)/zinc-blende (ZB) crystal phase coexistence and atomic inter-diffusion at the hetero-polar interface of GaP/Ge(111) hetero-structures. Using nanoscale (~100 nm) Raman sampling from cross-sectional surface of GaP/Si(111), new and interesting features like

strain-gradient ZB phases of GaP along the depth of hetero-structure are discovered and corroborated to the influence of deeply co-existing WZ phase. Furthermore, the highly intriguing origin of stacking polytypes in GaP/Si(001) hetero-structures is novelly traced back to nucleation and coalescence of higher-index faceted islands using azimuthal-angle resolved polarized Raman spectroscopy. The understanding developed through this gave immediate feedback to address the role of growth kinetics on the nucleation of structural defects, and has led to realization of epitaxial GaP/Si and GaP/Ge hetero-structures, having far superior crystalline and surface quality. Our results provide direct experimental evidence for the intricate relationship between hetero-polarity, surface energy and surface kinetics, and nucleation during initial stages of growth, which govern the nature and origin of structural complexities evolving at the polar/non-polar interface.

Through this study, a novel methodology based on a purely optical technique *i.e.*, Raman spectroscopy has been established to serve as an expeditious, non-invasive and non-destructive alternative to conventionally used high-resolution transmission electron microscopy, for obtaining important information on hetero-structure as well as in its evaluation for device fabrication.

Chapter 1: Introduction

The work presented in this thesis is based on Raman spectroscopy study of bulk, crystallographic morphed surfaces and interfaces of epitaxially integrated polar/non-polar GaP/Si and GaP/Ge hetero-structures, which show the intriguing physical, structural and physico-chemical properties governed by hetero-polar interface, surface energy, lattice mismatch and growth kinetics. In this introductory chapter, first the technological significance of the integration of III-V compound semiconductors on group-IV substrates is discussed to emphasize the importance of material chosen for this thesis work. Thereafter the brief history of Raman spectroscopy, which is the primary technique used in this study, is presented. The challenges associated with epitaxial integration of GaP on Si and Ge substrates are discussed to establish the aim of investigation. Then the motivation behind employing the Raman spectroscopy and atomic force microscopy (AFM) for the study of these hetero-structures is described. The novelties in the present research work, and a brief overview of the thesis, are presented in the last section.

1.1 Integration of III-V semiconductors on group IV substrates: Technological significance

A III-V semiconductor is an alloy composed of trivalent (III) and pentavalent (V) elements, e.g., AlAs, GaAs, InAs, GaP etc. Semiconductor materials of Group III-V elements furnish several advantages over group IV, silicon (Si) and germanium (Ge). This is due to their direct energy bandgap and its tunability by alloying, higher charge carrier mobility, and lower effective masses of the charge carriers [1-5]. The optical band gap energy for the III-V semiconductor materials lie in the range 0.5 eV-3.5 eV. Most of the III-V semiconductors have wide band gap and direct nature of band gap endows them with ability to interact strongly with the photons and having high photon absorption coefficient leading to the large photon conversion efficiency [4]. This renders them their most suitable usage in high-efficiency photovoltaics, advanced lasers, light-emitting diodes, etc. [6-8]. Similarly, Si and Ge are the best semiconductors of choice for the electronics industry. This is because Si is abundant, available at low cost and provides ideal device passivation in terms of the high-quality SiO_2 oxide dielectrics. Further, Si processing and integration technology is mature, established and well-developed. Therefore, Si has been material of choice in semiconductor devices over the years. Also, it is reported that high mobility of electron and holes in Ge facilitate the successful integration of several hetero-junctions on Ge substrate leading to the development of high carrier mobility metal oxide field effect transistor (MOSFETs) [9-12]. In order to combine the best of both the III-V and Si for technological and economical interest, tremendous efforts are being made for many years [13-22]. This unification would benefit from both, the unique optoelectronic functionality of III-V semiconductors and well-established, highly mature and low cost Si, Ge based microelectronic technology.

Technologically important gallium phosphide (GaP), the most mature candidate from the III-V family, possesses a wide bandgap ~2.26 eV (300 K) which implies a wide transparency window in the visible range, and makes it and its alloy compounds as one of the most promising materials for the development of multijunction solar cells [23, 24]. Although, GaP is an indirect band gap semiconductor, its indirect band gap nature can be changed to direct by addition of only ~0.4% of N into GaP [25]. Further, GaP-on-Si combination has additional advantage as GaP features the smallest lattice-mismatch (~0.4%) to Si, which makes GaP a strong contender for low dislocations density and high quality epitaxial integration of GaP on Si. Also, there exist possibilities that defect free GaP/Ge based hetero-structures can find applications in MOSFET based devices [26].

1.2 Raman spectroscopy: Birth, evolution, interests and current scenario

Simply put, Raman spectroscopy is a spectroscopy technique based on inelastic scattering of light by low energy excitations of the medium, predominantly the phonons. Other low energy excitations *e.g.*, magnons, coupled plasmon-phonon, polaritons etc., can also be studied via Raman scattering. Besides absorption, reflection and fluorescence emission of light by matter, the light radiations incident on the medium interact (via electrons) with atomic/molecular vibrations and can be scattered in three ways. When the light from medium is scattered elastically and retains its incident energy, the process is termed as Rayleigh scattering. If the light is scattered inelastically by adding energy to the medium or removing energy from the matter, the process is called Raman scattering. Inelastic loss and gain of energy of the incident radiation undergoing scattering, give rise to Stokes and anti-Stokes Raman scattering effect respectively. Most of the scattered light has same wavelength as incident radiation. However, only a small fraction (10^{-6} to 10^{-8}) of incident light is scattered at different wavelengths. These inelastically scattering radiations, more commonly the Stokes scattered light, are analyzed in Raman spectroscopy.

1.2.1 A timeline of the discovery of Raman Effect

During the sea voyage to Europe in 1921, Indian physicist Sir Chandrasekhara Venkata Raman observed the deep blue color of Mediterranean Sea and Alpine glaciers, and got motivated to discover the origin of this wonderful effect. Unsatisfied with Lord Rayleigh’s explanation of this phenomena and pondering over the matter, Raman and his group in Calcutta performed an extensive series of experiments on scattering of light by many liquids as well as some solids. In his report to *Nature* Sir C.

V. Raman communicated that nearly sixty different common liquids had been studied and all showed the same result that a tiny fraction of the scattered radiation had different color (wavelength) than the incident light [27]. Thereby, C. V. Raman was able to prove that blue color of the sea was result of the scattering of sunlight by water molecules in the air. Most of the earlier experiments by C. V. Raman and his group in IACS Calcutta were performed using sunlight and relied on the visual identification (using filters) of the color of scattered light rather than precise measurement of the wavelength of light [28]. Therefore, in order to evaluate the things quantitatively and to measure the exact wavelengths of scattered radiations, Raman replaced the visual observer with quartz (prism) spectrograph. Using this, the spectrum of scattered light could be photographed (on a photographic plate) along with measurements of its wavelength. For more intense incident radiations, C. V. Raman switched to mercury lamp, as it became commercially available by early 1928 [29]. The quantitative results (*i.e.*, first spectra) using the aforementioned system were published in *Indian Journal of Physics* in March, 1928 [30]. Later in June 1928, the German physicist Peter Pringsheim conducted independent experiments with organic liquids, reproduced the Raman's results successfully, and coined the term Raman Effect. C. V. Raman's contribution to light scattering was recognized and he was awarded the Nobel Prize in 1930 for explaining and demonstrating the phenomenon of light scattering. C. V. Raman had recognized the importance of his discovery, particularly as a convincing proof of quantum theory, and in his Nobel lecture given on December 11, 1930 he stressed "*... and the intensity and state of polarization of scattered radiations enable us to obtain an insight into the ultimate structure of the scattering substanc*e" [31].

By the late 1930s "*Raman Effect became the adopted child of chemistry*" as worded by James Hibben [32] and it was established as a principal technique for non-invasive analysis of organic and inorganic compounds. However, during the world-war II and even after it, Infra-red spectroscopy got ahead of Raman measurements and quickly became the more famous analytical tool for routine operations, due to technological advancement in detection and electronics [29]. The usage of Raman spectroscopy remained in the nascent stage until the development of more advanced measuring instrumentation in early 1960s, as discussed in next sub-section.

1.2.2 A timeline of the technological advancements

The timeline of key events in the gradual evolution of Raman spectroscopy instrumentation, which have led to consequential advancements in field, are discussed in the following. The development of Raman spectroscopy as a full-fledged and contemporary analytical technique was slow until early 1960s due to several reasons [32]. Firstly, the Raman scattering is an inherently weak effect, typically weaker than the incident excitation by 6-8 orders of magnitude, and the challenging task to measure such a weak signal is further complicated by the overwhelming, much stronger Rayleigh scattered light. Secondly, during the early light-scattering studies, Raman spectra were recorded using mercury lamp, prism spectrograph and photographic plate or photomultiplier tube, sometimes requiring few days of exposure to obtain measurable spectra. These complications hindered the evolution of Raman spectroscopy as a technique, in comparison to faster and less expensive infrared spectroscopy. However, these difficulties were overcome to great extent with advent of continuous wave (CW) lasers in early 1960s. The birth of lasers revolutionized the field of Raman spectroscopy in various ways. Also, the discovery of highly intense light source *i.e.*, laser, opened doors for different kinds of linear and non-linear (higher order) Raman spectroscopy. For example, the tuning of a laser (*e.g.*, CW

Argon ion laser) wavelength gave rise to Resonance Raman spectroscopy, particularly advantageous for low volume samples.

Following the advent of laser, the first commercial Raman measurement set-up using the laser source and double pass ruled grating monochromator (Perkin Elmer Raman spectrometer, with photomultiplier tube (PMT)) as dispersing element was introduced in 1966 [33]. More Raman instruments equipped with double monochromators (from Coderg and Spex companies) arrived in 1967-68 [33]. Few years later, a triple stage monochromator (Coderg T800) designed by Delhaye, was also introduced. Thanks to the development of holographic grating in 1972, which produces drastic reduction in stray (Rayleigh) light, the design of Raman spectroscopy instruments and hence the quality of Raman spectra improved significantly. Based on the idea of Delhaye and Migeon in 1966 itself, the coupling of Raman spectrometer to microscope for tight focusing of laser beam at the sample was materialized in 1974 through introduction of commercial instrument, the MOLE [34]. This finally opened the doors for spectroscopy imaging in the field of Raman spectroscopy.

Following the introduction of Raman microscopy system, the next big leap in technological evolution of Raman instrumentation was the development of charged couple device for detection of inherently weak Raman scattered signal. Until the early 1980s, all Raman instruments based on double and triple monochromators made use of the PMT for detection of scattered light. The main drawback of PMT is the large amount of time taken to record the Raman spectrum and low dynamic range. However, the charge couple device (CCD) array with improved sensitivity and high dynamic range used as multichannel detectors, made Raman spectral acquisition possible at much faster speed than the PMT. In row of further advancements, in 1990, *Carrabba et. al.,* reported and demonstrated the utilization of holographic Bragg diffraction filter to suppress the elastically scattered Rayleigh light [35], which consequently enabled the construction of any size monochromator for acquisition of Raman spectra. Taking advantage of holographic Rayleigh line rejection filters and high sensitivity CCD detectors, the birth of single stage (monochromator) Raman spectroscopy microscope followed soon. Due to considerably reduced loss of light in optics of a single monochromator, good quality spectra could now be recorded within seconds to few minutes. Owing to speedy acquisition, high sensitivity and high throughput of single stage Raman instrument, as realized through the introduction of CCD and Rayleigh line filters, further accelerated the potential field of Raman imaging, which is employed to determine the spatial distribution of spectral features. The convergence of various ideas since 1920 successfully resulted in the kind of high quality Raman spectroscopy instrumentation, which has shown huge potential for the research and applications in numerous fields of science and technology, as discussed in next section.

1.2.3 Applicability to various scientific fields: progression over time

With advancement in Raman instrumentation over the last 90 years, the spectroscopy technique has come a long way and achieved the recognition of a prominent and highly effective modern analytical technique. In the initial few years of the discovery, Raman spectroscopy was mostly used by the physicist to study the vibrational and rotational behavior of molecules and relating them to their molecular structure [29]. Chemists also developed the interest in the technique during this time period and started using the Raman effect as leading method for qualitative and quantitative chemical analysis of both organic and inorganic materials. Kohlrausch, who measured the Raman spectra of a great variety of organic compounds in early 1931, was the first person to recognize the potential of Raman Effect in chemical analysis [36].

Uniqueness of Raman spectrum to chemical bonds and molecular symmetry made it an indispensable analytical tool for molecular fingerprinting and studying the changes in chemical bonds, even in a mixture of compounds. Furthermore, the intensity of spectral lines could be related to concentration of individual components in a mixture.

The development of Raman spectroscopy as a technique also impacted the research in biological, medical and pharmaceutical fields. Unlike IR spectroscopy, Raman scattering does not suffer from the interference due to presence of aqueous (water) environment, and hence it is more suitable for biological materials. Label-free and non-destructive detection, using Raman spectroscopy with minimal or no sample preparation, further enhances its applicability to biological and medical fields [37, 38]. Non-invasive *in vivo* Raman measurements can be performed to tap its potential for disease diagnosis, as plenty of diseases stem from the biochemical changes in the cells [39, 40]. Owing to the unique chemical compositions of benign and malignant cancerous tissues, the Raman spectroscopy has been employed to identify and distinguish them [41]. In bio-pharmaceutical industry, Raman spectroscopy is routinely used for identification and quantification of active pharmaceutical ingredients (APIs) and their different polymorphic forms in tablets, due to its molecular and structural specificity [42].

Over the last 30 years, particularly after 1995, Raman spectroscopy has been widely implemented for the studying the behavior of low energy excitations e.g., phonons, coupled plasmon-phonons, magnons etc., in technologically important condensed matter systems, which yielded new information [43]. Raman spectroscopy has invaluably contributed to materials science, particularly to the in-depth evaluation of bulk and low dimensional carbon materials and technologically important semiconductors. The new materials and problems at the cutting edge of materials science are being successfully tackled using Raman spectroscopy. In last few years after the renaissance of graphene, Raman scattering has become an irreplaceable technique for the characterization of 2-D (graphene-related and transition metal chalocogenides) materials [44-48]. Also, the extensive study has been carried out on semiconductor nanowires using Raman spectroscopy and several new phenomena *e.g.*, mixed phase structures associated with these one dimensional structures, have been reported over the last few years [49]. Apart from material identification and routine characterization of semiconductors and other materials, Raman spectroscopy can be effectively employed as a research tool to understand various aspects of material growth *e.g.*, determination of alloy composition and strain, probing the structural imperfections, ascertaining the crystallographic orientations, measurement of temperature and doping concentration etc. Both qualitative and quantitative evaluations are feasible and most of these analyses rely on the phonon spectroscopy. The frequency of these phonons ($\boldsymbol{q}=0$), which are quantized lattice vibrations, lie in the frequency range 10 cm^{-1} - 4000 cm^{-1}. Furthermore, the resonant excitation of the semiconductor near its band gap can enhance the Raman scattered intensity, which is particularly beneficial for the investigation of nano-sized structures.

Raman spectral imaging is another variant of this spectroscopy technique which is relatively a new tool and has enhanced interest in several domains of scientific research and technology. A Raman map is a visual display of variations in the vibrational features at different spatial positions of the sample. This enables the user to quickly observe (visually) how the material parameters change with position. Large areas of the sample can be investigated with sub-micron spatial resolution and its high sensitivity to changes in surrounding, make Raman mapping a highly desirable and versatile technique in semiconductor physics. Depending on sampling of material, even the spectral features over the dimensions smaller than focal spot size can be detected through Raman mapping.

In comparison to other experimental techniques, for instance XRD which provides average information, Raman spectroscopy is a local probe and can determine the variations existing over nano-sized dimensions, in crystalline as well amorphous materials. Even the single particle/nanoscale analysis is possible using Raman spectroscopy. Since Raman spectroscopy is a contact-less and non-destructive technique, it is befitting for *in situ* monitoring and analysis of material growth and physical and chemical processes even at elevated temperature and pressure [50, 51]. Over the years, Raman spectroscopy has proved its indispensability in a vast number of fields, including pharmaceuticals and cosmetics [42, 52], geology and mineralogy [53], *in vivo* biomedical studies [54], environmental sciences [55], bulk and low-dimensional semiconductors [56, 57], archaeology [58], and forensic sciences [59]. In the following, we first discuss the complications associated with hetero-polar integration of III-V compound semiconductor (GaP) on Si and Ge substrates. Afterward, the applicability and versatility of Raman spectroscopy for investigating the bulk, surface and interfacial attributes of the polar/non-polar GaP/Si and GaP/Ge hetero-structures are described. A brief overview of the research work presented in this thesis is provided in the last section.

1.3 Challenges of III-V(GaP)/group IV(Si, Ge) epitaxial integration

In spite of the several years of research, the successful integration of high crystalline quality epitaxial structures of III-V compound semiconductors on Si and Ge substrates is still challenging. This is due to the polar/non-polar (interface hetero-polarity) nature of III-V/Si and III-V/Ge systems, lattice mismatch and diffusion at the hetero-interface [60-66]. Depending on the growth environnment**,** these complexities, can give rise to formation of different kind of defects, e.g. misfit dislocations, stacking faults, twin boundaries and anti-phase domains in the native crystal structure [61, 64, 65, 66-69]. The major problem is caused by hetero-polar interface giving rise to planar structural defects e.g., anti-phase boundaries (APBs). The surface of any substrate is not perfectly planar, and contains mono-atomic height steps [62]. When a non centro-symmetric polar material layer (e.g., zinc-blende phase GaP, GaAs, space group *F4(bar)3m*) is grown epitaxially on a non-polar substrate like Si, Ge containing monoatomic steps, there occurs the formation of wrong III-III (Ga-Ga) or V-V (P-P or As-As) during the growth [70]. This leads to formation of two sub-lattices (two domains), one is Ga terminating and other is P (or As) terminating. The boundary which separates the domains of two different sub-lattices is defined as anti-phase boundary. Depending on growth conditions, the ABPs in epitaxially grown layer may facilitate the formation and propagation of other structural defects. These extended planar defects are electrically active and can have negative impact on charge transport properties due to scattering at such boundaries. Consequently, these defects serve as non-radiative recombination centers, thus degrading the device efficiency. Therefore, the reduction of such structural defects generated at the interface and their propagation into the bulk layer is an issue of key importance. In spite of these constraints, successful epitaxial integration of III-Vs on Si and Ge has been reported by adopting a two step approach, wherein nucleation and actual growth processes are decoupled [71-77]. In this two step procedure, the principal parameters like growth temperature and V/III ratio are optimized in each step. Thin (~few tens of nanometer) nucleating layer grown during the first step of this two step epitaxy plays critical role in the growth of complete structure. In hetero-epitaxy, the crystalline structure of the epilayer is dependent on the way the epilayer constituent atoms react with the surface of the substrate and with one another. Therefore, in the recent time several attempts are made to understand the growth mechanism of GaP nucleating layer grown on Si by *in situ* and *ex situ* measurements [15, 60, 67, 78-80]. Interestingly, it is reported that surface energy of the substrate and the controlled migration of the group III elements are the key to achieve excellent surface and interface properties of the III-V/Si or III-V/Ge hetero-structures [80, 81]. For a given growth kinetics, it is observed that surface energy and hence the surface reconstruction play pivotal role in determining the crystalline properties of the grown layer [82, 83]. However, the surface energy (and hence the surface reconstructions) which influences the initial nucleation of island on substrate depends not only on the chemical and structural components, but also on the orientation of substrate involved. Apart from crystalline properties, the nature of growth mode (for given kinetics) is decided by the interplay between surface energy and polar/non-polar interface [81, 84]. It is therefore essential to understand the role of differences in the inherent material characteristics of the constituents and surface energy (for the given kinetics of growth) on the initial nucleation, morphology and crystalline properties of GaP nucleating and overgrowth layer.

In view of these issues, we have investigated the GaP nucleating (~60 nm) and thick (~820 nm) layer grown on three different substrates, under identical growth conditions, using metal organic vapor phase epitaxy (MOVPE). Growth of the samples has been performed by *Dr. V. K. Dixit, SML (MSS, RRCAT)* [79]. The selection of group-IV substrates is made to ascertain the role of differences in the chemical and structural aspects of the growth template, for given kinetics, in deciding the nucleation and type of growth mode during initial stages, and the nature of structural complexities in GaP layer; (1) impact of non-polar Ge(111) substrate featuring large lattice-mismatch (~4%) for GaP/Ge(111) material combination (2) influence of non-polar closely lattice-matched (~0.4%) Si(111) in GaP/Si(111) hetero-structure and (3) role of substrate crystallographic orientations, having different surface energies viz., Si(001) in GaP/Si(001) hetero-structures [81]. The applicability and significance of Raman and AFM for studying these hetero-structures is discussed in the following section.

1.4 Relevance of Raman spectroscopy to study of GaP/Si and GaP/Ge hetero-structures: Motivation for employing the technique

Apart from growth, the development of modern semiconductor optoelectronic devices involves the timely evaluation of fabricated device using advanced characterization tools. Thanks to its non-destructive nature, Raman spectroscopy, through the investigation of phonon properties, can reliably assess the effect of undesirable perturbations and their spatial non-uniformity on the optical and electronic properties of the as grown hetero-structures and the device based on them. High sensitivity and selectivity to atomic environment and structural arrangement make Raman spectroscopy extremely useful for probing the strain distribution, assessing the crystal imperfections, and determining the local crystal orientations in pseudomorphically grown micro/nano-structured epilayers. Qualitative and quantitative evaluation of strain and its uniformity over the device or wafer-scale is one of the most popular applications in microelectronics, for which Raman mapping is a great tool [85]. Epitaxially grown GaP layer on Si and Ge substrates is expected to undergo biaxial stress. The nature and distribution of strain in GaP epilayer can be determined at sub-micron length scale, using spatially resolved Raman spectroscopy and Raman spectral mapping. Polarization dependence of Raman phonons is extremely sensitive to sub-micron scale disruptions in crystal symmetry (or long range crystal order) due to structural defects, in-plane anisotropy and crystallographic orientations. Therefore, polarization dependent Raman spectroscopy can be used to resolve the spectral features that are indeterminate in unpolarized configuration, and obtain information on the structural defects (e.g., allotropism) and crystal orientations. Depending on the excitation wavelength used, resonance Raman measurements can lead to enhancement of Raman scattered light, which is particularly useful for investigation of nanosized structures. The visible laser excitation at 442 nm which closely resonates with direct band gap (E_g=2.78 eV, 300K) of GaP [86] can be utilized for the investigation of nucleating layer, which is only ~60 nm thick. Furthermore, the wavelength dependent Raman excitation allows the selective examination of different layers in a hetero-structure. Also, the Stoke-antiStoke Raman measurements can be used to determine the sample temperature. Additionally, the atomic force microscopy can be used to evaluate the topographical properties of crystallographic morphed surfaces in micro/nano-structured GaP/Si and GaP/Ge hetero-structures.

As discussed in section 1.3, the hetero-polar epitaxial integration of GaP on Si and Ge substrates suffers from interface-originated structural defects, extending into bulk and consequently impacting the surface properties of grown epilayer. Investigation on surface and interface properties of such hetero-structures has been reported using the *in situ* reflection anisotropy spectroscopy measurements performed at elevated temperatures [80]. However, the polarization information may be affected due to complexity in the reflection geometry of the metal organic vapor phase epitaxy horizontal reactor. Conventionally, some of these informations can be obtained through high resolution transmission electron microscopy (HRTEM)/selected area electron diffraction, which is destructive in nature and provides details over a small spatial region (~100 µm) of the sample. Also, the extraction of interfacial details using HRTEM requires the cross-section sample preparation which is cumbersome and time consuming. Further, X-ray diffraction (XRD) technique poses another problem of inaccurate determination owing to variations existing over nano-sized volumes. Therefore, it is imperative to understand surfaces and interfaces properties of GaP/Si and GaP/Ge hetero-structures over the large spatial region of the samples by an alternative method in timely manner that can be useful for understanding the bulk, surface and interfacial chemistry. Raman spectroscopy, which circumvents the major limitations posed by other conventional experimental methods like XRD and TEM, can serve as an expeditious and non-destructive alternative for sub-micron scale analysis of surfaces and interfaces in these hetero-structures, as briefed in the next section.

1.5 Novelties in the present study and Layout of thesis

In this work, a novel approach towards Raman spectroscopy technique in conjunction with AFM has been employed to investigate the bulk, hetero-junction boundaries and top of the crystallographic morphed surface of epitaxially grown GaP/Si and GaP/Ge hetero-structures. The inferences made from this study are extrapolated to actualize the integration of superior quality GaP/Si and GaP/Ge hetero-structures.

Spatially resolved polarized and unpolarized Raman spectroscopy from cross-sectional surface of cleaved interface of GaP/Si and GaP/Ge hetero-structures is employed innovatively for probing the surfaces and the buried interfaces. This novel methodology has successfully resolved the structural allotropes and strain distribution along the depth of GaP/Si and GaP/Ge hetero-structures**.** Further, the one-of-a-kind application of spatially resolved Raman spectroscopy, presented in this study, has enabled the detection of nanometer scale (~100 nm) variations along the depth of hetero-structure. We have already discussed in previous section that surface energy play an important role in determining the mode of growth, which is additionally complexified by hetero-valent polar/non-polar interface in case of GaP/Si and GaP/Ge hetero-structures. This, depending on growth kinetics, results in crystallographic morphed surface. Azimuthal-angle dependent polarized Raman spectroscopy, which is more exhaustive variant of Raman spectroscopy, is applied creatively to determine orientation of energetically favorable and defect-exposed higher-index crystal facets, and thereby the origin of symmetry forbidden and additional phonons of GaP epilayer. To the best of our knowledge, this is first of its kind study on hetero-structures. Furthermore, wavelength dependent Raman spectroscopy has been employed to selectively excite the different layers, and shallow and deeper region of the same layer in GaP/Si and GaP/Ge hetero-structures, which reveal the extent of disorders and along-the-depth variations in these hetero-structures. Also, the effect of laser irradiation induced heating (if any) on different layers in GaP/Si and GaP/Ge hetero-structure is resolved using Stoke-antiStoke Raman measurements. Apart from this, Raman spectroscopy is uniquely coupled with AFM to reveal more detailed information about the micro/nano-structured GaP epilayers, thus opening new doors in understanding the micro/nano-structured epitaxial layers. We know that AFM provides the 3-D information on surface morphological variations e.g., size and shape of micro/nano-structures and roughness parameters of grown layer. Such variations in the topography of micro/nano-structures could lead to the observance of symmetry forbidden (for scattering from particular one type of crystallographic planes) phonon modes in Raman spectra. This occurs due to allowed scattering contributions from crystallographic planes other than the one which is expected. Therefore, Raman spectroscopy measurements are performed in the same region of the material whereat

AFM has been performed, to extract out nearly the one-to one corroboration between surface topology and spectral features of the micro/nano-structured GaP epilayer.

In the following chapters, the results on Raman spectroscopy study of GaP/Si and GaP/Ge hetero-structures are presented in a way that they carry and weave the impact of hetero-polar interface, lattice mismatch, surface energy and growth kinetics on the bulk, surface and interfacial properties of these hetero-structures. Our results provide direct experimental evidence for the intricate relationship between hetero-polarity, surface energy and surface kinetics and initial nucleation, which govern the nature and origin of structural complexities evolving at the polar/non-polar interface. Chapter 2 describes the experimental foundation of primarily the Raman spectroscopy and AFM, which have been employed to obtain the results presented in this work. Chapter 3 discusses about the influence of large lattice-mismatch and hetero-polar interface on surface and crystalline properties of GaP/Ge(111) hetero-structures. The variations in spectral features of additional phonon modes of GaP epilayer is uniquely corroborated to topological and structural changes across the crystallographic morphed surface and the cross-sectional surface respectively. The dominance of wurtzite (WZ) crystal phase of GaP coexisting with zinc-blende (ZB) phase at GaP-Ge hetero-junction interface is discovered and shown to be the origin of additional phonon mode in Raman spectra. Furthermore, the anomalous disordering of the shallow layer (~20 nm) of Ge substrate near the interface is revealed and explicated in terms of the kinetics-, surface passivation- and V/III ratio- driven inter-diffusion of phosphorous across the hetero-interface. Chapter 4 builds on the understanding developed in chapter 3 and further explores into the interfacial nucleation of structural defects in closely lattice-matched GaP/Si hetero-structures, wherein the major contribution is expected to come from polar/nano-polar mismatch.

The significant spatial non-uniformity in strain and crystalline quality of micro-structured GaP epilayer, as noticed in Raman spectra from growth surface of GaP/Si(111), is shown to originate from the presence of strain distributed zinc-blende phases of GaP along the depth of hetero-structure. These physical variations are correlated with the deeply co-existing wurtzite crystal phase of GaP along the depth of GaP/Si(111). Chapter 4 further discusses the impact of substrate orientation on nucleation during initial stages of growth, surface topology, and formation of stacking polytypes in GaP/Si(001) hetero-structures. The interfacial evolution of epitaxial islands terminating on energetically favorable higher-index crystal facets and their coalescence during the overlayer growth is revealed to result in symmetry forbidden phonon mode and highly intriguing WZ/ZB allotropes along the $(0001)_{WZ}/(111)_{ZB}$ directions. The role of initial nucleation in controlling the crystalline quality of overgrowth layer is brought as a natural consequence. This understanding facilitated the improvisation in the structural properties of these hetero-structures by tweaking the nucleation kinetics as discussed in the next chapter. Chapter 5 builds on the results presented in Chapter 4, and discusses the attempts to achieve the growth of defect-reduced GaP/Si and GaP/Ge hetero-structures by applying the Raman spectroscopy. Chapter 6 summarizes the principal findings of the work presented in this thesis and also emphasizes the future experimental plans based on the present study.

Chapter 2: Experimental Techniques

This chapter primarily discusses the necessary theoretical-cum-experimental foundation of Raman spectroscopy and atomic force microscopy (AFM), and the details of associated experimental set-ups used to obtain the results presented in this thesis. We first illustrate the configuration of GaP/group-IV hetero-structures, which have been investigated in the present thesis work. Macroscopic and microscopic formulations for Raman scattering by phonons in semiconductors are briefly discussed, along with the the conceptual discussion on insightful variants of Raman spectroscopy such as resonant Raman and polarization dependent Raman scattering. Thereafter, the working principles and concepts of AFM and cross-sectional transmission electron microscopy (TEM) are described. This is followed by the detailed description of major experimental set-ups used for Raman spectroscopy and AFM measurements. The chapter then presents a concise overview of the operating methodology of Raman & AFM measurements at the same site, as implemented for the analysis of micro/nano-structured GaP epilayers.

2.1 Materials under investigation: GaP/Si and GaP/Ge

The GaP epilayers are grown on group-IV Si and Ge substrates in a horizontal metal organic vapor phase epitaxy (MOVPE) reactor AIX-200. A two-step approach is adopted for the MOVPE growth of hetero-structures. In this two step process, first GaP nucleating layer of thickness ~60 nm with high V/III ratio ~1725 is grown at low temperature ~425°C. This is followed by the growth of GaP layer of thickness ~760 nm at 770°C with V/III ratio ~100 so that total thickness is ~820 nm [79]. As discussed in chapter 1, the crystalline quality of the thick layer grown in second step and hence the performance of the devices based on these hetero-structures, depends critically on the growth of nucleating layer [15, 79]. Therefore, it becomes fundamentally important to understand the role of nucleation layer in determining the crystalline properties of the overgrown thick layer. Keeping this in mind, nucleating layer (~60 nm) hetero-structure is also grown separately and investigated. Figure 2.1 shows the configuration of nucleating and thick layer hetero-structures.

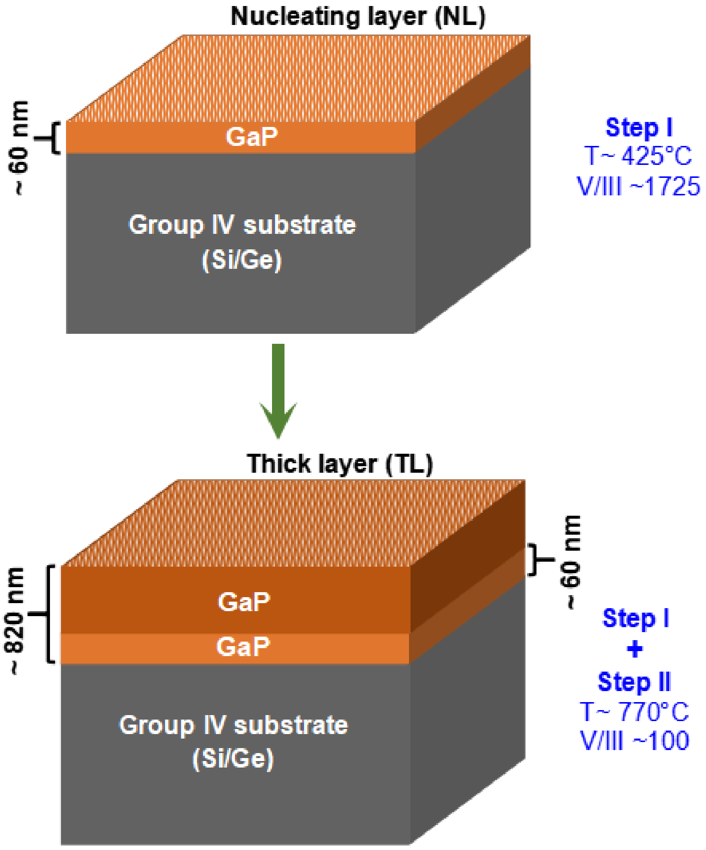

Fig. 2.1. *Schematic diagram illustrates the configuration of nucleating and thick layer GaP/group-IV hetero-structures.*

Following this approach, GaP nucleating and thick layers are grown on Ge(111), Si(111) and Si(001) substrates. The samples used in this thesis work have been grown by *Dr. V. K. Dixit*, SML (MSS, RRCAT). The details of MOVPE growth are presented in Appendix-A.

In the first chapter, we discussed how Raman spectroscopy technique, over the years, has established itself as an invaluable tool for studying the material properties and also described its relevance and applicability to study of semiconductor hetero-structures. However, effective Implementation of the Raman spectroscopic tool and in-depth analysis of spectral features rest on the building-blocks of theoretical concepts, as described in the next section.

2.2 Raman spectroscopy: Concept, theory and insightful variants

Most of the light incident on a material is either transmitted absorbed or reflected following the laws of refraction and reflection. However, a fraction of light is scattered by the medium in all the directions. It originates from the fluctuations in the properties of the medium. The outgoing scattered radiation may have the same frequency as the incident radiation termed as the elastic Rayleigh scattering or may differ in energy giving rise to inelastic scattering. Fluctuations in the density of the medium through which light traverses could be due to vibrations of the atoms of the medium about their equilibrium position. These are the example of scatterers where outgoing scattered light comes out at different energy (higher or lower) than the incident radiation [87]. This kind of inelastic scattering is termed as the Raman scattering and has become an extremely useful tool to study the semiconductors, especially those having nanoscale dimensions. There are two approaches by which the theory of inelastic scattering of light by lattice vibrations of crystal can be treated: macroscopic (classical) and microscopic (quantum) theories. In the following we discuss the macroscopic and microscopic theory of light scattering (Raman scattering) by lattice vibrations in the solids.

2.2.1 Macroscopic (Classical) theory of Raman scattering by lattice vibrations

Macroscopic theory of Raman scattering is constructed on the idea that electromagnetic radiation incident on a medium induces the time dependent dipole moment in each atom and these individual atomic dipole moments (considered in classical theory) combine to form a macroscopic polarization vector [87]. The scattered light is radiated by the oscillatory macroscopic polarization treated through the Maxwell equations. When a electromagnetic filed $\boldsymbol{E}$ is incident on a medium it induces a polarization $\boldsymbol{P}(\boldsymbol{r}, t)$, represented by [87]:

$$\boldsymbol{E}(r,t) = \boldsymbol{E}_i(\boldsymbol{k}_i, \omega_i)\cos(\boldsymbol{k}_i.\boldsymbol{r} - \omega_i t) \quad \text{and} \quad \boldsymbol{P}(r,t) = \boldsymbol{P}(\boldsymbol{k}_i, \omega_i)\cos(\boldsymbol{k}_i.\boldsymbol{r} - \omega_i t) \tag{2.1}$$

where $\boldsymbol{k}_i$, ω_i and $\boldsymbol{E}_i(\boldsymbol{k}_i, \omega_i)$ are the wave-vector, frequency and amplitude of the incident field. The frequency and wave vector of the induced polarization are same as the incident field. The amplitude of the induced polarization $\boldsymbol{P}_i(\boldsymbol{k}_i, \omega_i)$ in terms of the electrical susceptibility χ_{jk} and the incident field can be written as [87]:

$$\boldsymbol{P}(\boldsymbol{k}_i, \omega_i) = \chi(\boldsymbol{k}_i, \omega_i)\boldsymbol{E}_i(\boldsymbol{k}_i, \omega_i) \tag{2.2}$$

At a finite temperature of the medium, there are fluctuations in the susceptibility of the medium due to thermally excited atomic vibrations. The atomic vibrations in crystalline material are quantized into phonons and the atomic displacement $\boldsymbol{u}(\boldsymbol{r}, t)$ associated with a phonon can be represented by a plane wave:

$$\boldsymbol{u}(\boldsymbol{r}, t) = \boldsymbol{u}(\boldsymbol{q}, \omega_{ph})\cos(\boldsymbol{q}.\boldsymbol{r} - \omega_{ph} t) \tag{2.3}$$

where $\boldsymbol{q}$ and ω_{ph} are the wave vector and frequency of the lattice vibration. These lattice vibrations will modify the electrical susceptibility 'χ'. Under adiabatic approximation, it can be assumed that the electronic frequencies which determine the 'χ' are much larger than the lattice vibration frequency ω_{ph}. Hence 'χ' can be taken to be a function of atomic displacement $\boldsymbol{u}$ $(\boldsymbol{r}, t)$. Since the amplitudes of lattice vibrations at room temperature are small compared to the lattice constant, one can expand the change in susceptibility due to lattice vibrations as Taylor series in $\boldsymbol{u}$ $(\boldsymbol{r}, t)$ about the equilibrium position $\boldsymbol{u}= 0$, and retain the terms up to first order only. Only two terms are saved in equation (2.1) and we get [87]:

$$\boldsymbol{P}_0(\boldsymbol{r},t) = \chi_0 \boldsymbol{E}_i(\boldsymbol{k}_i,\omega_i)\cos(\boldsymbol{k}_i.\boldsymbol{r} - \omega_i t) \tag{2.4}$$

$$\begin{aligned}\boldsymbol{P}_{\mathrm{ind}}(\boldsymbol{r},t,\boldsymbol{u}) = \frac{1}{2}\left(\frac{\partial \chi}{\partial \boldsymbol{u}}\right)_{\boldsymbol{u}=0} \boldsymbol{u}(\boldsymbol{q},\omega_{ph})\boldsymbol{E}_i(\boldsymbol{k}_i,\omega_i)\times \\ \left[\cos\{(\boldsymbol{k}_i - \boldsymbol{q}).\boldsymbol{r} - (\omega_i - \omega_{ph})t\} + \cos\{(\boldsymbol{k}_i + \boldsymbol{q}).\boldsymbol{r} - (\omega_i + \omega_{ph})t\}\right]\end{aligned} \tag{2.5}$$

where χ_0 is the electrical susceptibility of the medium without any perturbation i.e., fluctuations. $\boldsymbol{P}_0(\boldsymbol{r}, t)$ is the polarization vibrating at same frequency and phase as the incident radiation and corresponds to the elastic scattering of light called Rayleigh scattering. The other term $\boldsymbol{P}_{\boldsymbol{ind}}(\boldsymbol{r}, t, \boldsymbol{u})$ is the polarization induced by the lattice vibrations and is related to Raman scattering. The induced polarization term $\boldsymbol{P}_{\mathrm{ind}}(\boldsymbol{r}, t, \boldsymbol{u})$ consists of the Stokes shifted wave with wave vector $\boldsymbol{k}_s =(\boldsymbol{k}_i - \boldsymbol{q})$and frequency $\omega_s= (\omega_i - \omega_{ph})$ and the anti-Stokes wave with wave vector $\boldsymbol{k}_{as}= (\boldsymbol{k}_i + \boldsymbol{q})$ and frequency $\omega_{as} = (\omega_i + \omega_{ph})$. Therefore, in Raman scattering process we observe two scattered radiations, one is Stoke shifted wave and other is Anti-Stoke shifted wave. In the scattering event, the momentum conservation law and energy conservation law hold and are given by:

$$\boldsymbol{k}_i = \boldsymbol{k}_s \pm \boldsymbol{q} \tag{2.6}$$

$$\omega_i = \omega_s \pm \omega_{ph} \tag{2.7}$$

Where subscript '*i*' and '*s*' stands for incident and scattered radiation and the sign '±' refers to '+' for stokes scattering and '-' for anti-Stokes scattering. This implies that in Stokes process a phonon is created while in anti-Stokes process a phonon is annihilated. Raman scattering experiments are performed with visible incident radiations having typical frequency ~10^{15} Hz and wave-vector ~10^7m^{-1}. Frequency of lattice vibrations studied is much smaller ($\omega_{ph}<<\omega_i$) than the frequency of incident radiation. Therefore, conservation of wave-vector in a scattering event necessitates that the wave-vector of phonon involved must be of the similar order ~10^7m^{-1}. Its magnitude is much smaller than that of Brillouin zone boundary wave-vector and thus long wavelength phonons near $|\boldsymbol{q}| \approx 0$can be excited in first order Raman scattering. The intensity of Raman scattered light is determined by the induced polarization term $\boldsymbol{P}_{ind}$. The $\boldsymbol{P}_{ind}$ term is same for both Stokes and anti-Stokes scattering except the difference in their frequencies and wave-vectors. Considering that the polarization of incident and scattered light are '$\boldsymbol{e}_i$' and '$\boldsymbol{e}_s$' respectively, the scattered intensity 'I_s' for first order Raman scattering is expressed as [87]:

$$I_s \propto \left|\boldsymbol{e}_i \, . \, R . \boldsymbol{e}_s\right|^2 \qquad \text{wit h} \qquad R = \left(\frac{\partial \chi}{\partial \boldsymbol{u}}\right)_{\boldsymbol{u}=0} \hat{\boldsymbol{u}}(\boldsymbol{q}, \omega_{ph}) \tag{2.8}$$

The prefactor appearing in equation (2.5), which has come into (2.8) also, is defined as the Raman tensor 'R'. Since 'R' is obtained by the contraction of a vector '$\boldsymbol{u}$' with the derivative of susceptibility 'χ' with respect to '$\boldsymbol{u}$', it is a second rank tensor. Raman scattered intensity depends on the polarization of incident and scattered radiation, and therefore the equation (17) can be used to determine the Raman modes of given crystalline structure, participating in scattering. In other words, this signifies that scattered intensity either vanishes or remain non-zero for certain choices of polarizations. Polarization dependent Raman spectroscopy is an effective and extremely informative variant of Raman spectroscopy, and we have employed it innovatively to extract information on structural aspects of GaP/group-IV hetero-structures.

2.2.2 Polarization dependent Raman spectroscopy

Depending on the crystal symmetry of the material, symmetry of phonon modes involved in the scattering, the Raman scattered intensity (equation (17)) vanishes for certain choices of the scattering geometry and the incident ($\boldsymbol{e}_i$) and scattered ($\boldsymbol{e}_s$)polarizations. These so-called Raman selection rules (RSRs) dictate whether an optical phonon mode at Brillouin zone center is active or not in the in the first-order Raman scattering. The work presented in this thesis is primarily based on Raman spectroscopy investigation of epitaxially grown micro-structured GaP/Ge(111), GaP/Si(111) and GaP/Si(001) hetero-structures. Therefore, it becomes pertinent to evaluate and discuss the RSRs for scattering from (001) and (111) crystallographic planes.

Pure bulk GaP adopts the more stable zinc-blende (ZB) crystal structure (point group T_d and space group *F4(bar)3m)* which consists of two interpenetrating FCC sub-lattices displaced from each other along the body diagonal by one-quarter length of that diagonal. One of the two sub-lattices is occupied by Ga atoms and other by P atoms. Therefore, we determine the Raman tensors and hence RSRs for a zinc-blende type crystal structure. Raman tensors in the main crystallographic axes system $x \equiv [100]$, $y \equiv [010]$ and $z \equiv [001]$ are [87]:

$$R(x) = \begin{pmatrix} 0 & 0 & 0 \\ 0 & 0 & d \\ 0 & d & 0 \end{pmatrix}, \; R(y) = \begin{pmatrix} 0 & 0 & d \\ 0 & 0 & 0 \\ d & 0 & 0 \end{pmatrix}, \; R(z) = \begin{pmatrix} 0 & d & 0 \\ d & 0 & 0 \\ 0 & 0 & 0 \end{pmatrix} \qquad (2.9)$$

R(x), R(y) and R(z) represent the Raman tensors for optical phonons polarized along crystallographic directions *x*, *y* and *z* respectively. For polar semiconductor crystals like GaP, GaAs, optical phonon is split into a doubly degenerate transverse optical (TO) phonon and a longitudinal optical (LO) phonon, having different frequencies. In equation (2.9), parameter *d* represents the non-zero Raman susceptibility tensor element. The element *d* takes different values for TO and LO phonons because in addition to deformation-potential mechanism for TO, LO phonon can scatter light through its macroscopic electric field called Frohlich electron-phonon interaction [87].

Therefore, the different tensor elements for TO and LO phonons are represented by ‘d_{TO}’ and ‘d_{LO}’ respectively. As employed in this study, the RSRs are derived in back-scattering geometry configuration, wherein the wave-vectors of incident ($\mathbf{k}_\mathrm{i}$) and scattered photons ($\mathbf{k}_s$) are in opposite directions. Depending on the orientation of Si and Ge substrate used for MOVPE growth of GaP layers and analysis presented in following chapters of this thesis, the polarized RSRs (in back-scattering geometry) for different crystallographic bases are calculated. Table 2.1 summarizes the so-obtained RSRs for optical phonons of ZB crystal structure. A particular scattering configurations in Table 2.1 is represented by the $\mathbf{k}_\mathrm{i}(\mathbf{e}_i, \mathbf{e}_s)\mathbf{k}_s$, knownas Porto notation [87]. The details of derivations of these RSRs under different polarization configurations are presented in Appendix-B.

Table 2.1. *Raman selection rules (RSRs) for* $\mathbf{q}\approx 0$ *optical phonons of the ZB type crystal in different crystallographic bases*

Crystallographic basis: ($x \equiv [100]$, $y \equiv [010]$ and $z \equiv [001]$)		
Scattering configuration	TO phonon	LO phonon
$z(xx)\bar{z}$ and $z(yy)\bar{z}$	forbidden	forbidden
$z(xy)\bar{z}$	forbidden	allowed
Crystallographic basis: ($X \equiv [1\bar{1}0]$, $Y \equiv [110]$ and $Z \equiv z \equiv [001]$)		
Scattering configuration	TO phonon	LO phonon
$Z(XX)\bar{Z}$ and $Z(YY)\bar{Z}$	forbidden	allowed
$Z(XY)\bar{Z}$	forbidden	forbidden
Crystallographic basis: ($X_1 \equiv [1\bar{1}0]$, $Y_1 \equiv [11\bar{2}]$ and $Z_1 \equiv [111]$)		
Scattering configuration	TO phonon	LO phonon
$Z_1(X_1X_1)\bar{Z}_1$ and $Z_1(Y_1Y_1)\bar{Z}_1$	allowed	allowed
$Z_1(X_1Y_1)\bar{Z}_1$	allowed	forbidden

Raman selection rules in Table 2.1 clearly reflect the behavior of optical phonons of a ZB crystal under different polarization configurations. Therefore, the Raman active phonon modes, which are directly linked to crystal structure and symmetry, can be unambiguously attributed by controlling the polarizations of incident and scattered light. Also, the spectral features that remain undetermined in unpolarized configuration can be resolved [49] through polarized Raman scattering. Furthermore, the disruption of the crystal symmetry due to the structural defects in crystal is reflected in the polarization dependence of Raman modes. These strengths of polarized Raman spectroscopy have been innovatively utilized in revelation and analysis of the nano-size scale structural defects in GaP/Si and GaP/Ge hetero-structures. Polarization dependence can be further augmented to azimuthal angle-dependent (polar) Raman spectroscopy for the more insightful evaluation of crystal growth, as discussed in next sub-section.

2.2.3 Azimuthal angle-dependent polarized Raman spectroscopy

As described in previous section, the polarization dependent behavior of long wavelength optical phonons directly reveals the crystal symmetry; however the comprehensive information on in-plane crystal anisotropy and crystallographic orientations can be obtained by azimuthal angle-dependent polarized Raman spectroscopy. In semiconductor micro-electronics, particularly the nano-electronics, determination of crystallographic orientations is of utmost importance since various physical, chemical and electronic properties depend on crystal orientation. In the azimuthal angle-dependent polarized Raman measurements, the in-plane polarizations are rotated through various angles and their dependence on scattering cross-section of different phonon modes in Raman spectra are evaluated. In order to obtain the azimuthal dependence of Raman scattered intensity, the incident ($\boldsymbol{e_i}$) light polarization is rotated by using a half wave plane in its path and scattered ($\boldsymbol{e_s}$) light polarization is selected by an analyzer in the output, in a way that these polarizations either remain parallel ($\boldsymbol{e_i} \parallel \boldsymbol{e_s}$) or perpendicular ($\boldsymbol{e_i} \perp \boldsymbol{e_s}$) to each other. The similar arrangement can also be realized by keeping the incident polarization direction fixed, and rotating the sample around a fixed optical axis. The variations in the scattering cross-section of Raman phonons are registered against the different azimuthal angles, resulting in the polar Raman plots. The so-obtained polar Raman plots in parallel and cross polarization configurations can determine the crystallographic directions of even nano-sized structures. This method has been creatively implemented by us for discovering the higher-index (non-(001)) defect faceting in micro/nano-structured GaP/Si(001) hetero-structures.

Using the mathematical expression for power radiated by oscillating dipole [88] and combining it with expression (2.8), the intensity of the scattered light per unit solid angle can be further expressed as [87]

$$I_s \propto (\omega / c)^4 \left| \boldsymbol{e}_i \, . \, R \, . \boldsymbol{e}_i \right|^2 \tag{2.10}$$

The macroscopic (classical) treatment of Raman scattering developed so far rightly predicts the existence of Stokes and anti-Stokes components in the scattered light. However, one shortcoming of classical theory is that it gives incorrect ratio of stokes and anti-Stokes lines. The ratio of intensity of two components is:

$$\frac{I_s}{I_{as}} \propto \frac{\omega_s^4}{\omega_{as}^4} = \frac{(\omega_i - \omega_{ph})^4}{(\omega_i + \omega_{ph})^4} \tag{2.11}$$

This ratio is always less than unity, whereas it has been observed experimentally that the intensity of stokes line is always larger than that of the anti-stokes component. This discrepancy can be removed by quantum (microscopic) theory of Raman scattering, discussed in next section.

2.2.4 Microscopic (Quantum) theory of Raman scattering

Microscopic theory of Raman scattering is based on the quantization of electron radiation interactions and electron lattice interactions. In quantum mechanical treatment, electromagnetic field and lattice vibrations are quantized, and the material (crystal) is treated quantum mechanically. The total Hamiltonian (H_T) of the system consists of three parts [89, 90]:

$H_T = H_R + H_{scm} + H_{ER}$

H_R= Hamiltonian of incident and scattered radiation field

H_{scm}= Hamiltonian of the scattering medium = $H_o + H_{EL}$

H_{ER}= Hamiltonian of the electron radiation interaction (H_{ER})

H_o = Hamiltonian for elementary excitations of the medium

H_{EL} = Hamiltonian corresponding to electron-lattice vibration interaction

The interaction part of the total Hamiltonian is of relevance here as the transition rate between the initial and final states for Raman scattering process is given by the matrix elements of the interaction parts of the Hamiltonian. The interaction Hamiltonian can be divided into two parts: 1) electron-radiation interaction Hamiltonian 'H_{ER}' and 2) electron-lattice interaction Hamiltonian 'H_{EL}'.

(1) H_{ER}: This term describes the interaction of electromagnetic field with the electrons of the medium. The radiation field is considered in the electronic Hamiltonian by making the following replacement:

$$\boldsymbol{p}_j \rightarrow \boldsymbol{p}_j + e\boldsymbol{A}(\boldsymbol{r}_j) \qquad (2.12)$$

Here, '$\boldsymbol{p}_j$' is the momentum operator of jth electron and '$\boldsymbol{r}_j$'is its position vector. $\boldsymbol{A}(\boldsymbol{r}_j)$ is the vector potential operator of the electromagnetic field at position '$\boldsymbol{r}_j$' of the electron in the scattering medium. Making this replacement, applying the Coulomb gauge condition, $\nabla.\boldsymbol{A} = 0$, and separating the H_{ER} part:

$$H_{ER} = \sum_j \frac{e\boldsymbol{A}(\boldsymbol{r}_j).\boldsymbol{p}}{m} + \sum_j \frac{e^2\boldsymbol{A}(\boldsymbol{r}_j).\boldsymbol{A}(\boldsymbol{r}_j)}{2m} = H'_{ER} + H''_{ER} \tag{2.13}$$

where '*e*' and '*m*' are the charge and mass of electron respectively. Quantization of electromagnetic field give rise to the following expression for vector potential '$\boldsymbol{A}(\boldsymbol{r_j})$' at the position vector '$\boldsymbol{r_j}$' in the scattering medium:

$$\boldsymbol{A}(\boldsymbol{r}_j) = \sum_k \left(\frac{\hbar}{2 \in_0 \eta^2 V \omega_k} \right)^{1/2} \left[a_{\boldsymbol{k}} e^{i\boldsymbol{k}.\boldsymbol{r}_j} + a_{\boldsymbol{k}}^{+} e^{-i\boldsymbol{k}.\boldsymbol{r}_j} \right] \tag{2.14}$$

$$\text{with} \quad a_{\boldsymbol{k}} \left| n_{\boldsymbol{k}} \right\rangle = \sqrt{n_{\boldsymbol{k}}} \left| n_{\boldsymbol{k}} - 1 \right\rangle \quad \text{and} \quad a_{\boldsymbol{k}}^{+} \left| n_{\boldsymbol{k}} \right\rangle = \sqrt{n_{\boldsymbol{k}} + 1} \left| n_{\boldsymbol{k}} + 1 \right\rangle \tag{2.15}$$

where '*V*' is the scattering medium volume, '$\omega_{\boldsymbol{k}}$' is the frequency of the photon of wave vector '***k***' and polarization direction '$\varepsilon_{\boldsymbol{k}}$'. In above equation '$\eta$' is the refractive index of the scattering medium. Creation and annihilation operators for a photon with wave vector ***k*** (and energy $\hbar\omega_k$) are 'a_k^{+}' and 'a_k' respectively. '$n_{\boldsymbol{k}}$' is the total number of photons with wave vector ***k***.

2) Electron-lattice interaction (H_{EL}): In quantum mechanics, the vibrational modes of the lattice are quantized and are represented by normal coordinate operators. The quantum of vibrational mode is called phonon. The lattice displacement produced by the excitation of a phonon perturbs the periodic potential experienced by the electrons. This gives rise to electron-lattice interaction, which plays the important role in the microscopic scattering. This interaction in a lattice can be divided into two parts: short range interaction and long range interaction. The short range interaction (present in the homopolar crystals like silicon) arises from the effect of the atomic displacement on the periodic potential energy of electron. Its strength depends on the relative displacement of the two atoms (diatomic lattice) in the primitive cell. The long range interaction (present in the polar III-V semiconductors) arises due to the interaction of

electrons with the macroscopic electric field of the lattice vibrations. The longitudinal optical phonon of the crystal has an associated electric field.

In scattering experiments, the quantity of importance is the scattering cross section. The scattering cross-section is defined as the rate of removal of energy from the incident beam, due to scattering process, into solid angle dΩ, in volume V for scattered radiation frequency lying between ω_S and $\omega_S + d\omega_S$ divided by the intensity of the incident beam. Mathematically it can be expressed as [90]:

$$\frac{d^2\sigma}{d\omega_s d\Omega} = \frac{\hbar\omega_i}{\tau\, I_i} = \frac{\eta_I \upsilon}{n_i c} . \frac{1}{\tau} \tag{2.16}$$

where '$\hbar\omega_i$' is the energy of the incident photon, 'I_i' is the mean intensity of the incident beam and '$1/\tau$' is the rate of transition (transition probability per unit time) between initial and final states. 'n_i' is the number of incident photons in the scattering volume υ. Raman scattering of photon changes the lattice vibrational state of the material, but the electronic state remains unchanged at the end of the scattering event, although the virtual intermediate states in the process involve the excitation of the electrons. Raman scattering process involves three matrix elements, one from the electron lattice interaction (H_{EL}) and two matrix elements for electron radiation (H_{ER}) interaction. Therefore, the transition rate for the Raman scattering is given by third order time-dependent perturbation theory. In first order Raman effect, a photon of frequency 'ω_i' is annihilated, a long wavelength optical phonon of frequency ω_{ph} is created (Stokes) or destroyed (Anti-Stokes), a photon of frequency 'ω_s' is emitted. These three transitions can occur in any time order and hence give rise to six types of processes as shown in Fig. 2.2. The transition rate for Stokes process, obtained by summing the individual contributions of six Feynman diagrams, will be of the form [89, 90]:

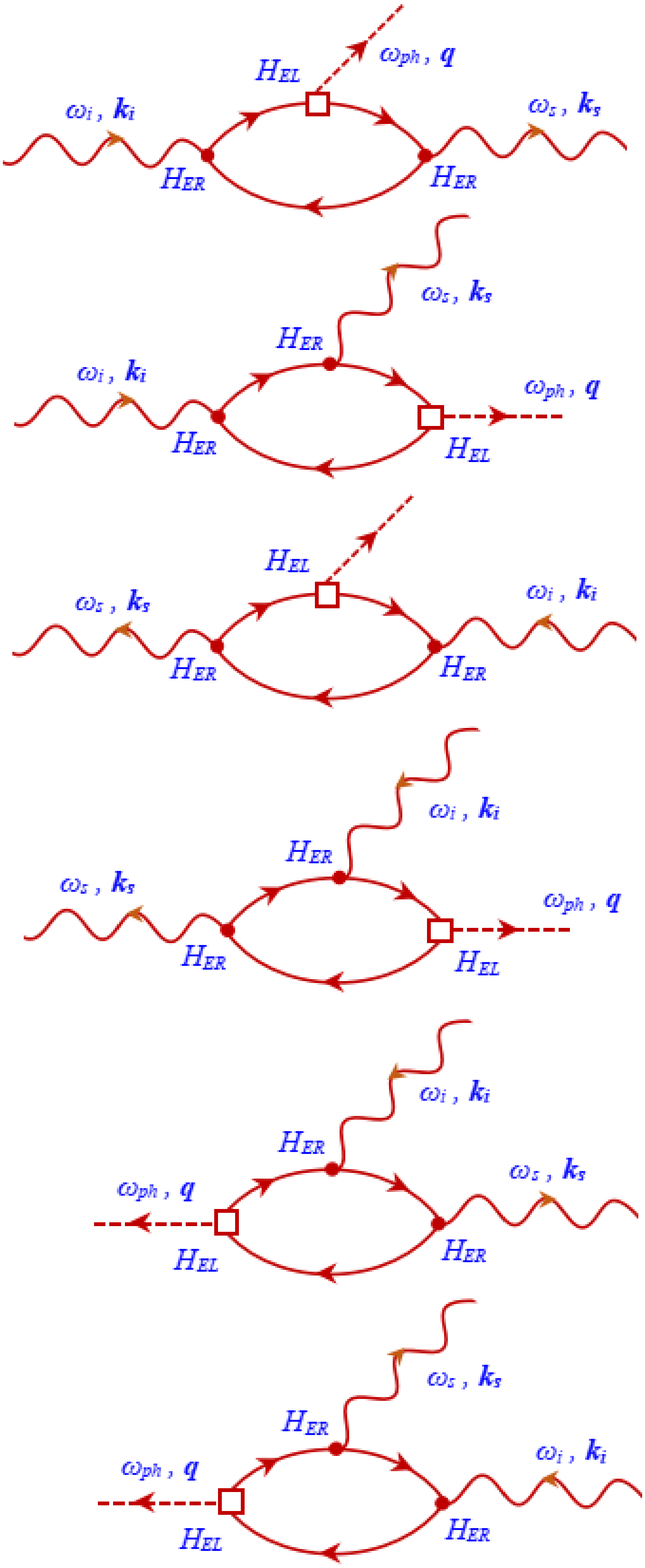

Fig. 2.2. *Feynman diagrams for six type of scattering processes which contribute to the first order Stokes Raman scattering*

$$
\begin{aligned}
\frac{1}{\tau} \propto \sum_{\boldsymbol{k}} \Bigg| \sum_{\alpha,\beta} & \frac{\boldsymbol{e}_s.\boldsymbol{p}_{0\beta}(-\boldsymbol{k}_s)\langle \beta, n_i-1, 0, n_{ph}+1 | H_{EL} | \alpha, n_i-1, 0, n_{ph}\rangle \boldsymbol{e}_i.\boldsymbol{p}_{\alpha 0}(\boldsymbol{k}_i)}{(\omega_\beta-\omega_s)(\omega_\alpha-\omega_i)} \\
& + \frac{\langle 0, n_i-1, 1, n_{ph}+1 | H_{EL} | \beta, n_i-1, 1, n_{ph}\rangle \boldsymbol{e}_s.\boldsymbol{p}_{\beta\alpha}(-\boldsymbol{k}_s)\boldsymbol{e}_i.\boldsymbol{p}_{\alpha 0}(\boldsymbol{k}_i)}{(\omega_\beta+\omega_{ph})(\omega_\alpha-\omega_i)} + \\
& \frac{\boldsymbol{e}_i.\boldsymbol{p}_{0\beta}(\boldsymbol{k}_i)\langle \beta, n_i-1, 1, n_{ph}+1 | H_{EL} | \alpha, n_i, 1, n_{ph}\rangle \boldsymbol{e}_s.\boldsymbol{p}_{\alpha 0}(-\boldsymbol{k}_s)}{(\omega_i+\omega_\beta)(\omega_\alpha+\omega_s)} + \\
& + \frac{\langle 0, n_i-1, 1, n_{ph}+1 | H_{EL} | \beta, n_i-1, 1, n_{ph}\rangle \boldsymbol{e}_i.\boldsymbol{p}_{\beta\alpha}(\boldsymbol{k}_i)\boldsymbol{e}_s.\boldsymbol{p}_{\alpha 0}(-\boldsymbol{k}_s)}{(\omega_\beta-\omega_{ph})(\omega_\alpha+\omega_s)} \\
& + \frac{\boldsymbol{e}_s.\boldsymbol{p}_{0\beta}(-\boldsymbol{k}_s)\boldsymbol{e}_i.\boldsymbol{p}_{\beta\alpha}(\boldsymbol{k}_i)\langle \alpha, n_i, 0, n_{ph}+1 | H_{EL} | 0, n_i, 0, n_{ph}\rangle}{(\omega_\beta-\omega_s)(\omega_\alpha+\omega_{ph})} \\
& + \frac{\boldsymbol{e}_i.\boldsymbol{p}_{0\beta}(\boldsymbol{k}_i)\boldsymbol{e}_s.\boldsymbol{p}_{\beta\alpha}(-\boldsymbol{k}_s)\langle \alpha, n_i, 0, n_{ph}+1 | H_{EL} | 0, n_i, 0, n_{ph}\rangle}{(\omega_\beta+\omega_i)(\omega_\alpha+\omega_{ph})} \Bigg|^2 \times \delta(\omega_i-\omega_s-\omega_{ph})
\end{aligned}
\tag{2.17}
$$

$$
\text{with} \quad \boldsymbol{p}_{\alpha 0} = \langle \alpha | ex(i\boldsymbol{k}_i.\boldsymbol{r}_j)\boldsymbol{p} | 0 \rangle
$$

Where, single electron-hole pair states in a semiconductor are represented by |α> and |β>. In the above equations, ‘n_i’, ‘n_s’, and ‘n_{ph}’ are the number of incident photons, scattered photons and optical phonons, respectively. The polarizations and wave-vectors of incident and scattered photons are denoted by ($\boldsymbol{e}_i$, $\boldsymbol{k}_i$) and $\boldsymbol{e}_s$, $\boldsymbol{k}_s$) respectively. The transition from |α> to |β> are electron-lattice interaction induced transitions and therefore, the differential scattering cross-section, in terms of susceptibility $\Delta\chi$, can be expressed as [91],

$$
\frac{d\sigma}{d\Omega} = \left(\frac{\eta_s \upsilon V}{\eta_i} . \frac{1}{16\pi^2 c^4} \right) \left(\frac{\hbar(n_{ph}+1)}{2M_r \omega_{ph} N} \right) \frac{\omega_s^5}{\omega_i} \left| (\boldsymbol{e}_s.\Delta\chi.\boldsymbol{e}_i) \right|^2 \tag{2.18}
$$

Where $V/N = a_0^3$ is the volume of the unit cell. From equation it can be inferred that scattering cross-section depends on the scattering volume and effectively on the fourth power of scattered frequency ‘ω_s^4’ (as $\omega_s \approx \omega_i$).

The quantum mechanical description developed above correctly explains the higher intensity of stokes line compared to anti-stokes component. Since at moderate and not too high temperatures, the population of ground vibrational state is expected to be much higher than the excited levels, the probability that incident photon finds the medium in excited vibrational level is much weaker than that for ground vibrational state. Phonons are integer spin particles and probability of occupation of given vibrational state obeys Bose-Enstein statistics. Therefore, from equation (2.19), the ratio of intensities of Stokes and anti-Stokes lines will be:

$$\frac{I_s}{I_{as}} \propto \frac{(\omega_i - \omega_{ph})^4}{(\omega_i + \omega_{ph})^4} \ \exp\left(\frac{\hbar\omega_{\mathrm{ph}}}{kT}\right) \tag{2.19}$$

Above equation, in contradiction to classical theory, correctly predicts that this ratio is considerably greater than unity as observed experimentally. The relative strength of Stokes and anti-Stokes lines can be understood by considering a simple example of Raman scattering from 'Si' wafer at room temperature. For 'Si' at 300 K, $\omega_{ph} \sim 520$ cm^{-1}, $kT \sim 200$ cm^{-1} and taking $\omega_s \approx \omega_i$, the ratio $I_s/I_{as} \sim 14$. This simple calculation demonstrates that stokes intensity is greater than that of anti-stokes line by more than an order at room temperature. This also exemplifies that the local temperature of the material under investigation can be determined by measuring the Raman scattered intensities of stokes and anti-stokes bands. This kind of analysis is extremely useful in segregating the effect (if any) of laser irradiation induced heating on the material properties, as we have employed for investigating the anomalous behavior of substrate layer in GaP/Ge(111) hetero-structures. Another aspect of quantum mechanical treatment of Raman scattering process, not apparent in macroscopic theory, is the Resonance phenomena. When the energy of incident laser radiation is tuned to coincide with the real electronic transition, the intensity of Raman scattered signal is strongly enhanced. This enhancement of scattering cross-section near the absorption bands is called resonance Raman scattering. Under resonance condition, only first one of the six terms in equation (2.17) or (2.18) has dominant contribution. The contribution of non-resonant terms which involves the summation over many intermediate states is weak and so can be regarded as constant term. Consequently, only one (top most) of the six Feynman diagrams shown in Fig. 2.2 has the strongest contribution. The unphysical divergence of the first term (energy denominator becomes zero) in equations (2.17) or (2.18) at condition when incident photon energy 'E_i' is equal to intermediate state (real electronic level) energy 'E_α', can be eliminated by considering the finite lifetime 'τ_α' of the state $|\alpha\rangle$ due to radiative and non-radiative decay processes. This is taken into account by assigning a damping constant $\Gamma_\alpha = h/\pi 2\tau_\alpha$ to energy state $|\alpha\rangle$ and replacing the energy 'ω_α' by '$\omega_\alpha - i\Gamma_\alpha/h$' in denominator of equation (2.17) or (2.18). The principal advantage of Resonance Raman measurements over non-resonant spectroscopy is that it can enhance the scattered signal intensity by several orders ($\sim 10^2$-10^6) of magnitude. Therefore, Resonant spectroscopy is extremely useful for the analysis of low concentration samples and nano-sized structures. In this thesis work, resonance Raman spectroscopy has been employed to study the nucleating layer (~60 nm thick) GaP/Si and GaP/Ge hetero-structures.

We have already explained that Raman scattering is an extremely weak process suffering from the Rayleigh background. Therefore, the experimental determination of high-quality Raman spectra involves advanced equipment, as discussed in the next section.

2.3 Raman spectroscopy Instrumentation

The principal components of a Raman spectroscopy instrument are:

(1) Laser light source for material excitation

(2) Collection optics to collect the scattered radiation

(3) Spectrometer for dispersing the spectral components of scattered light

(4) Detector for the detection of scattered radiation coming out of the spectrometer

In the following, we describe these components individually.

(1) Laser light source for material excitation: Raman scattering is inherently a weak process, wherein only one in 10^6-10^8 photons gets scattered inelastically. The intensity of Raman scattered radiation is directly proportional to the intensity of incident beam. Therefore a coherent, intense source of light would serve the purpose. Further, the light source should be highly monochromatic so that spectral width of Raman bands of interest would be as narrow as possible. Therefore, using a laser light source for excitation of the material can meet all these requirements. Also, the laser light (with TEM_{00} output) can be tightly focused to a very small spot size (<1 µm), which is advantageous for performing the Raman spectroscopy imaging and spatially resolved Raman measurements. Further, Raman spectroscopy of many materials particularly the semiconductors could become possible only after the development of lasers as most of the semiconductors are opaque. Continuous wave gas discharge lasers e.g., Argon ion laser, Helium-Cadmium (He-Cd) laser, Helium neon (He-Ne) laser having narrow line-width (<10 GHz) are preferred for Raman spectroscopy measurements. Furthermore, many discrete laser line excitations can be obtained from the single gas (e.g., Argon ion laser) laser source. In the red portion of visible spectrum, 633 nm excitation can be obtained from He-Ne laser. This flexibility enables the user to tune the wavelengths over a wide range as per requirement, which could be beneficial for resonance Raman measurements and selective probing of different layers in a multi-layered system *e.g.*, a semiconductor hetero-structure. Further, laser light is polarized (polarization ratio >200:1 for Argon ion laser) and this allows researchers to perform the polarization dependent Raman measurements. The direct band gap of GaP ($E_g(\Gamma)$ ~2.78 eV, 300K)) [86] is close to the excitation energy

of 442 nm (2.81 eV) laser line from He-Cd laser, and has been used in the Raman spectroscopy investigation of micro/nano-structured nucleating layer (~60 nm thick) hetero-structure, as described in this thesis.

(2) Collection optics: In micro Raman spectroscopy, depending on the sample and experimental requirements, the objective lenses of different numerical apertures are used for the collection of back-scattered light from the sample. The numerical aperture of a microscope objective lens determines its ability to collect light and resolve fine spatial details in the sample at a fixed object distance. Numerical aperture (NA) of a lens is defined by the relation:

$$NA = n.\sin\theta \qquad (2.20)$$

where 'n' is the refractive index of the medium between objective front lens and sample and 'θ' is the half angular aperture. Figure 2.3 shows the collection of radiation scattered from sample for the two objectives of different numerical apertures. It is evident from Fig. 2.3 that collection solid angle 'θ_2' is larger than that of the low numerical aperture objective 'θ_1'. The wider collection angle of high numerical aperture objective increases its light gathering ability and hence increases the sensitivity of measurement. From Rayleigh criteria, beam spot diameter d_{spot}= (1.22λ)/NA for the microscope objective, where 'λ' is the wavelength of incident laser beam, determines the diffraction limited lateral spatial resolution ($d_{spot}/2$). The higher NA objective gives rise to smaller focal spot size for a given wavelength, and therefore, it can be utilized for studying the sub-micron scale spatial non-uniformity in physical and chemical properties of the sample through the observed variations in corresponding Raman spectra. For the same laser power incident on the sample, a high NA objective enables larger power density (mW/cm^2) on focal plane, which also increases the sensitivity of Raman measurement.

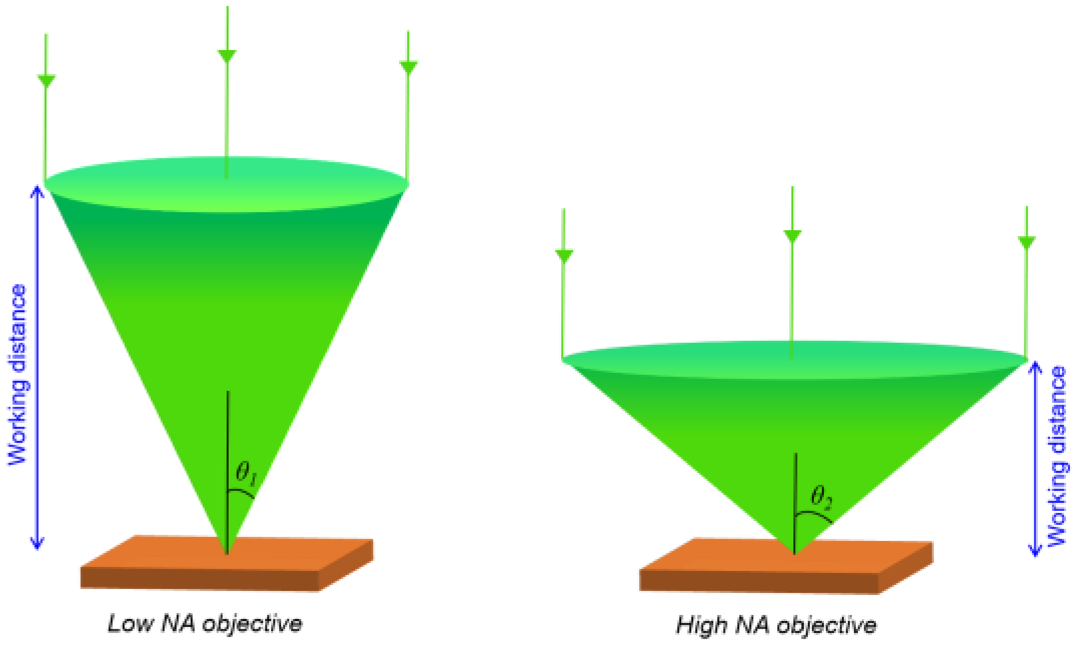

Fig. 2.3. *Schematic showing the light gathering ability, and working distances of microscope objectives, having different numerical apertures (NA).*

(c) Spectrometer: Raman spectrometer consists of a monochromator and a light intensity detector. The monochromator in turn comprises of entrance slit, a dispersive element *i.e.*, diffraction grating, collimating and focusing mirrors and the exit slit. A monochromator separates the collected light scattered from a medium into its spectral component wavelengths, and the intensity of outgoing (from spectrometer) light is measured over a broad spectral range. When photo multiplier tube (PMT) is used for photon detection, this configuration is called single channel detection. In case of single channel detection, a spectrometer equipped with PMT operates by moving the grating to different wavelengths (with one wavelength at a time) in scattered output and focusing them to a focal point on exit slit where PMT will sequentially record photon signal of each wavelength. On the other side, in multichannel configuration, generally termed as spectrograph, the exit slit is replaced by an array detector charge coupled device (CCD). This enables the simultaneous detection of wide spectral range in single acquisition. In contemporary Raman spectroscopy technique, multichannel

detection is the most commonly used configuration as it can serve the purpose for most of the applications. Spectrograph configuration has been used for recording all the Raman spectra presented in this thesis work. The monochromator forms an image of entrance slit in CCD plane at different wavelengths present in the scattered light, which can be achieved through Czerny-Turner configuration of monochramator shown in Fig. 2.4.

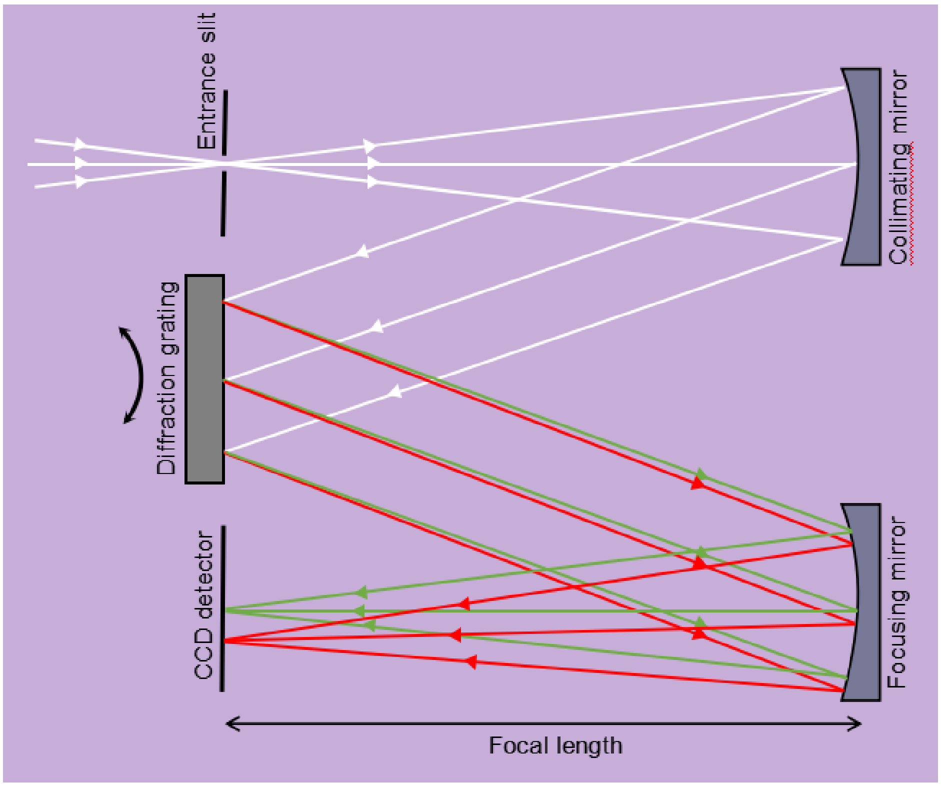

Fig. 2.4. *Schematic for Czerny-Turner design of a monochromator showing the beam paths and spectral separation in spectrograph*

The scattered beam from the sample is made to enter the spectrometer through entrance slit. Using a focusing lens, the scattered light is focused onto the entrance slit. A divergent beam of light from entrance slit is made to incident on the collimating mirror (Fig. 2.4), which collimates the light and directs it to the diffraction grating. The grating disperses (Fig. 2.4.) and hence spatially separates the spectral components of the scattered light. The diffracted beam from the grating is focused onto the CCD array by a focusing mirror (Fig. 2.4.). Spectral (wavelength) range and spectral resolution are two experimental parameters of utmost importance when dealing with spectrometers. For a given laser excitation wavelength, spectral range illuminating the CCD detector depends on the grating groove density and focal length of spectrometer. Spectral resolution of the spectrograph is a measure of its ability to resolve unambiguously, the closely lying spectral features into their separate components. Following factors determine the spectral resolution of spectrometer.

(a) Entrance slit width: Narrower the width of entrance slit, smaller will be the FWHM of instrumental profile of the spectrometer and hence better the spectral resolution of the system.

(b) Dispersion: Dispersion is a function of (i) focal length of monochromator (Fig. 2.4) (ii) groove density of the diffraction grating and (iii) excitation laser wavelength. Longer focal length and high groove density further increases the spatial separation between the spectral components falling on detector, and this leads to higher (less in magnitude i.e., improved) spectral resolution of the system. For the same focal length and groove density, the larger excitation wavelength leads to larger diffraction angle for the spectral components in scattered beam and thus improves the spectral resolution.

(c) Exit slit width: Narrower exit slit width improves the spectral resolution of the system. In case of CCD used for detection of scattered light, each pixel (photo-detector element) serves as an exit slit, where pixel width is equivalent to exit slit width. Therefore, a CCD with smaller size pixels improves the spectral resolution of the system. Practically, the spectral resolution is determined by measuring the FWHM of sharp atomic transition lines (plasma lines) of the gas lasers, or width of

Rayleigh line as it has linewidth ~20 MHz [87]. Depending upon the particular application involved and the information desired from material under investigation, low or high spectral resolution may be required.

Besides spectral resolution, another issue of considerable importance in single monochromator Raman spectrometer is the rejection of stray light. The intensity of Raman scattered light is 6-8 order of magnitudes weaker than that of elastically scattered Rayleigh light. Also, in most experiments, the frequency of Raman scattered signal is very close to excitation laser frequency. Therefore, in order to detect the weak Raman signal in the proximity of strong laser light, a notch or edge filter (Optical density OD>6) which block out the laser light, is used. Apart from ultra-high spectral resolution, excellent stray light rejection can also be achieved by employing the multistage monochromator configuration. The triple Raman spectrometer can be utilized in additive and subtractive modes. In triple additive configuration, three monochramators, three monochromators are used and each stage disperses the incoming scattered light leading to ultra high resolution which enables the researcher to very accurately determine the frequency position of Raman spectral lines depending on application involved. The multistage system can be easily switched to triple subtractive mode wherein the first two monochromators act as integral pair. The first one of two monochromators disperse the polychromatic light and physically block (reduces its intensity through intermediate slit between stage 1 and stage 2) the intense Rayleigh light and then second monochromator recombines all the dispersed light and focuses this polychromatic light on the entrance slit of third stage. The third stage monochromator provides all the dispersion for separating the spectral components. The advantage of triple subtractive mode is that it can used as a tunable notch filter because this configuration can be employed for any laser excitation wavelength unlike the notch or edge filter which are specific to laser wavelengths, and their availability for each wavelength is another concern. Further, excellent stray light rejection in triple subtractive mode allows the user to extract the spectral information very close (10-20 cm^{-1} away from Rayleigh line) to laser line. Although multistage spectrometer system achieves the high stray light rejection, ultra high resolution and measurements very close to laser wavelength, one has to compromise with loss of throughput as compared to single stage spectrometer. Therefore, three factors *e.g.*, resolution, stray light rejection and throughput decide whether one has to use single, double or triple stage configuration. For the Raman measurements presented in this study, we have used Raman spectrograph in single-stage and multi-stage (triple subtractive mode) configurations.

(d) Detection: Detection of inherently weak inelastically scattered light is another important aspect of Raman spectroscopy set-up. Owing to high speed data acquisition, nowadays multichannel detection system based on charge couple device (CCD) are the most commonly used detectors for wide-range spectroscopy applications. The CCD is based on silicon semiconductor which consists of several thousand pixels, arranged in two dimensional arrays. Each pixel on interaction with light generates electrical charges proportional to the incident photon flux and acquisition time, which is measured using the suitable electronics. Depending on the way the light photons reach the photosensitive (pixels) region of the CCD, Si based CCDs are categorized as front and back illuminated sensors. In front illuminated CCD, the photons strike on the same side of sensor where gate electrode is present. This gate structure can absorb and/or reflect some of the photons thereby reducing limiting the QE (~50%) of CCD. However, in a back illuminated CCD, the illumination is done from the back of the sensor i.e., Si from substrate side. To make this effective, most of the Si substrate is

removed via etching and reduced to thickness ~10 µm. The quantum efficiency close to ~80% (in visible range) can be achieved. The key parameters associated with detector performance are signal-to-noise ratio (sensitivity) and quantum efficiency, and consequently these parameters decide the quality of Raman spectra. The major challenge in a CCD is to increase the signal-to-noise (S/N) ratio by reducing the noise. The primary sources contributing to noise in CCD are (i) Signal shot noise (ii) Thermal noise (Dark noise) and (iii) Sensor read out noise. In most experiments, for a Peltier cooled (-70°C) CCD, the photon noise is almost always the governing noise source once the signal increases above some background signal. For fixed photon flux incident on sensor and quantum efficiency of detector, the S/N ratio in Raman spectra can be increased by increasing the integration (exposure) time and number of accumulations at that exposure duration.

In chapter 1, we have discussed how Raman spectroscopy, when facilitated with atomic force microscopy (AFM), could advance the understanding of crystallographic morphed surfaces, as implemented in the present thesis work. In the view of this, the working principle, concept and technical aspects of AFM are discussed in the next section.

2.4 Atomic Force microscopy: Working principle and technique

Atomic force microscopy (AFM) is a type of scanning probe microscopy technique which images the 3-dimensional topography of the sample surface at nanoscale, and has played a key role in enriching our understanding on nanoscience and technology [92, 93]. In AFM, surface of the sample is probed with a sharp tip (generally pyramidal shaped and made of silicon or silicon-nitride), a couple of microns long and often ~10 nm in radius. When the tip is brought in proximity of the sample surface to be investigated, the forces between the atoms of the tip and that of the sample (at the surface) give rise to the deflection of cantilever. The inter-atomic forces between sample and tip atoms, called Van der Waals forces, are accurately modeled by Lennard-Jones potential (U):

$$U = U_0\left[-2\left(\frac{r_0}{r}\right)^6 + \left(\frac{r_0}{r}\right)^{12}\right] \tag{2.21}$$

Here 'r' is the distance between the atoms, and 'r_0' is the equilibrium distance between the atoms for which the potential energy is minimum 'U_0'. The first term in the above equation describes the long distance attraction caused by the dipole-dipole interaction and the second term takes into account the short range repulsion forces due to Pauli Exclusion Principle. The variation of forces with the distance between the two atoms based on the Lennard-Jones potential is shown in Fig. 2.5. Depending on the tip to sample separation, two modes of AFM operation can be realized:

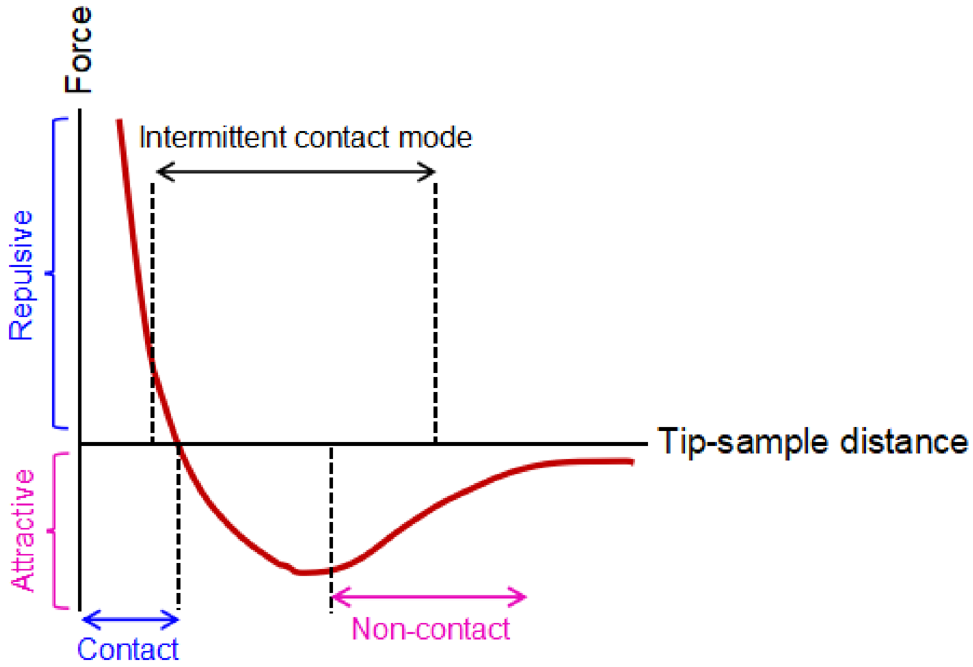

Fig. 2.5. *Force-distance curve showing the contact and non-contact operation regions of the atomic force microscopy*

AFM contact mode: In the contact mode (Fig. 2.5), the typical vertical separation between tip and sample is order of few (~5-10Å) Angstroms, and the AFM probe makes a soft physical contact with sample surface. During the initial contact, the atoms at the end of the tip experience a weak repulsive force due to overlap of electronic orbitals of the atoms of tip and sample.

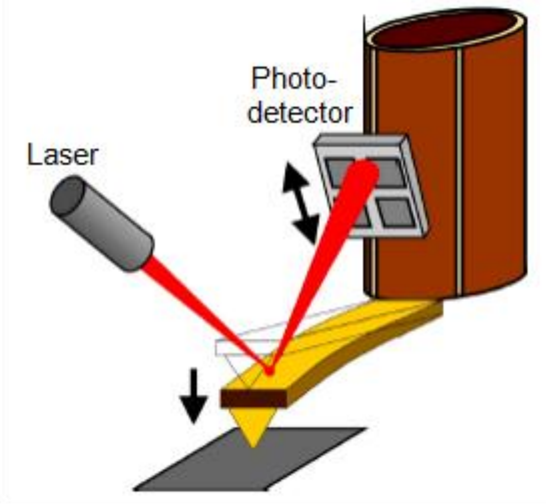

Fig. 2.6. *Schematic diagram showing the general beam bounce detection scheme for AFM measurement. Reproduced from user manual of SPM integrated (Alpha 300S) Raman system*

In this mode, not only vertical force but lateral forces also act between the tip and sample, which may lead to dragging of weakly bound structures and produce the blurred images. These complications require that the spring constant (<1 N/m) of the cantilever should be low *i.e.*, smaller than the spring constant holding the atoms of the sample together. The total force between the tip and the sample in the contact regime generally varies from ~ 10^{-8} N to ~ 10^{-7} N. Contact mode is mainly preferred for imaging the hard surfaces. The schematic for beam bounce detection scheme that most AFMs use for measuring the cantilever deflection is shown in Fig. 2.6. The vertical movement of laser spot (from central position) on photo-detector (Fig. 2.6) is directly proportional to the bending of cantilever and determines the magnitude of deflection. Once the deflection in cantilever is detected, the topographical information can be obtained by operating in the constant force mode. In constant-force mode, the deflection of the cantilever is used as input to a feedback circuit which, in response to surface topography, moves the sample scan stage up and down in vertical direction, thereby maintaining the cantilever deflection constant. In this case, the topographical image is generated from the up and down motion of scan stage.

AFM Non-contact mode: Non-contact mode mode operates in the attractive forces regime (Fig. 2.5), and in this mode tip is brought into close proximity (within few nanometers) to the sample surface, but not in contact with the sample. In this mode, the cantilever is made to vibrate near its resonance frequency (100-400 kHz) with amplitude of few nanometers. Because of the force between the atoms of the tip and the sample, the cantilever gets deflected which in turn results in either the change in resonant frequency or the vibrational amplitude of the cantilever. In the AFM set-up used for the present study, the system monitors the changes in vibrational amplitude of the cantilever and keeps it constant using a feedback system that moves the sample scan stage up and down. Similar to contact mode (in constant-force mode), the motion of the scan stage is used to generate the topographical information in non-contact mode AFM. Because of the small forces ($\sim 10^{-12}$ N) between tip and sample in non-contact mode, it is advantageous for studying soft samples. In addition, cantilevers used for non-contact AFM must be stiffer (spring constant ~40 N/m) than those for contact AFM, because soft cantilevers can be pulled into contact with the sample surface. As compared to contact mode, the non-contact mode has the advantage that tip or sample degradation effects are minimized because the tip-sample interaction force is predominantly vertical and the lateral forces are negligible.

The experimental parameters which determine the lateral resolution of AFM are radius of curvature of probe tip and step size of image. Scan speed is another important parameter in AFM mapping which is limited by the speed of feedback circuit and therefore the faster scanning can give rise to noise in the topographical features.

2.5 Transmission electron microscopy: Principal and technique

The operating principle of Transmission electron microscopy (TEM) is same as that of light microscope; however in TEM an electron beam is used instead of light [94]. The electron beam behaves like a wave having de-Broglie wavelength five orders of magnitude smaller than light waves. When a high energy (100-300 keV) electron beam is passed through a thin specimen, electrons are either scattered or get transmitted through the sample. Depending on the arrangement of electromagnetic lenses and objective aperture, scattered/transmitted electrons beam is focused to form an image or diffraction pattern. In the imaging mode of TEM, the beam of electrons transmitted through the sample contributes to the image formation. The contrasting features in a TEM image stem from the non-uniformity in atomic density and specimen thickness. Furthermore, high resolution TEM (HRTEM) is a type of TEM which makes use of transmitted and scattered electron beam to produce an interference image. The basic principle of HRTEM is same as that of TEM, however the high magnifications studies in HRTEM allows imaging of the materials on the atomic scale. HRTEM is an ultimate tool in imaging, and has been successfully used for analyzing crystallographic structure and crystal defects (e.g., dislocations, stacking faults etc.) in various kinds of materials on atomic scale. Since sufficient number of electrons has to pass through the specimen to form an image, the TEM specimen should be thin (~100 nm) enough. Therefore apart from instrumentation, the sample preparation, particularly for the cross-sectional measurements, is another challenging aspect of TEM analysis. Initially, two small (each of width ~3 mm) hetero-structure samples are joined together from the epilayer side, and then inserted into a hollow cylindrical (diameter ~3 mm) brass-rod with cross-sectional region towards open side of brass rod. The cylindrical ring (thickness ~1 mm) cut from this brass rod is mechanically thinned to ~70-100 µm, and then loaded into dimple grinder to further reduce the thickness to ~20 µm. Finally, the sample is loaded in precise ion-milling machine (Argon ion gun) to get a few tens of nanometer thick specimen.

In the following section, we illustrate the different experimental set-ups used for Raman spectroscopy, atomic force microscopy and TEM study of GaP/Si and GaP/Ge hetero-structures.

2.6 Experimental set-ups: Raman spectroscopy, AFM and TEM

Depending on the kind of analysis required, Raman spectroscopy measurements on the different GaP/group-IV hetero-structures are performed using Acton *SP-2500i* single spectrograph and TriVista *TR557* triple (Spectroscopy & Imaging GmbH, Germany) Raman spectrograph. Acton *SP-2500i* is the part of scanning probe microscopy (SPM) integrated Raman system *Alpha 300S* (WiTec, Germany), which has been used for AFM measurements also. Structural properties of one of the hetero-structure samples are further confirmed by high resolution transmission electron microscopy (Philips CM200). In the following, we present the brief description of each of these experimental set-ups.

2.6.1 SPM integrated Raman spectroscopy system

Figure 2.7 shows the schematic of SPM integrated Raman spectroscopy set-up *Alpha 300S* along with elaborated images of Raman spectrograph and AFM beam path. For Raman spectroscopy measurements, the excitation laser (shown in green) delivered through a single-mode optical fiber is directed towards the sample using a holographic beam splitter (BS, Fig. 2.7) and then focused onto the sample by an infinity corrected microscope objective. The light scattered by the sample is collected by the same objective, made to pass through the beam splitter and Rayleigh-blocking edge filter (discussed in section 2.3), and then focused onto a multi-mode fiber. Holographic BS, designed for specific wavelength, diffracts laser light towards the sample with an efficiency of >90% and transmits the light of other wavelengths (*e.g.*, the scattered light from sample) with high efficiency. The multi-mode fiber (diameters: 25μm, 50μm and 100μm) couples the scattered beam to 500 mm focal-length Czerny-Turner monochromator (described in section 2.3) equipped with a CCD camera. The spectrograph (Fig. 2.7) includes a grating turret having three gratings of different groove densities viz., 600 g/mm, 1200 g/mm and 2400 g/mm. A thermoelectrically cooled back-illuminated CCD (Andor DV-401-BV) having quantum efficiency ~80% in the desired wavelength range 400-550 nm, is used for signal detection. The CDD has an array of 1024×128 sensors, each of size 26×26 μm. For polarization dependent Raman spectroscopy, a polarizer is positioned above the edge filter (Fig. 2.7) in the scattered light path. Raman measurements presented in this thesis have been performed using 25μm, 50μm multi-mode fibers, mostly 2400 g/mm grating and low (NA=0.55, NA=0.75, 50X) and high numerical aperture (NA=0.90, 100X) objectives. However, for Raman spectral imaging, we have used 1200 g/mm grating. For most of the Raman measurements, focal spot size and spectral resolution (discussed in section 2.3) are <1 μm and <2.0 cm^{-1} (wavenumber per pixel <0.7 cm^{-1}) at the wavelengths (442 nm, 488 nm and 514.5 nm) of interest. In the following, we describe the methodology and technical aspects of Raman imaging, AFM scanning, and Raman and AFM mapping at the same site.

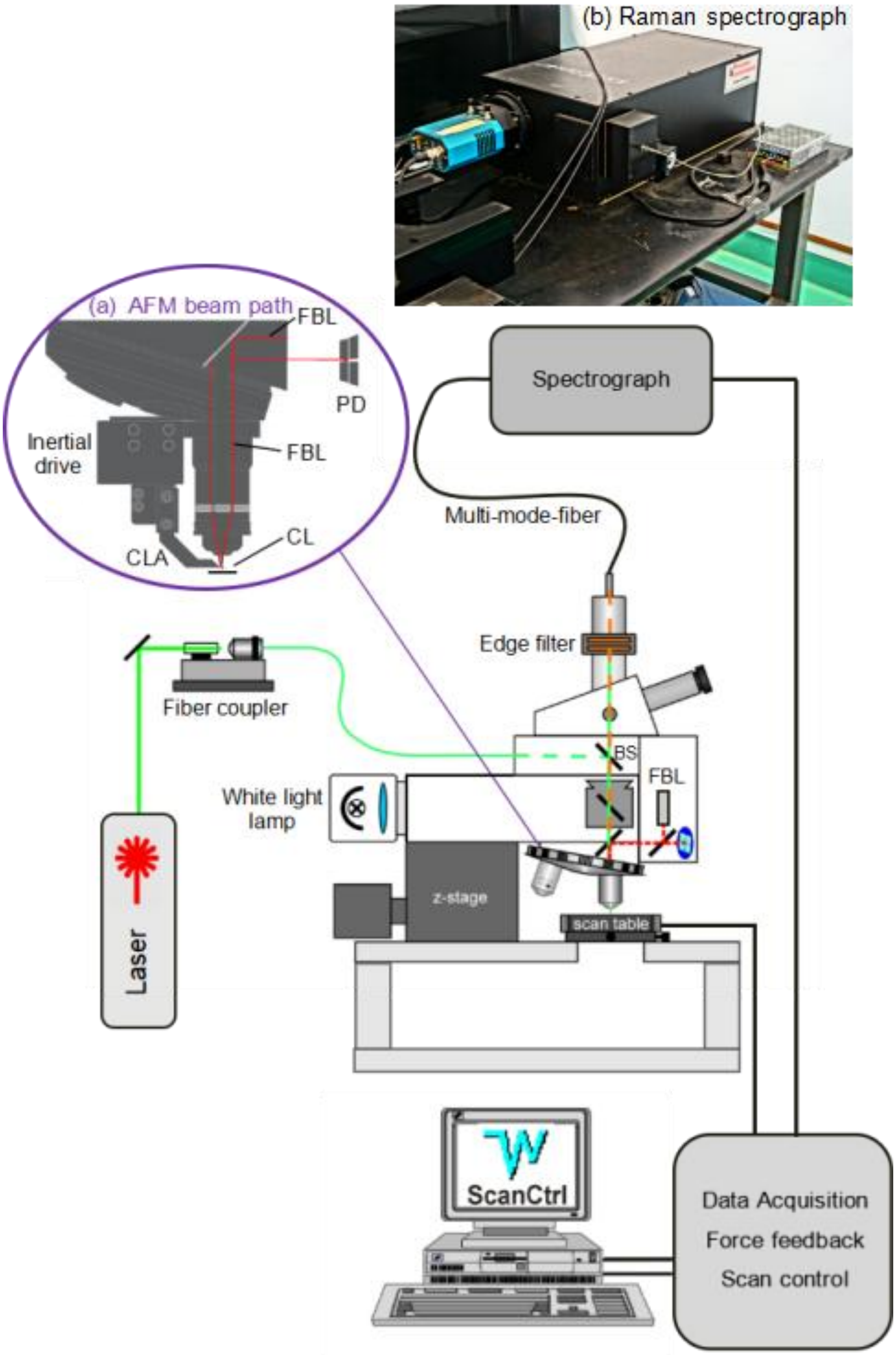

Fig. 2.7. *Optical schematic of SPM integrated Raman set up with its major components. Inset (a) scheme of AFM measurements in same instrument (b) elaborated image of single stage spectrograph with CCD(in blue color) and fiber coupling at the entrance. FBL: feedback laser, PD: photodiode, CLA: Cantilever arm, CL: Magnetically held cantilever, BS: beam splitter. Reproduced from user manual of SPM integrated (Alpha 300S) Raman system.*

(a) Raman imaging and spatially resolved Raman spectroscopy: For Raman imaging, first the desired sample region to be scanned is chosen using the optical image (of the sample) as guide. Then piezo-electrically driven sample-stage (scan range=100μm in X and Y directions) is scanned in X-Y directions under the microscope objective to record the Raman spectra corresponding to different spatial positions. Raman spectral map is generated by integrating the Raman scattered intensity over the desired phonon frequencies. Similarly, the spatially resolved Raman spectra from different locations on the sample, is obtained by selecting the desired site in optical image so that scan table (under the optical probe) moves to corresponding spatial position.

(b) AFM mapping: For AFM mapping, *Alpha 300S* uses a large working distance (WD) objective (e.g., 50X, WD=8.5 mm) and an inertial drive assembly which magnetically holds the cantilever arm (Fig. 2.7) and cantilever itself under the objective. This arrangement facilitates simultaneous observation of sample and the cantilever in optical image. Using a beam splitter and dichroic mirror, the feedback laser (FBL, 980 nm) is first directed onto the cantilever (Fig. 2.7) and then back onto the segmented photodiode (described in section 2.4). The feedback laser is focused onto the cantilever and collected back using the large working distance objective. In SPM integrated Raman system, the same scan stage is used for Raman and AFM mapping. The sample scan stage has the travel range of 20μm in Z (vertical) direction. The closed loop resolutions of scan stage in X-Y and Z directions are ≤1 nm and ≤0.1 nm respectively. In order to avoid the tip or sample degradation effects, most of the AFM maps presented in this thesis have been obtained using non-contact mode of operation. Based on the sizes of GaP micro/nano-structures studied in this work, a step size at least 8-10 times smaller than the size of individual GaP structure is chosen to obtain the high resolution topographical image. As we emphasized the significance of measuring speed in section 2.4, the moderate scanning speed (~2 sec/line) is used to obtain good quality topographical images.

(c) Raman and AFM mapping in the same regions of the sample: In chapter 1, we discussed the effectiveness of Raman spectroscopy and AFM measurements performed at the same spatial sites, for extracting out nearly the one-to-one correlation between surface topology and vibrational signatures of the material. Due to experimental complexities, and to achieve greater degree of certainty in correlation between two techniques, the region of samples having rarefied micro/nano-structures is selected for such studies. Using SPM integrated Raman system (Fig. 2.7), Raman spectroscopy and AFM measurements are carried out independently *(i.e.*, one by one) on a chosen area of the sample. Visual optical image of the selected area (of the sample) is taken as the guide for ensuring that both Raman and AFM are being performed in the same selected region of the sample. Coinciding the position of focused laser spot in Raman mapping with the site where AFM tip lands on the sample surface, is a crucial step of this experiment. Through repeated, one-to-one Raman and AFM mapping experimentation on a carefully chosen reference sample, we find the spatial difference between laser focal spot and AFM tip landing position. This positional difference between two kinds of probes is taken into account while performing Raman and AFM mapping in same region. Using the optical image, we select an area of the sample and first perform the AFM scanning in that region. Then we perform Raman imaging in the same region, and again the AFM mapping is performed to ensure the reproducibility of the measurements. This methodology has been adopted by us for the analysis the micro-structured GaP layer grown on Ge substrate.

2.6.2 Triple Raman spectrograph set-up

Figure 2.8 shows the photograph of TriVista *TR557* triple Raman spectrograph, wherein first the excitation laser is coupled to microscope body and then the back-scattered light is directed to entrance slit of monochromator, using free-space optics. The system can be used in single and triple additive/subtractive (described in section 2.3) configurations.

Fig. 2.8. *Photograph of triple Raman spectrograph TR557, showing three monochromators (TMC) and microscope assembly (MA). OPA: optical assembly (mirrors, neutral density filters, beam splitter, edge filter), SS: sample scan satge, CM: coupling mirror (pre-monochromator), FM: flip mirror.*

Each of the monochormator in *TR557* has Czerny-Turner configuration and includes gratings of different groove densities 600/900 g/mm, 1800 g/mm and 2400 g/mm. The focal lengths of first, second and third monochromators are 500 mm, 500 mm and 750 mm respectively. Raman scattered signal is detected using thermoelectrically cooled, back-illuminated CCD (PIXIS:256E, Princeton Instruments, USA), installed on third monochromator (Fig. 2.8). The CDD has an array of

1024×256 pixels, with each of size 26×26 μm. The third monochromator is used as single stage spectrograph also. For using *TR557* Raman set-up in triple spectrograph configuration, the scattered light collected by microscope objective is directed to entrance slit of first monochromator via a flip mirror (Fig. 2.8). Software operated switching between triple- additive and triple-subtractive mode is attained by changing the direction of grating's rotation. In triple subtractive configuration, the gratings of first and second monochromator are made to rotate (synchronously) in clockwise and anti-clockwise directions respectively. Consequently, the dispersion generated by grating of first monochromator is canceled by that of second monochromator. However in triple additive mode, gratings of both first and second monochromator synchronously rotate in clockwise direction, thereby adding the dispersion produced by each. Stoke-antiStoke and azimuthal angle-dependent polarized Raman measurements presented in this thesis have been performed using Trivista *TR557* Raman set-up in triple subtractive (900 g/mm, 900 g/mm and 1800 g/mm gratings) and single spectrograph (1800 g/mm grating) mode. The wavenumber per CCD pixel at 514.5 nm laser wavelength and 200 μm entrance slit width, used for Raman measurements is <0.6 cm^{-1}. We have used infinity corrected low working distance 50X (NA=0.75) and 100X (NA=0.90) objectives for focusing (focal spot size <1 μm) the laser beam on sample.

2.6.3 Transmission electron microscopy set-up

The cross-sectional HRTEM measurements presented in this thesis are performed using the Philips, CM 200 instrument. The CM 200 system has a LaB$_6$ source and it is operated at an accelerating voltage 200 kV, giving the resolution ~2.4 Å. Cross-sectional HRTEM measurements on one of the hetero-structure sample are carried out by *Dr. Himanshu Shrivastava* (LML, SUS, RRCAT). The sample suitable for cross-sectional HRTEM analysis is prepared using dimpler (Gatan dimple grinder 656) and ion milling (Gatan precise ion polishing system 691) machine. The preparation of sample is carried out under the guidance of *Shri Mahendra Babu* (IOD, RRCAT) and *Dr. Himanshu Shrivastava* (SUS, RRCAT). Sample preparation is also assisted by Shri Chandrashekhar (RSL, RRCAT).

Chapter 3: Interfacial polytypism and Inter-diffusion in GaP/Ge(111) hetero-structures

3.1 Introduction and background

In the first chapter, we discussed the challenges associated with the hetero-polar integration of GaP on group-IV substrates and described how the lattice mismatch and substrate orientation, apart from hetero-valency, could influence the surface and crystalline properties of epilayer. In addition to the hetero-polar interface in GaP/Ge(111), there exists a large (~4%) lattice-mismatch. Till date very few reports exist on the growth and studies of large lattice-mismatched GaP-on-Ge material combination [26, 95]. Although carrier transport behavior and electronic band alignment properties of MOVPE grown GaP/Ge hetero-junction have been reported, the structural aspects and atomic inter-diffusion near the hetero-junction have largely remained unexplored [26, 95]. In view of this, we have explored the epitaxial integration of GaP on Ge(111) in greater depth by using the novel combination of Raman and atomic force microscopy (AFM). Our results provide direct experimental evidence for the intricate correlation between hetero-polar epitaxy, lattice mismatch, growth kinetics, and structural attributes of GaP epilayer grown on Ge(111) substrate. As discussed in chapter 1 and 2, Raman spectroscopy coupled with AFM offers a unique tool to corroborate vibrational and topological features. In the present chapter, this potentiality along with spatially resolved polarized Raman spectroscopy from cross-sectional surface (CSS) has been employed to determine the sub-micron scale structural variations and their correlation with topographical changes. Further, the wavelength dependent Raman spectroscopy is utilized innovatively to inspect the surface passivation- and kinetic-dependent physico-chemical changes occurring in underlying substrate layer near the GaP-Ge hetero-interface.

Consequently, this chapter is organized into two sections. In the first section, effect of large lattice-mismatch and polar/non-polar interface on physical and structural properties of micro/nano-structured GaP epilayer grown on Ge(111) substrate is explored. The co-existence of GaP allotropes, *i.e.*, wurtzite (WZ) phase near hetero-junction interface and dominant zinc-blende (ZB) phase near GaP surface is established using the spatially resolved polarized Raman spectroscopy from the cross-sectional surface (CSS) of hetero-structure. The inter-diffusion of constituent elements across the GaP-Ge hetero-interface, and its influence on the substrate layer are ascertained using wavelength dependent Raman measurements, in second section. In last section, the results of study on GaP/Ge(111) hetero-structures, and their key significances are summarized.

3.2 Interfacial Polytypism in GaP/Ge(111) hetero-structures

Raman spectra in back scattering geometry, arising from (111) surface of nucleating and thick layer GaP/Ge(111) hetero-structures (schematic: Fig. 3.2.1(a)), are shown in Fig. 3.2.1(b). Raman spectroscopy and Raman mapping measurements are performed using SPM integrated Raman system (*Alpha 300S*, section 2.6). Raman spectroscopy is performed at room temperature in back-scattering geometry. The excitation wavelengths used are 488 nm (Ar ion laser) and 442 nm (He-Cd laser). The spectral resolution of the Raman spectrograph at the wavelengths of measurement is ~1.5–2.0 cm^{-1}. A 100x microscope collection objective is used and the spatial resolution of the measurement at 442 nm and 488 nm are ~0.5 µm and ~0.6 µm, respectively. Also, AFM and the same site Raman-AFM measurements are performed using the same SPM-Raman (*Alpha 300S*) integrated system.

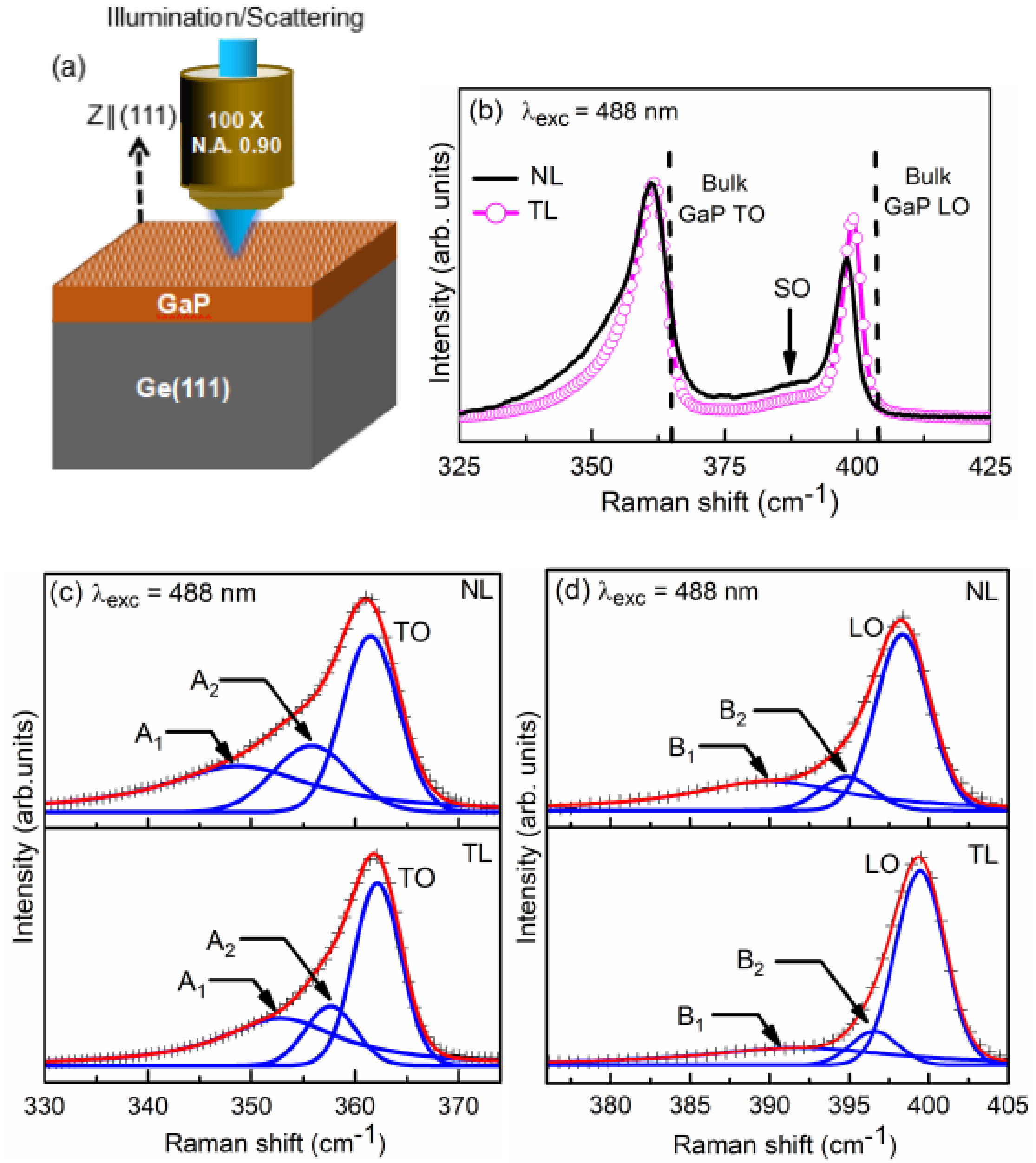

Fig. 3.2.1. *Schematic of Raman back-scattering from growth surface of GaP/Ge(111) hetero-structures. (b) Raman spectra of nucleating and thick layers in back-scattering from (111) surface. (c) TO phonon deconvolution and (d) LO phonon deconvolution for nucleating and thick layers using minimum required Lorentzian and Gaussian lineshapes. Red color fit to data (+) shows total fit.*

Representative Raman spectra in Fig. 3.2.1(b) show mainly the two dominant features ~362 cm^{-1} and ~399 cm^{-1}, corresponding to transverse optical (TO) and longitudinal optical (LO) phonons of GaP, respectively. The additional mode observed ~389 cm^{-1} in between TO and LO phonon is attributed to surface optical phonon [96]. The surface optical phonon is more significant in nucleating layer as shown in Fig. 3.2.1(b). Additionally, an asymmetric broadening is also observed on lower frequency side of GaP TO phonon [97, 98]. It has been reported that anharmonic interaction of TO phonon with two phonon density of states gives rise to asymmetry on lower frequency side of TO phonon, which has been observed even for bulk GaP [97, 98]. An additional asymmetry component is observed on lower frequency side of TO phonon of nucleating and thick GaP layers, which we understand through deconvolution. Asymmetric feature on lower frequency side of GaP TO phonon, for nucleating and thick layers, is deconvoluted (Fig. 3.2.1(c)) into one Lorentzian A_1 ~349 ± 0.4 cm^{-1}, and two Gaussians A_2 ~358 ± 0.1 cm^{-1} and A_3 (TO) ~361.5 ± 0.02 cm^{-1}. Similarly, Raman spectra of nucleating and thick layers in the LO phonon spectral range 376–405 cm^{-1} (Fig. 3.2.1(d)) are also deconvoluted into one Lorentzian B_1 ~389.5 ± 0.5 cm^{-1}, and two Gaussians B_2 ~396.4 ± 0.1 cm^{-1} and B_3 (LO) ~398.5 ± 0.1 cm^{-1}. Generally, one would expect that all phonon modes be fitted using Lorentzian line shape, and this was performed initially. However, it did not give proper fit and line shape suggested that the high frequency modes, *i.e.*, TO and LO phonons have Guassian profile. Indeed, best fit has been obtained using Guassian profiles for $A_{2(\text{TO asymmetry})}$, TO, $B_{2(\text{LO asymmetry})}$ and LO modes. The reason for the Gaussian line-shape of these modes will become evident in subsequent sections. The phonon mode A_1 on lower frequency side of TO has the same origin as bulk GaP [97, 98]. The full width half maxima (FWHM) of the LO phonon for both layers is ~4.0 cm^{-1} and is indicative of reasonably good crystalline quality of the GaP layer. It is observed that both TO and LO phonons arising from GaP/Ge hetero-structures are red shifted with respect to that of bulk GaP(111) by ~2.5 cm^{-1} and ~3.5 cm^{-1}, respectively. The origin of red-shift of TO and LO phonons and presence of additional modes on lower frequency side of TO and LO phonons are analyzed in the next sub-section.

3.2.1 Determination of biaxial strain

GaP layer grown on Ge(111) substrate is expected to undergo biaxial tensile strain due to lattice mismatch between substrate and epilayer. However, thickness of the grown GaP layer is greater than its critical thickness and therefore it is expected to be relaxed via the generation of dislocations. From the area scan of high resolution X-ray diffraction (HRXRD) experiments, it has been observed that in spite of expected relaxation, GaP layers contain residual tensile strain with anisotropic distribution for in plane and out of plane directions [26]. Thus the observed shift in the frequency of TO, LO and the additional phonon modes are attributed to presence of residual strain. Considering the biaxial strain in (111) plane as the cause of the observed shift in TO and LO phonons, the frequencies of triply degenerate $|\boldsymbol{q}| \approx 0$ optical phonons of strained (deformed) crystal are given by the solution of secular equation [99]

$$\det\begin{bmatrix} (p+2q)\varepsilon_{xx}-\lambda & 2r\varepsilon_{xy} & 2r\varepsilon_{xy} \\ 2r\varepsilon_{xy} & (p+2q)\varepsilon_{xx}-\lambda & 2r\varepsilon_{xy} \\ 2r\varepsilon_{xy} & 2r\varepsilon_{xy} & (p+2q)\varepsilon_{xx}-\lambda \end{bmatrix} = 0 \qquad (3.2.1)$$

Where, the eigenvalues $\lambda = \omega^2 - \omega_0^2$ with ω and ω_0 representing the strained and unstrained frequencies of the phonon modes. Also, ε_{xx} and ε_{xy} are the hydrostatic and shear components of the strain, respectively. Secular equation (3.2.1) has been obtained under quasi-harmonic approximation by retaining the terms linear in strain. The aforementioned results can be generalized to ZB crystals (e.g. GaP) by taking into account the LO–TO splitting due to long range coulomb interaction (ionicity of the bond). The strain effects on LO–TO splitting can be explained by considering the two different sets of phonon deformation potentials *p, q* and *r* for TO and LO phonons. The GaP film considered here has (111) orientation and the secular equation (3.2.1) and the strain tensor are defined in crystallographic basis, *i.e.*, $x\equiv$ (100), $y\equiv$ (010) and $z\equiv$ (001). The three eigen values obtained from equation (3.2.1) are:

$$\lambda_1 = \lambda_2 = \omega_d^2 - \omega_0^2 = (p+2q)\varepsilon_{xx} - 2r\varepsilon_{xy} \qquad (3.2.2a)$$

$$\lambda_3 = \omega_s^2 - \omega_0^2 = (p+2q)\varepsilon_{xx} + 4r\varepsilon_{xy} \qquad (3.2.2b)$$

where, ω_d (doubly degenerate) and ω_S (singlet) are eigen frequencies of TO and LO phonons with polarizations in and out of (111) plane respectively. The relevant parameters [100] of bulk GaP, used for estimation of strain are listed in Table 3.1.

Table 3.1. *Material parameters of bulk GaP at 300K used for the calculation of biaxial strain.*

Phonon	Raman shift (cm^{-1})	$\frac{-(p+2q)}{6\omega_0^2}$	$\frac{r}{\omega_0^2}$
TO	364.7 cm^{-1}	0.90	-0.58
LO	403.2 cm^{-1}	0.87	-0.50

Using these parameters and observed values of TO and LO phonon frequencies, the in plane strain parameters $\varepsilon_{parallel}$ for GaP nucleating and thick layers are calculated from equations (3.2.2a) and (3.2.2b). The results are summarized in Table 3.2. These values are different than those reported from HRXRD analysis (~0.0030 for thick layer) of these hetero-structures [26]. The apparent differences in results (for $\varepsilon_{parallel}$ for thick epilayer) from HRXRD and Raman spectroscopy may be attributed to following differences between the two methodologies: (1) The strain parameter determined from XRD measurements is the average one, obtained from ~30 mm^2 spatial area [101] whereas, in Raman spectroscopy, we have probed the region of the sample having area <1 µm^2, (2) Further, Raman spectral mapping over different regions of the sample, shows variation of ~1-1.5 cm^{-1} in the frequency of TO and LO phonons. It is important to note here that this variation is equivalent to the observed deviation in the value of $\varepsilon_{parallel}$ determined from XRD.

.

Table 3.2. *Calculated values of $\varepsilon_{parallel}$, $\omega_{TO(s)}$ and $\omega_{LO(d)}$ from the experimentally observed values of $\omega_{TO(d)}$ and $\omega_{LO(s)}$ for GaP/Ge(111) hetero-structures.*

Sample	$\omega_{TO(d)}$ (cm^{-1})	$\omega_{LO(s)}$ (cm^{-1})	$\varepsilon_{parallel}$	$\omega_{TO(s)}$ (cm^{-1})	$\omega_{LO(d)}$ (cm^{-1})
GaP/Ge(111) Nucleating layer	361.5	398.5	0.0018	360.4	399.5
GaP/Ge(111) Thick layer	362.2	399.6	0.0014	361.3	400.4

For BSG from (111) surface, the eigen values λ_1 and λ_2 in equation (3.2.2a) represent the shift of doublet type phonon (*i.e.*, TO) and the eigenvectors corresponding to these eigen values are polarized perpendicular to (111) direction, i.e. in crystal plane. These two phonon modes are doubly degenerate as eigenvalues λ_1 and λ_2 are equal in magnitude for back-scattering along (111) growth axis. When incident and back-scattered light wavevectors are normal to (111) plane, the LO phonon mode corresponds to the vibrations of the atoms along the (111) direction and will therefore shift (equation (3.2.2b)) as singlet type. On the other hand TO phonon mode corresponds to the vibrations in growth plane and will shift (equation (3.2.2a)) as doublet type. Thus, the strain induced splitting of TO phonon cannot give rise to the observed asymmetry on lower frequency side of TO phonon for Raman back-scattering from (111) surface. However, TO phonon splitting due to biaxial strain should be observable in Raman spectra from CSS, *i.e.*, $[1\bar{1}0]$ or $[11\bar{2}]$ planes in BSG. Also, the optical and AFM image of nucleating and thick layers show that the GaP film has morphological variations (made up of triangular microstructures). Consequently, there is finite possibility of scattering events in the direction different than [111], while Raman spectra is measured from (111) surface of GaP/Ge(111). These scattering events may result in partial deviation from Raman selection rules (RSRs) for BSG from (111) surface of GaP, wherein TO phonons polarized in (111) direction may appear as leakage due to observed morphological variations. Therefore, the difference $\Delta\omega = \omega_{TO(d)} - \omega_{TO(s)}$ is calculated using equations (3.2.2a) and (3.2.2b), which comes out to be within ±1 cm^{-1} for strain values obtained from TO and LO phonon shifts. This difference ($\omega_{TO(d)} - \omega_{TO(s)}$) is much smaller than the observed shift of ~4 cm^{-1}. Because of this inconsistency in the magnitude of red-shift, the possibility of the mode A_2 being the strain-induced split TO phonon is discarded. Furthermore, the Raman spectra from growth surface of both the hetero-structures exhibit position dependent variations in the relative intensity of TO and LO phonons, which may be related to topographical variations in GaP epilayer. This possibility is examined further using spatially resolved polarized Raman measurements, as discussed in the next sub-section.

3.2.2 Correlation between morphology and partial deviation from Raman selection rules (RSRs)

Raman spectra measured from (111) surface in back-scattering geometry at different positions on GaP/Ge(111) thick layer, show variation in the peak intensity of mode A_2 relative to that of TO phonon, *i.e.*, the peak intensity ratios $I(A_2)/I(TO)$ and $I(TO)/I(LO)$ varies spatially over the entire region of the sample. Keeping this in mind, polarization dependent Raman spectroscopy measurements are performed at two different positions on the sample as shown in Fig. 3.2.2(a). Raman tensors for ZB optical phonons having polarization vectors along the sample axes X ≡ $[1\bar{1}0]$, Y ≡ $[11\bar{2}]$ and Z ≡ [111] are obtained (Appendix-B) by performing the suitable matrix transformation from crystallographic basis *i.e.*, x ≡ [100], y ≡ [010] and z ≡ [001] to sample crystal coordinate system. On the basis of these, the expected RSRs for ZB crystal structure (having equivalent directions) in back-scattering configuration, are compiled in Table 3.3.

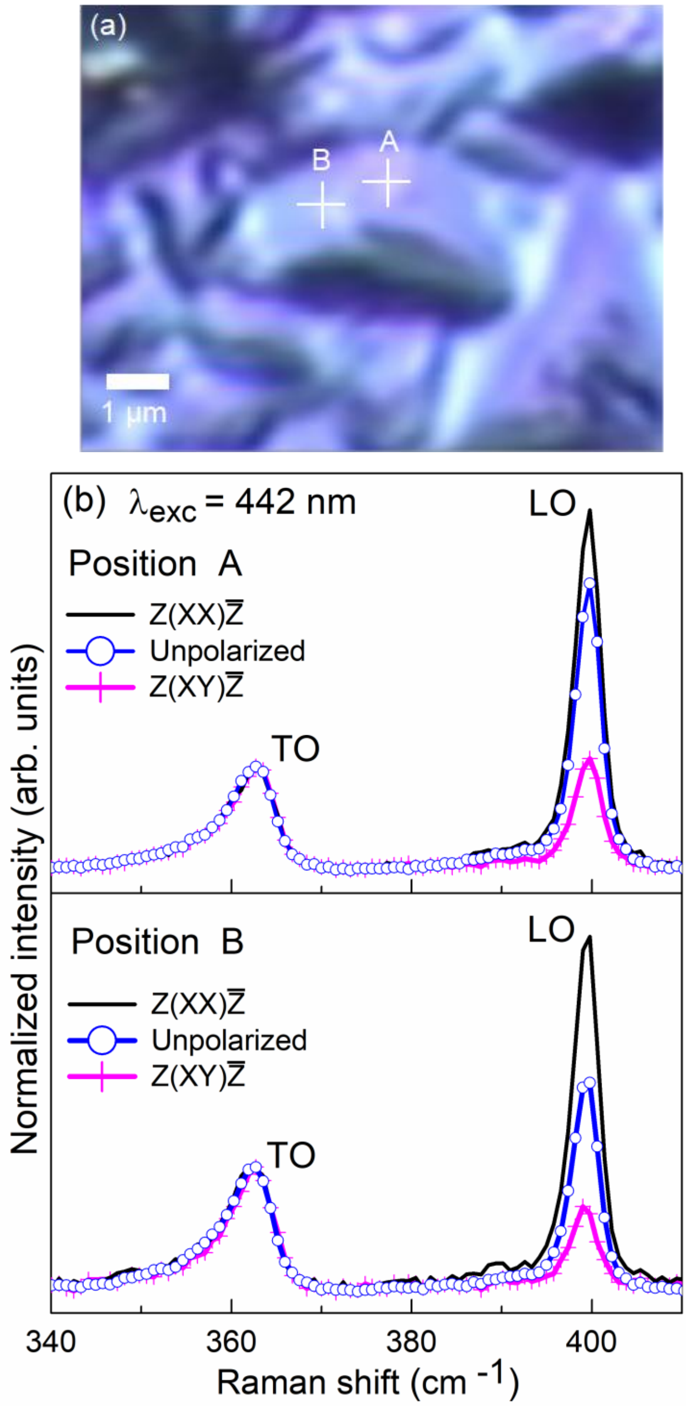

Fig. 3.2.2. *(a) Optical image of GaP/Ge(111) thick layer hetero-structure showing (111) growth surface (b) polarized and unpolarized Raman spectra from (111) surface of thick layer, measured at two different positions marked as A and B in optical image. All the spectra have been normalized with respect to peak intensity of TO phonon.*

Table 3.3. *Raman selection rules (RSRs) for* $\mathbf{q} \approx 0$ *optical phonons of the ZB and WZ type crystals. For ZB crystal,* $X = [1\bar{1}0]$, $Y = [11\bar{2}]$ *and Z = [111] are three crystallographic directions in sample coordinate system. For WZ crystal,* $X = [1\bar{1}00]$, $Y = [11\bar{2}0]$ *and Z = [0001] represent crystallographic directions in sample coordinate system.*

Scattering configuration	Expected modes	
	Zinc-blende	Wurtzite
$Z(XX)\bar{Z}$	TO, LO	E_{2H}, A_1(LO)
$Z(XY)\bar{Z}$	TO	E_{2H}
$X(YY)\bar{X}$	TO	E_{2H}, A_1(TO)
$X(ZZ)\bar{X}$	TO	A_1(TO)

The particular scattering configuration in Table 3.3 is represented using Porto notation [87]. From RSRs in Table 3.3, LO phonon is forbidden in cross polarization configuration $Z(XY)\bar{Z}$, whereas in $Z(XX)\bar{Z}$ configuration both TO and LO are allowed. Therefore, scattering configuration $Z(XY)\bar{Z}$ is chosen to examine the deviation (if any) from RSRs at different sites on the film. However, it may be important to keep in mind that at 442 nm (2.81 eV) laser excitation, resonance Raman enhancement is expected due to its closeness to the direct band gap (2.78 eV) of GaP [86] and therefore LO phonon selection rules may not be exactly followed [102, 103]. The relative peak intensity of LO phonon is less (nearly half) than that of the allowed TO phonon for $Z(XY)\bar{Z}$ geometry, where it is forbidden. In the light of this discussion, it can be comprehended from Fig. 3.2.2(b) that polarization selection rules are nearly followed at position B, and there is deviation from the same at nearby position A. The data acquired at many different positions on thick layer is consistent with these observations. In order to check the same for GaP/Ge(111) nucleating layer hetero-structure, spatially resolved polarized Raman spectroscopy (SRPRS) measurements are carried out at two different sites (Fig. 3.2.3(a)) on GaP microstructure.

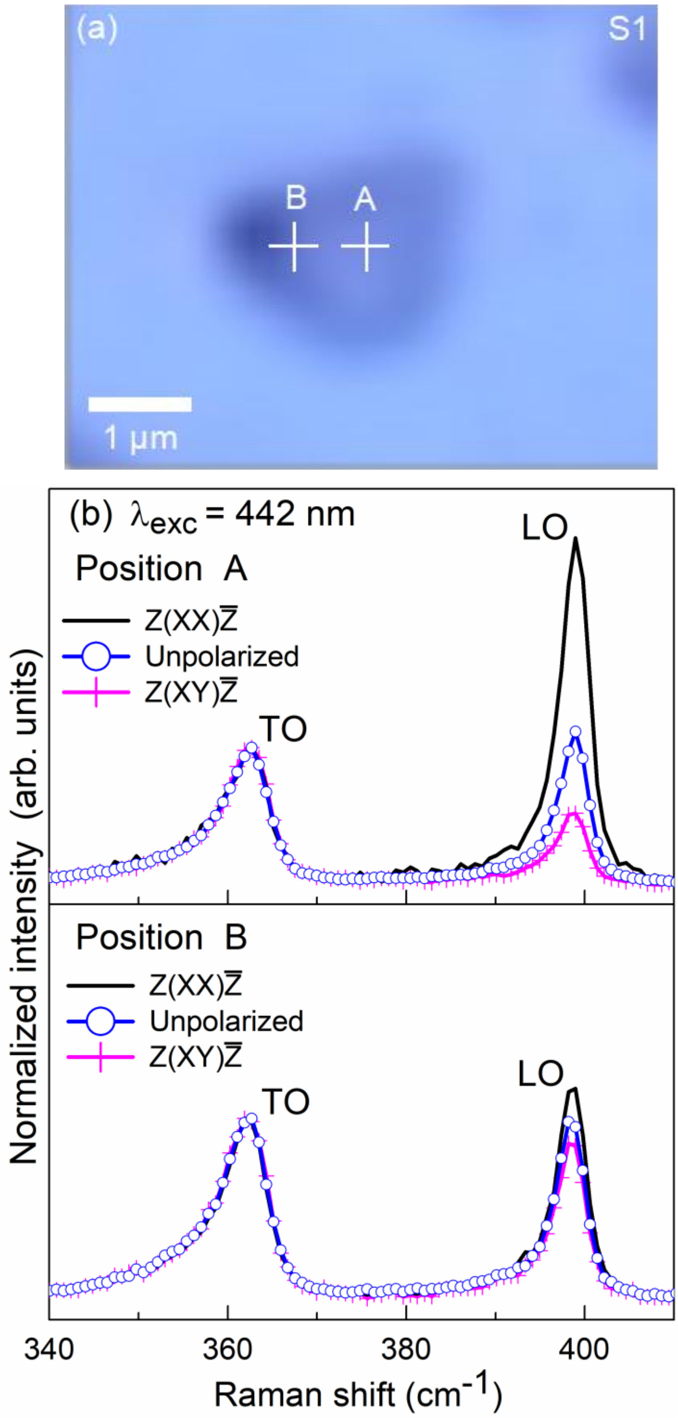

Fig. 3.2.3. *(a) Optical image of GaP/Ge(111) nucleating layer heterostructure showing (111) surface (b) polarized and unpolarized Raman spectra from (111) surface of nucleating layer, measured at two different positions marked as 'A' and 'B' in optical image. All the spectra have been normalized with respect to peak intensity of TO phonon.*

Spatially resolved polarized Raman spectra for the nucleating layer are shown in Fig. 3.2.3(b). Raman spectra from spatial position ‘A’ (marked in Fig 3.2.3(a)), in the central region of the island, show that RSRs are obeyed at this location. However, at position B near the edges of the island, it is apparent from Fig. 3.3.2(b) that the peak intensity ratio I(TO)/I(LO) remains nearly the same for all polarized ($Z(XX)\bar{Z}$, $Z(XY)\bar{Z}$) and unpolarized configurations, evincing that the RSRs are not obeyed. These observations for nucleating and thick layers clearly bring out dependence of Raman spectra on morphology. The correlation between Raman spectra and morphology is further investigated by carrying out Raman and AFM mapping on the same selected region of GaP/Ge(111) layer. Since nucleating layer (Fig. 3.2.3(a)) has well-isolated GaP microstructures, it is more suitable to perform AFM and Raman measurements on the same site. Optical image of the region of GaP nucleating layer chosen for this study is shown in Fig. 3.2.4(a). AFM and Raman mappings of the corresponding region are performed, as explained in chapter 2. AFM and Raman mapping data are shown in Fig. 3.2.4(b) and 3.2.4(c), respectively, which reveal that GaP layer growth occurs in the form of nanostructures (each of size ~400–600 nm) stacked in a group of four, making a trapezoidal shaped structure. Each of the four nanostructures in the trapezoidal shaped stack has nearly pyramidal morphology (Fig. 3.2.4(b)) with side walls having inclination with respect to the surface normal. This peculiar feature has been consistently observed in most of the regions of NL hetero-structure. The possible origin of such structures could be related to formation of microtwins. It is interesting to note that signature of microtwins is observed in HRXRD data too [26]. The surface reconstruction owing to surface energy difference between GaP and Ge may also add to small coalescing islands. This is out of the scope of this thesis and will be looked into separately. The trapezoidal shaped stack of four islands is seen as triangle in Raman spectroscopy mapping (Fig. 3.2.4(c)) data and optical image (Fig. 3.2.4(a)) of the same region.

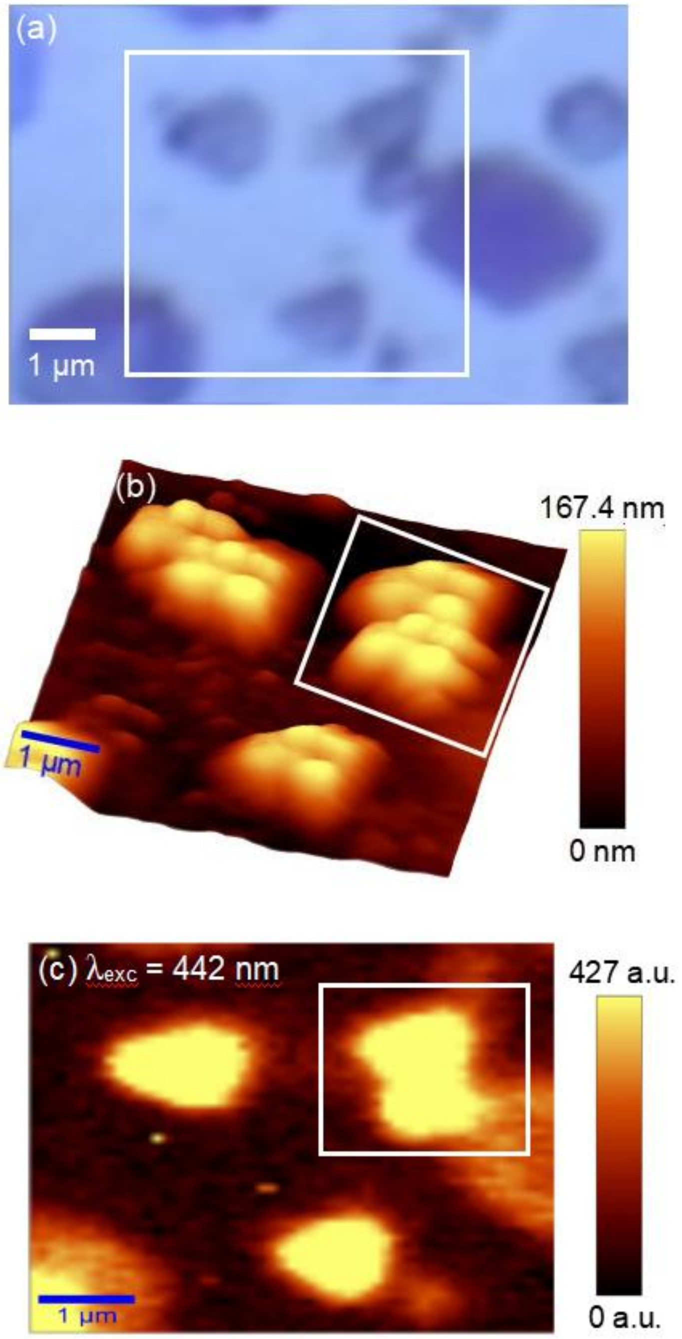

Fig. 3.2.4. *(a) Optical image of GaP/Ge(111) nucleating layer, (b) AFM scan of the rectangle region in (a) showing the formation of trapezoidal shaped stacks, each consisting of four nano-islands and (c) Raman image of the rectangle region in (a), obtained by integrating the intensity of phonon modes in spectral range 332–372* cm^{-1} .

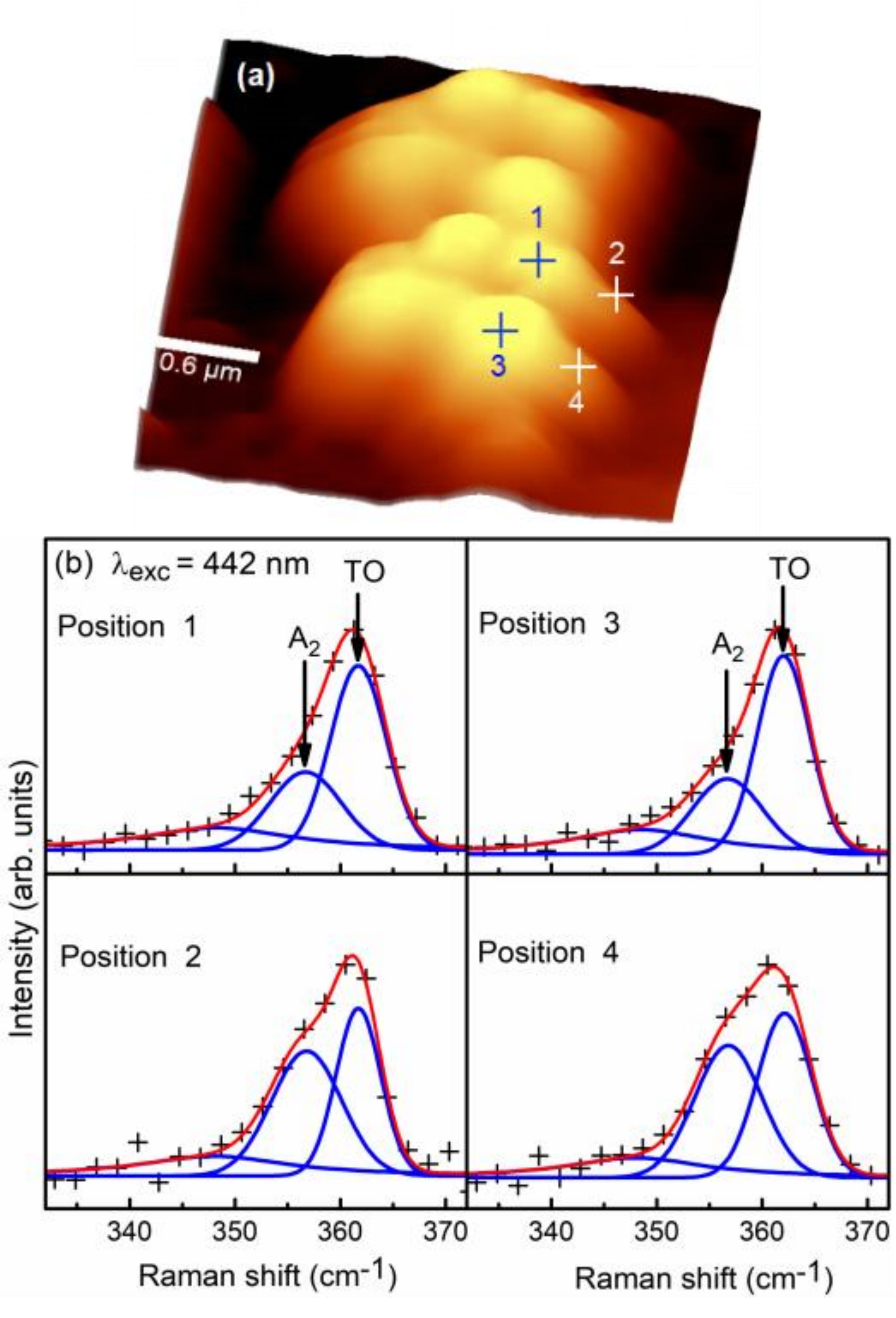

Fig. 3.2.5. *(a) AFM scan of the region of GaP/Ge(111) nucleating layer marked by rectangle (white) in Fig. 3.2.4(b), (b) Comparison of Raman spectra arising from the positions '1' and '3' having planar morphology with that from the sites '2' and '4' having inclined morphology, showing the increase in the relative intensity of mode* A_2 *w.r.t. the TO phonon.*

One to one correspondence of GaP nanostructures is clearly evident from optical (Fig. 3.2.4(a)), AFM (Fig. 3.2.4(b)) and Raman (Fig. 3.2.4(c)) images. Observed Raman spectra at four different spatial positions denoted by the numbers from ‘1’ to ‘4’ in Fig. 3.2.5(a) are shown in Fig. 3.2.5(b). The spatial positions ‘1’ and ‘3’ are at the center of each of the four nanostructures, whereas the positions marked by ‘2’ and ‘4’ are located on the inclined side walls. It can be clearly observed that the peak intensity of phonon mode A_2 relative to that of TO phonon increases, as we go from planar surface to the regions of inclined morphology. This observation is true for other similar positions in the AFM image. Similar experiments have been carried out at more such sites in the nucleating layer to discover the same morphology dependent variations in spectral features. Correlation between morphology and peak intensity variation of phonon mode A_2, suggests that there is a contribution from crystal planes other than (111) and/or near interface region. This stimulated the investigation of cross-sectional surface (CSS) of GaP/Ge(111) hetero-structures as discussed in next sub-section.

3.2.3 Investigation of polytypism using Raman mapping and spatially resolved polarized Raman spectroscopy

To obtain further insight into the origin of phonon mode A_2, CSS of GaP/Ge(111) thick layer hetero-structure is mapped along the interface (‘Y’ direction in Fig 3.2.6(a)), integrating the spectral range (332-372 cm^{-1}) containing TO phonon and asymmetric feature (A_2) on its lower frequency side. Fig. 3.2.6(a) represents the schematic of Raman scattering from CSS of thick layer hetero-structure, and the corresponding Raman spectral map of the CSS is shown in Fig. 3.2.6(b). Raman spectra arising from three positions, as marked in Fig. 3.2.6(b), are shown in Fig. 3.2.6(c).

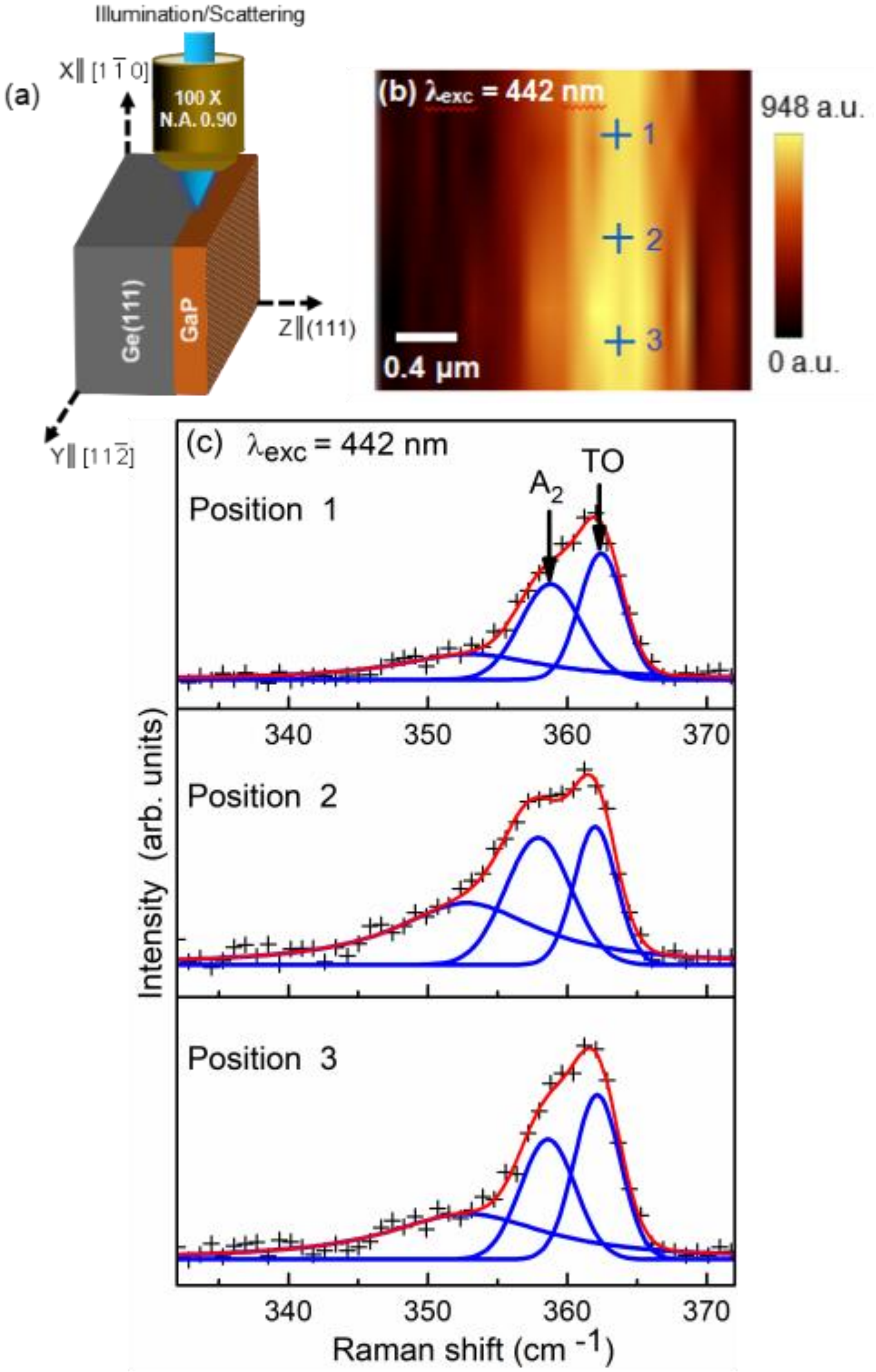

Fig. 3.2.6. *(a) Schematic diagram of Raman scattering from cross-sectional surface, (b) Raman image of phonon modes in spectral range 332–372 cm^{-1}, as obtained from mapping of cross-sectional surface (GaP-Ge interface) of thick layer hetero-structure along the direction 'Y' in (a). (c) Raman spectra recorded at three different positions marked (along 'Y') in the Raman image shown in (b). Deconvolution of contributions to Raman spectra shows the intensity of mode* A_2 *relative to that of TO phonon.*

It is important to note that prominent phonon mode A_2 with nearly same intensity as that of TO phonon is observed in all Raman spectra presented in Fig. 3.2.6(c). Since mode A_2 has strong presence in cross-sectional geometry, it is decided to investigate this further by performing the spatially resolved Raman measurements from CSS, along the depth of thick layer. The important observation from spatially resolved Raman (Fig. 3.2.7) measurements performed on CSS is that the line-shape and frequency of TO and LO phonon bands for sites near GaP-Ge interface (NI) and away from GaP-Ge interface (AI) are very different. In addition to TO phonon ~358 cm^{-1} and LO mode ~397 cm^{-1}, the In NI Raman spectra (Fig. 3.2.7(a)) register the significant presence of modes ~351 cm^{-1} and ~394 cm^{-1}. It should also be noted from Fig. 3.2.7(a) that the TO and LO phonon frequencies are different than those observed for scattering from (111) surface. Further, Figure 3.2.7(b) shows that Raman spectra from AI region of CSS resembles the spectra obtained from (111) surface of GaP/Ge(111), both in frequency and line-shape. Similar to Raman spectra observed from (111) surface, the AI spectra (Fig. 3.2.7(b)) from CSS has mainly the TO (~362 cm^{-1}) and LO (~399 cm^{-1}) phonons with asymmetric feature on low frequency side of both the modes. The possible causes of this spatial dependence of Raman spectra and observance of additional phonons are considered to be: (1) variation in composition/strain and/or (2) change in crystal phase occurring along the depth of GaP layer. Polarized Raman spectroscopy is expected to give more insight into the same. Out of the two possibilities mentioned above, former is not expected to influence the polarization dependent Raman spectra. However, the effect of change in crystal structure can be easily detected through polarized Raman spectroscopy. It may be recollected here that the magnitude of the splitting of TO phonon due to biaxial strain is much smaller than observed difference between frequencies of A_2 and TO phonon (Fig. 3.2.1) modes. In addition to this, there exist reports suggesting the possibility of existence of wurtzite (WZ) crystal structure at the interface of III-V/Si and III-V/GaAs hetero-structures [84, 104, 105].

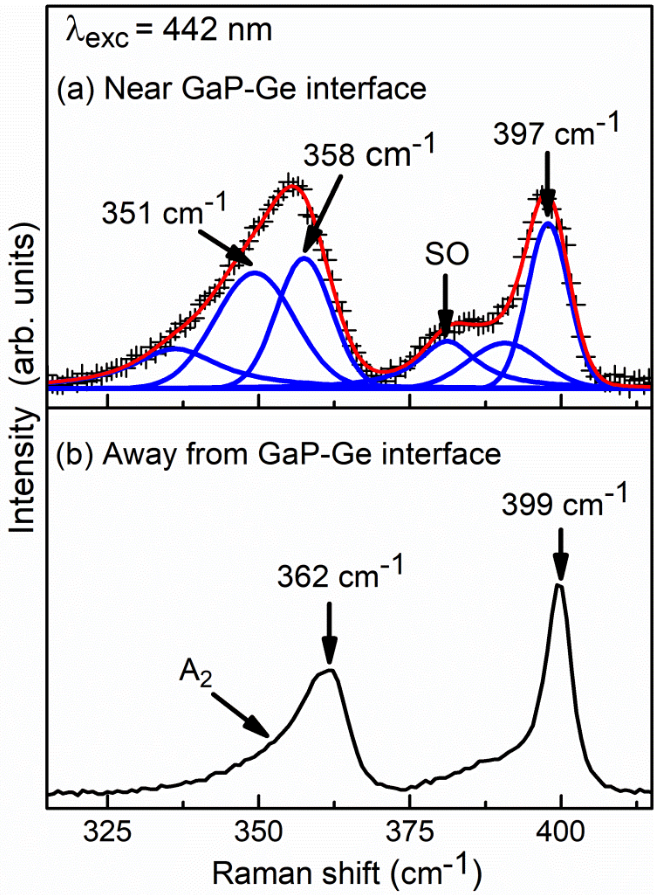

Fig. 3.2.7. *Unpolarized Raman spectra in backscattering geometry arising from (a) near GaP–Ge interface (NI) site and (b) away from interface (AI) region of the cross-sectional surface of GaP/Ge(111) thick layer hetero-structure.*

Keeping this in mind, SRPRS measurements are performed on CSS of thick layer hetero-structure in polarization configurations $X(YY)\bar{X}$ and $X(ZZ)\bar{X}$ [49], which can reveal the existence of WZ crystal phase (if any), under epitaxial growth along ZB (111) direction. It is noteworthy that the (111) crystallographic direction of ZB crystal is equivalent to (0001) of WZ, as the atomic arrangements along these two directions are closely similar. Consequently, for a WZ/ZB crystal structure, X, Y and

Z axes represent the crystallographic directions $[1\bar{1}00]/[1\bar{1}0]$, $[11\bar{2}0]/[11\bar{2}]$ and [0001]/[111], respectively. It can be deduced from selection rules in table 3.3 that for Raman back-scattering from CSS, the two polarization configurations *i.e.*, $X(YY)\bar{X}$ and $X(ZZ)\bar{X}$ can unambiguously resolve the contribution of WZ and ZB phases to Raman spectra. Therefore, the afore specified configurations are chosen to discern the presence of WZ phase (if any) and hence explicate the spatial dependence of Raman spectra as observed in Fig. 3.2.7. Figure 3.2.8 shows Raman spectra arising from NI and AI sites in scattering configuration $X(YY)\bar{X}$. For this configuration, both E_{2H} (WZ) and TO (WZ and ZB) phonons, which lie close in frequency, are allowed (Table 3.3) and indeed observed in Raman spectra in Fig. 3.2.8. Although, LO phonons are forbidden in configuration $X(YY)\bar{X}$, they appear due to resonant Raman scattering. Two LO phonon peaks and two phonons (*i.e.*, E_{2H} and TO) can indeed be observed from NI site, whereas, only one dominant TO and one LO phonon with asymmetry on low frequency side are observed in Raman spectra from AI region as shown in Fig. 3.2.8. Raman spectra in Fig. 3.2.8 is thus strongly indicative of change in crystal phase of GaP from interface to surface of GaP/Ge(111) hetero-structure. Considering the presence of WZ crystal structure, the mode ~360 cm^{-1} in Fig. 3.2.8 is expected to have superposition of E_{2H} (WZ) and TO (WZ, ZB) phonons. The change in relative peak intensities of these phonons due to difference in content of WZ and ZB is expected to influence not only their lineshape, but also the frequency of these modes in different polarization configurations. Although, similar effect is already observed in Fig. 3.2.8, the basic difference is that Raman spectra shown in Fig. 3.2.8 stem from different sites (and in same same polarization configuration), wherein, at one position WZ and at other the ZB phase GaP is probably the dominant crystal structure.

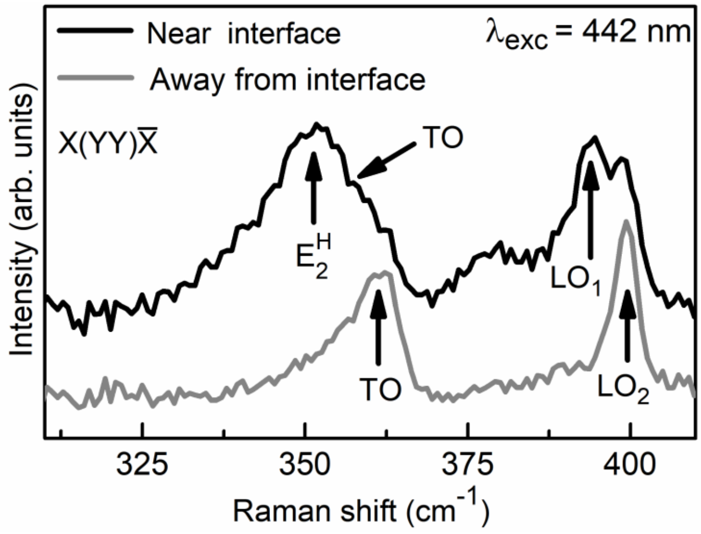

Fig. 3.2.8. *Polarization dependent Raman spectra arising from near GaP–Ge interface (NI) site and away from interface (AI) site of cross-sectional surface of GaP/Ge(111) thick layer hetero-structure, in scattering configurations* $X(YY)\bar{X}$.

However, the underlying cause of the observed effect is the same; in one condition (*i.e.*, WZ phase) both E_{2H} and TO phonons are observed, and in other (*i.e.*, ZB phase) only TO phonon is present. This is further confirmed by performing the SRPRS measurements in polarization configuration $X(ZZ)\bar{X}$, and comparing it with Raman spectra in $X(YY)\bar{X}$ configuration. Polarization dependent Raman spectra measured at different positions, *i.e.*, NI and AI regions in both scattering configuration are shown in Fig. 3.2.9(a) and (b), respectively. During the measurements, the scattering configuration is changed from $X(YY)\bar{X}$ to $X(ZZ)\bar{X}$ by placing the sample on a sample rotator and rotating it by an angle of 90◦. Figure 3.2.9(a) shows that the phonon mode ~351 cm^{-1} indeed shifts by ~7 cm^{-1} from ~351 cm^{-1} to ~358 cm^{-1} on changing scattering configuration from $X(YY)\bar{X}$ to $X(ZZ)\bar{X}$. Further, the line-shape of two phonons in Fig. 3.2.9(a) also suggest the strong presence of E_{2H} phonon (A_2 mode) in $X(YY)\bar{X}$ configuration for NI Raman spectra (Fig. 3.2.9(a)) in accordance with the RSRs for WZ and ZB structures (Table 3.3).

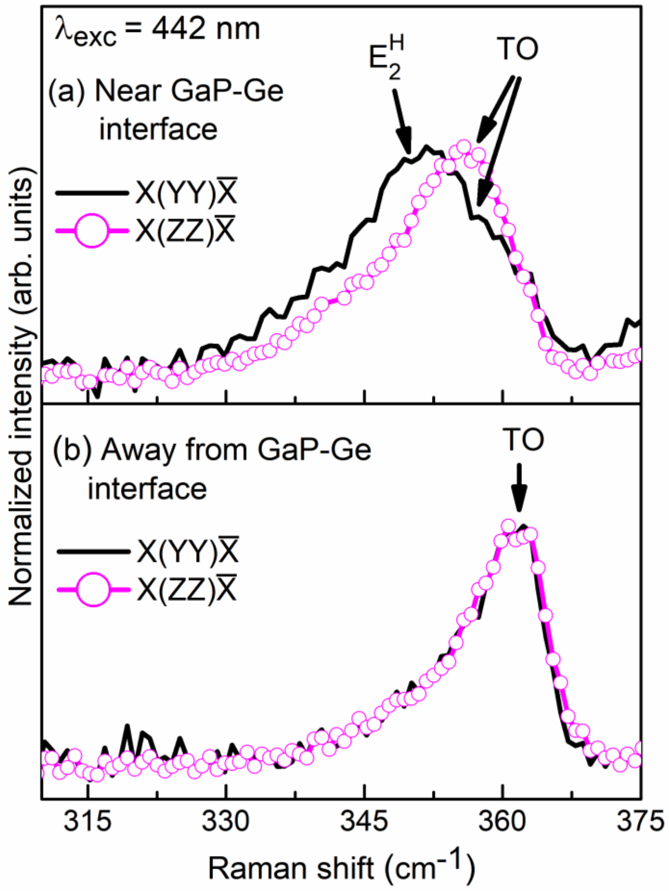

Fig. 3.2.9. *Polarized Raman spectra (range: 310–375 cm^{-1}) arising from (a) near GaP–Ge interface (NI) site and (b) away from interface (AI) site of cross-sectional surface of GaP/Ge(111) thick layer hetero-structure, in scattering configurations* $X(YY)\bar{X}$ *and* $X(ZZ)\bar{X}$.

This establishes the coexistence of WZ and ZB phases with dominance of WZ phase of GaP near the GaP-Ge interface. Accordingly, we attribute the lower (A_2) and higher frequency (TO) phonons in Figs. 3.2.5 and 3.2.6 to E_{2H} phonon of WZ and TO phonon of WZ and ZB phases, respectively. It is also important to note that there is no change in Raman spectra arising from AI site for both these polarization configurations, as shown in Fig. 3.2.9(b), suggesting the presence of mainly the ZB structure in this region. In view of this understanding, it is interesting to look at the observed Raman spectra in the spectral range 310–410 cm^{-1}, showing both TO and

LO phonon (Fig. 3.2.8). The spectra from NI site show two LO phonons, whereas only one strong LO phonon is observed in Raman spectra from AI site.

Thus Raman spectroscopy and AFM study of GaP/Ge(111) confirms the coexistence of two crystalline phases of GaP in these hetero-structures, with dominance of WZ phase near GaP-Ge interface and that of ZB phase near the surface.

3.2.4 Recapitulation of Raman spectra from (111) surface of GaP/Ge(111) in the light of polytypism

The polytypism observed in GaP layer grown on Ge(111) can now consistently explain the partial deviation from RSRs, as observed for backscattering from (111) surface of GaP. The phonon mode E_{2H} (~351 cm^{-1}) observed in Raman spectra arising from near GaP-Ge interface region (in scattering from CSS) gives rise to the asymmetry on low frequency side of ZB-TO phonon (~362 cm^{-1}) as seen (Fig. 3.2.1) in Raman spectra from (111) surface. This can be attributed to the Raman signal being picked up from WZ phase dominant near the interface. Also, the relatively small asymmetry observed (B_2 mode in Fig. 3.2.1) on lower frequency side of LO phonon is the LO phonon arising from WZ structure and is forbidden in back-scattering from (111) surface. Partial deviation from RSRs, as observed in the SRPRS measurements in Fig. 3.2.3 and 3.2.4 are now understood to be the result of the combined effect of the morphological variation and the presence of WZ phase near the interface. Morphological dependence of the peak intensity of A_2 phonon, as shown in Fig. 3.2.5, can also be explained as due to Raman signal being picked up from CSS (near interface region) on the inclined morphology. Also, Figure 3.2.7 shows that the frequencies of TO and LO phonons observed in Raman spectra from NI (TO ~358 cm^{-1} and LO ~397 cm^{-1}) and AI (TO ~362 cm^{-1} and LO ~399 cm^{-1}) sites are different. This can be explained in terms of the further red-shift of ZB phonon due to presence of WZ phase in the near interface region. This effect has been discussed in detail by

Gupta et. al., [49], wherein the spatially resolved Raman spectroscopy measurements on InAs nanowires, having mixed (WZ and ZB) crystal structures, are presented. Also, Raman spectra (Fig. 3.2.7) from NI site exhibit a red-shift in frequency of surface optical (SO) phonon as compared to that from AI region. Frequency of surface optical phonon depends on the TO mode frequency and dielectric constant of surrounding medium [106]. For NI region, TO phonon frequency is lower (Fig. 3.2.7) and dielectric constant of surrounding medium is higher than that for AI site, which give rise to the observed red shift in SO phonon frequency. The Gaussian profile of the phonons (A_2, TO, B_2 and LO) of GaP can also now be understood in the light of the above discussion. This is attributed to the presence of different structural phases of ZB and WZ structures with dominance of WZ phase near the interface and the variation being random in nature. It is noteworthy to mention that III–V semiconductor nanowires have been found to crystallize in pure WZ or mixed (WZ and ZB) phase for certain growth conditions and dimensions [107-110]. Also, recently, the growth of phase-pure WZ GaP nanowires (diameter ~80 nm) has been reported by Assali *et al*., [111]. However, to the best of our knowledge, the co-existence of WZ and ZB crystal phases in microstructured GaP/Ge layer has not yet been reported. Only single other report by *Narayanan et al*. [84] on GaP/Si(111), shows (using high resolution TEM) the presence of mixed (WZ and ZB) phases of GaP for ~30 nm islands.

Furthermore, while examining the interfacial properties of GaP epilayer in GaP/Ge(111) hetero-structures, it is also noticed that spectral features originating from the underlying Ge substrate have substantial deviations from that of pure bulk Ge wafer. The cause of such a behavior of substrate layer, particularly in nucleating layer hetero-structure, is investigated using Raman spectroscopy and is discussed in the next section.

3.3 Inter-diffusion across the hetero-interface in GaP/Ge(111) hetero-structures

Figure 3.3.1 shows the Ge-optical phonon Raman spectra stemming from Ge substrate of nucleating (NL) and thick layer (TL) GaP/Ge(111) hetero-structures. For comparison, Raman spectrum of Ge(111) wafer, which is used as substrate for the growth of GaP epilayer, is also shown in Fig. 3.3.1(a).

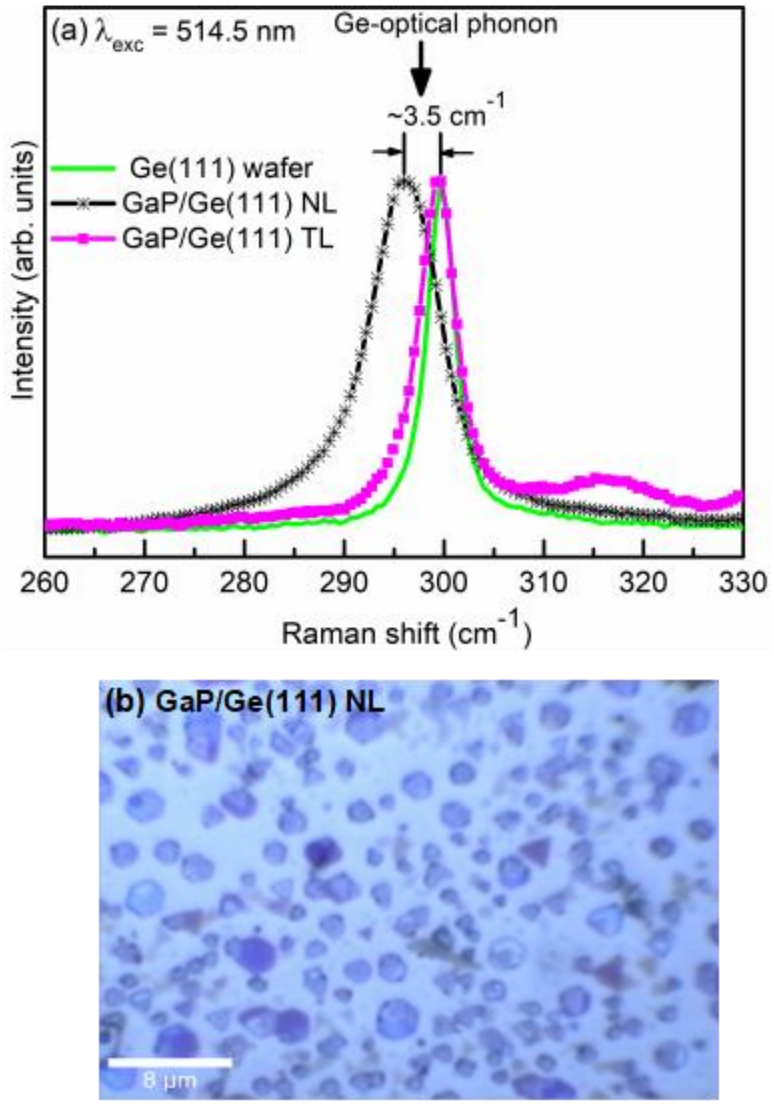

Fig. 3.3.1. *(a) Raman spectra of GaP/Ge(111) nucleating layer (NL), thick layer (TL) and Ge(111) wafer, showing the red-shift and broadening of Ge-optical phonon of GaP/Ge(111) NL hetero-structure (b) optical image of NL.*

Most of the Raman spectroscopy measurements (in back-scatteing geometry) are performed using SPM-Raman integrated system (*Alpha 300S*). Stokes/anti-Stokes Raman measurements are performed using Trivista triple Raman spectrograph system *TR557*. The excitation wavelengths used are 488 nm, 514.5 nm (Ar ion laser) and 633 nm (He-Ne laser). For Raman data at 633 nm excitation, LabRAM HR800 (Horiba Scientific) Raman spectrometer is used. The wavenumber per pixel of Raman spectrograph at the laser excitations used is in the range ~0.3-0.5 cm^{-1}. The laser power density at the sample surface is kept constant for recording all the Raman data presented in this work.

It is observed that frequency of Ge-optical phonon arising from thick layer hetero-structure is close to that of Ge wafer. Ge-optical phonon of Ge(111) wafer is observed ~300 cm^{-1}, having FWHM ~3-4 cm^{-1}. Ge optical phonon arising from thick layer shows spatial variation of ±1 cm^{-1} in frequency, and its FWHM lies in the range ~4-5 cm^{-1}. However, the GaP/Ge(111) nucleating layer registers highly intriguing and deviant spectral features, wherein, Ge optical phonon is observed at ~296 cm^{-1} (red shift from the bulk value ~300 cm^{-1}) with large FWHM ~8 cm^{-1}, almost twice that of Ge wafer and thick layer. Therefore, the possible causes for the origin of anomalous behavior of underlying Ge substrate are discussed in the following sub-section.

3.3.1 Heating and spatial correlation effects: Broadening and softening of Ge optical phonon mode

Raman spectra of NL hetero-structure, which is grown at ~425°C with V/III ratio ~1725, show that disorders are introduced in Ge layer, leading to significant reduction in the lifetime of Ge-optical phonon. However, during the second step of MOVPE growth, wherein growth temperature is raised to ~770°C and V/III ratio is decreased to ~100, there is substantial improvement in crystalline quality of Ge layer (Fig. 3.3.1(a)) as inferred from the the behavior of Ge-optical phonon of TL. The

GaP/Ge(111) NL consists of isolated GaP micro-structures as seen in the optical image (Fig. 3.3.1(b)). The region surrounding isolated GaP micro-structures does not show any signature of GaP, even with higher laser power, and for resonance Raman scattering at 442 nm excitation. It is interesting to note that the Ge-optical phonons arising from both of these regions of the NL hetero-structure have same frequency and line-shape. The possible causes of red-shift and large FWHM of Ge-optical phonon of NL GaP/Ge hetero-structure are considered as,

(1) Temperature dependent broadening and red-shift due to laser heating of Ge substrate, as the substrate is covered by GaP and not directly exposed to air. This may cause the inefficient heat removal as compared to that for substrate in contact with air, leading to increase in substrate temperature.

(2) Structural ordering of the sub-nano dimensional size (correlation length) in the Ge substrate could give rise to downshift and broadening of phonon spectra through the relaxation of |***q***|=0 momentum selection rules.

In the following, first possibility *i.e.*, laser induced heating (if any) of the underlying Ge susbtrate is discussed. To investigate whether laser heating effectuates the red-shift and broadening of Ge optical phonon, we perform Stokes-anti Stokes (S-AS) Raman measurements for Ge-optical phonon of the Ge wafer and NL sample. S-AS Raman spectra of Ge optical phonon is shown in Fig.3.3.2. Temperature (T) from S-AS Raman spectra can be calculated using following equation:

$$\frac{I_s}{I_{as}} = \frac{\left(\omega_i - \omega_{ph}\right)^4}{\left(\omega_i + \omega_{ph}\right)^4} \exp\left(\frac{\hbar\omega_{\mathrm{ph}}}{kT}\right)$$

where, I_S, I_{AS}, ω_{ph}, ω_L are Stoke intensity, anti-Stoke intensity, Ge optical phonon energy and excitation laser energy respectively. From above equation, the calculated value of temperature for NL and Ge(111) wafer is ~350 K.

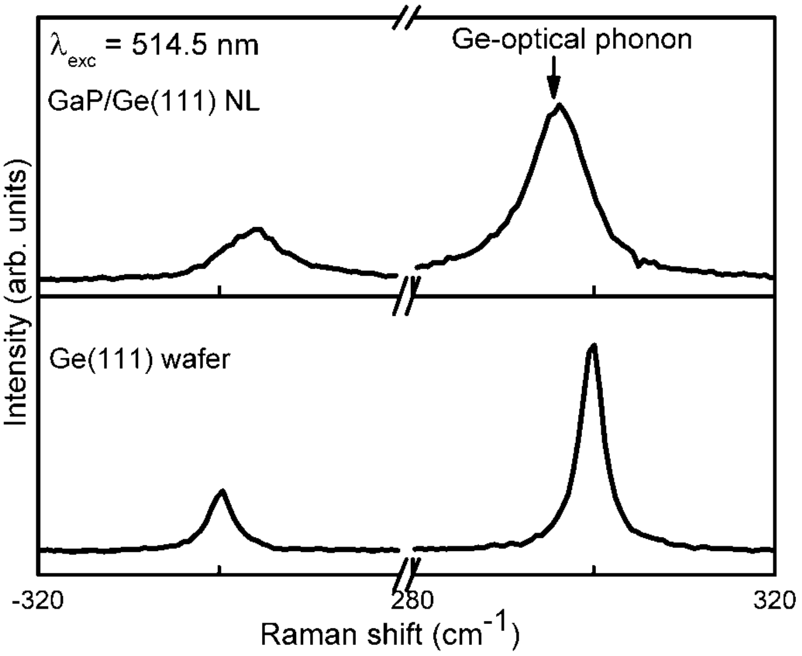

Fig. 3.3.2. *Stoke-anti Stoke Raman spectra of Ge-optical phonon of GaP/Ge(111) NL and bulk Ge(111) wafer.*

Calculation shows that temperature estimated from S-AS Raman measurement is in the vicinity of room temperature and has nearly the same magnitude for both NL and Ge wafer. Therefore, this analysis demonstrates that the laser irradiation of germanium layer during Raman measurement is not responsible for the observed broadening and softening of Ge-optical phonon.

Although the observed line-shape of phonon ~296 cm^{-1} is nearly symmetric, it's large FWHM and red-shifted wavenumber are analyzed using spatial correlation model (SCM), by taking into account structural disorders (if any) existing beyond some correlation length (*L*) in the substrate layer [112, 113]. Using the Gaussian weighting function, natural line width of Ge-optical phonon (of bulk wafer) and appropriate phonon dispersion function for Ge [113], line-shape of the Ge-optical phonon is simulated for different correlation length values. Figure 3.3.3 shows SCM profile of Ge-optical phonon obtained for different correlation length values. However, the observed line-shape (also shown in Fig. 3.3.3) and its FWHM cannot be reproduced with SCM profile calculated for different spatial correlation lengths ranging from 300 nm, 30 nm, 20 nm and 15 nm. The calculated FWHM of phonon mode for correlation length 15 nm is closer to observed FWHM, but line-shape has a large asymmetry. Therefore, the observed line-shape and red-shift of Ge-optical phonon arising from disordered region of Ge substrate cannot be delineated using the SCM.

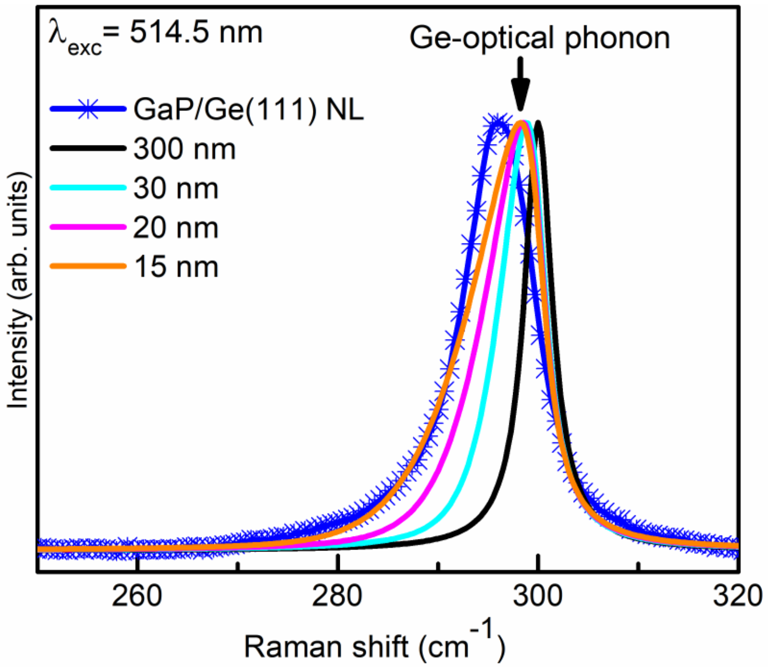

Fig. 3.3.3. *Spectral line shape of Ge-optical phonon obtained using spatial correlation model for different correlation lengths. The observed spectra of GaP/Ge(111) NL is also plotted for comparison.*

In the absence of heating and spatial correlation effects, another nearest possibility for the observed behavior of Ge layer could be the disorder generated due to inter-diffusion of the elements constituting the substrate and/or epilayer (Gallium/Phosphorous) at the GaP-Ge hetero-interface. This possibility is discussed in the next sub-section.

3.3.2 Wavelength dependent Raman spectroscopy: A clue to inter-diffusion

The possibility of Inter-diffusion of substrate and epilayer elements at the hetero-interface is considered in the succeeding discussion. Owing to earlier study on diffusion in Ge [114], and large V/III ratio employed during the MOVPE growth (step-I) of GaP/Ge NL hetero-structure, the Gallium diffusion in Ge is less probable. However, the diffusion of phosphorous is expected to be dominant. Raman spectra of NL hetero-structure and Ge(111) wafer are deconvoluted using a Lorentzian profile and the same is shown in Fig. 3.3.4. It is evident that Ge optical phonon of Ge wafer has Lorentzian line-shape, however the corresponding optical phonon arising from NL cannot be fitted with a Lorentzian. This point will be discussed later in this section.

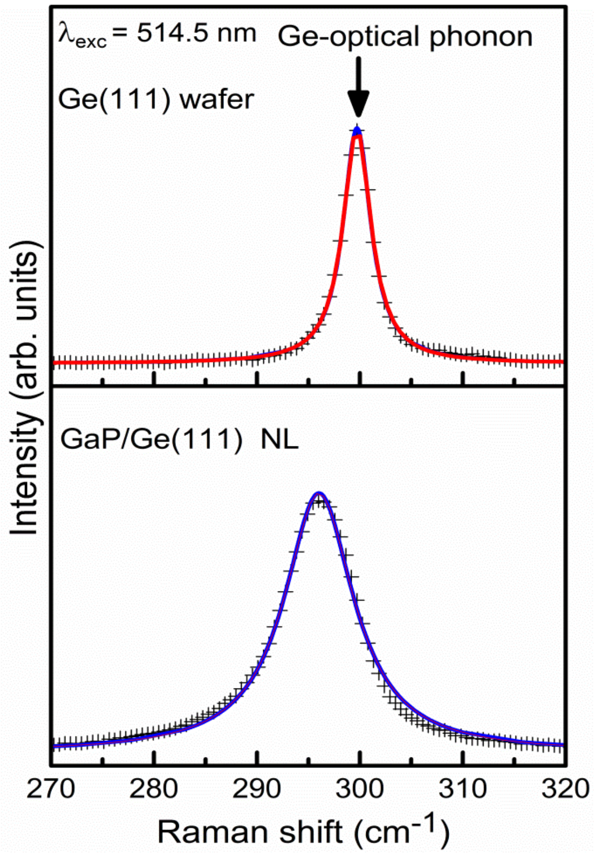

Fig. 3.3.4. *Deconvolution of Ge optical phonon of Ge(111) wafer and GaP/Ge(111) NL using minimum required Lorentzians. The curves fitted to data (+) show the total fit.*

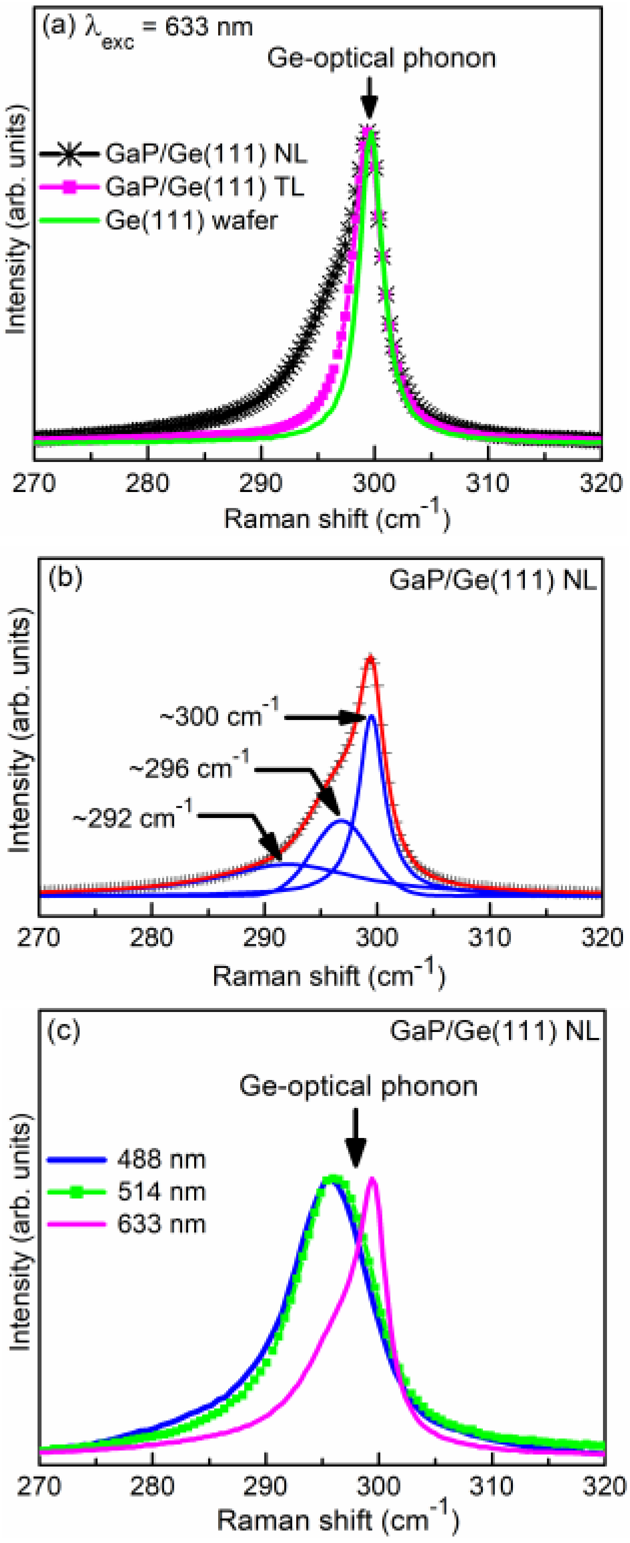

Fig. 3.3.5. *(a) Raman spectra of GaP/Ge(111) NL, TL and Ge(111) wafer at 633 nm laser excitation (b) Deconvolution of contributions to Raman spectra (shown in (a)) of NL sample using minimum required Lorentzian and Gaussian. Red color fit to data (+) shows the total fit. (c) Comparison of Raman spectra of NL at three different excitation wavelengths.*

It is important to note here that only a limited depth in Ge layer can be probed using 514.5 nm laser excitation, since its penetration depth in Ge is ~17 nm. Therefore in order to probe deeper in Ge layer, Raman measurements on NL, TL and Ge(111) wafer are performed at higher laser excitation wavelength *e.g.*, 633 nm, for which the penetration depth in Ge is ~ 52 nm. Figure 3.3.5(a) shows Raman spectra of all the three samples, wherein, wafer and TL have similar spectra as that at 514.5 nm excitation. However, Raman spectra from the Ge substrate of NL is deconvoluted (Fig. 3.3.5(b)) into three phonon modes: 1) phonon mode ~296 cm^{-1}, which has the same line shape, frequency and FWHM as the one observed at 514.5 nm excitation. Another important observation is that this phonon mode can be best fitted with a Gaussian, which suggests inhomogeneity near the hetero-interface, 2) An additional mode (in comparison to that at 514.5 nm spectra) is observed ~300 cm^{-1}, fitted using a Lorentzian, and 3) phonon mode ~292 cm^{-1} having the Lorentzian profile may be the disorder activated phonon. The additional phonon mode observed ~300 cm^{-1} has same frequency and FWHM as that from Ge(111) wafer. This along with the appearance of Ge wafer phonon ~300 cm^{-1} (for 633nm excitation) indicates that the region upto ~17 nm (penetration depth of 514.5 nm in Ge) or more in Ge, near the hetero-interface, is affected during MOVPE growth of NL heterostructure. More accurate estimation of altered depth of Ge (111) substrate (of NL) can be obtained from the relative peak intensity of two phonon ~296 cm^{-1} and ~300 cm^{-1}. From the peak intensity ratio of two modes, the altered depth of Ge substrate is calculated to be ~20 nm. However, Ge-optical phonon of TL hetero-structure is observed at the same spectral position, and has similar FWHM as that for 514.5 nm. Further, Figure 3.3.5(c) shows the comparison of Raman spectra arising from Ge substrate of NL at three different excitation wavelengths, which clearly demonstrates the contributions from affected and non-affected regions of the underlying substrate.

Thus Raman measurements at 488 nm, 514.5 nm and 633 nm laser excitations suggest that shallow germanium layer (~20 nm thick) near hetero-interface is getting affected during the growth of nucleating (step I) layer, which further endorses the possibility of inter-diffusion at GaP-Ge interface. This is explored into further by providing thermal treatment to GaP/Ge(111) hetero-structures as described in the next sub-section.

3.3.3 Thermal treatment of hetero-structures: substantiation of inter-diffusion

The thick layer GaP/Ge(111) hetero-structure grown at ~770°C during the step-II of MOVPE growth, shows the recovery of affected Ge layer near the hetero-interface. Considering this, thermal treatment is performed on NL, TL hetero-structures and Ge wafer at ~500°C and ~700°C. All three samples are subjected to thermal treatment under Argon/N_2 atmosphere as described in the following:

(1) First, all three samples are thermally treated (rapid thermal annealing: RTA) at ~500°C for 20 seconds under Nitrogen atmosphere. The same procedure was repeated three times, making the total annealing duration ~60 seconds.

(2) Parts of the same set of samples are thermally treated at ~700°C for 20 minutes under Argon atmosphere.

Figure 3.3.6(a) and (b) show Raman spectra of NL, TL and Ge(111) wafer, thermally treated at ~500°C and ~700°C, respectively. At ~500°C, no significant change is observed in phonon frequency and FWHM of Ge-optical phonon for all three samples (Fig. 3.3.6(a)). However, due to thermal treatment at ~700°C (Fig. 3.3.6(b)), the Ge-optical phonon of NL hetero-structure gets blue shifted to that of

Ge(111) wafer along with the significant reduction (from ~8 cm^{-1} to ~3 cm^{-1}) in its FWHM.

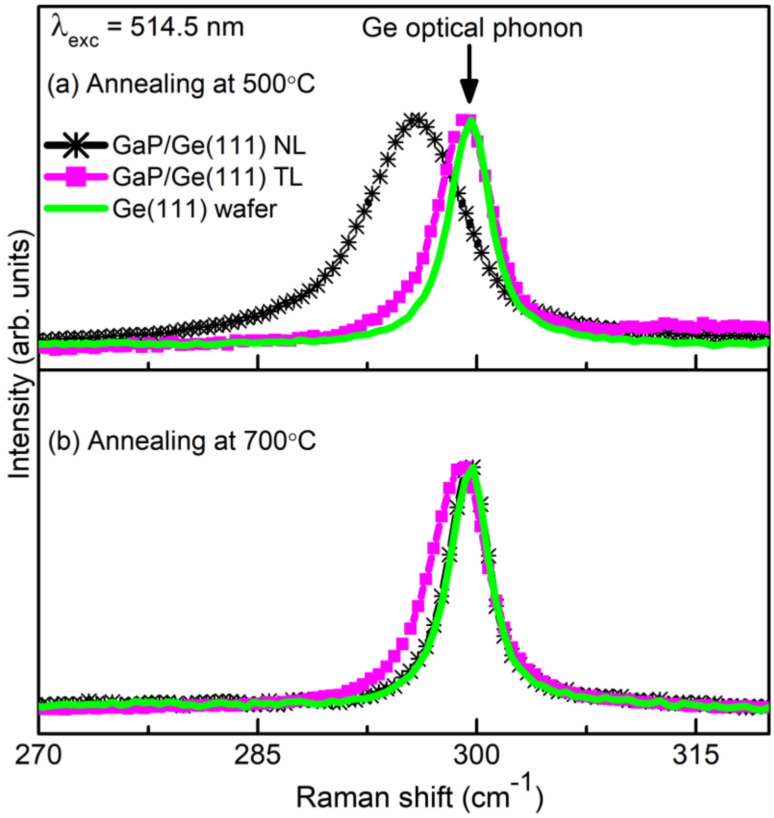

Fig. 3.3.6. *Raman spectra of GaP/Ge(111) NL, TL and bulk Ge(111) wafer, thermally treated at (a) 500°C for 60 seconds and (b) 700°C for 20 minutes.*

The Ge-optical phonon arising from TL sample does not show any significant change in frequency and FWHM as evident from Raman spectra in Fig. 3.3.6(b). This suggests that the thermal treatment at ~700°C, which is close to the growth temperature of TL, results in ordering of the affected shallow region (~20 nm) of the Ge wafer of nucleating layer hetero-structure. This observation substantiates the plausibility of inter-diffusion at GaP-Ge interface leading to disordered shallow Ge layer. Different mechanisms, whereby the inter-diffusion leading to the disordered hetero-interface and consequently the phonon mode ~296 cm^{-1}, may take place are elucidated in next sub-section.

3.3.4 Possible mechanisms for inter-diffusion

Depending on the growth kinetics and inherent properties of the host crystal lattice, the diffusion of epilayer and/or substrate elements could take place across the hetero-interface of GaP/Ge(111). Therefore, we evaluate the cause of the anomalous disordering of a small volume of Ge substrate, taking into account the diffusion of Ge and Ga/P elements at the GaP-Ge interface:

(1) **Out-diffusion of Ge:** It is reported that Ge out-diffusion, during the epitaxial growth of III-V/Ge hetero-structure, is predominant at the growth temperature >500°C and can be controlled to a great extent by carrying out the MOVPE growth at low temperatures [63, 115]. This is because Ge diffuses into III-V (e.g., GaAs) layer via Ga vacancies left by the out-diffusion of Ga atoms into the Ge substrate. As the growth temperature decreases, the formation of Ga vacancies also decreases and thereby reducing the Ge out diffusion. Additionally, the segregation of Ge atoms at the interface during the growth of the III-V nucleating layer is another important mechanism for Ge out-diffusion. Thus at low growth temperature, formation of gallium vacancies as well as the germanium segregation decreases. These two factors lead to a significant reduction of Ge out-diffusion. Consequently, the III-V layer grown at low temperature acts as a barrier layer for Ge out-diffusion. In the present case, since we are observing the disordered Ge near the GaP-Ge hetero-interface of nucleating layer grown at low temperature (~425°C), the possibility of Ge out-diffusion is debilitated. Therefore, the origin of phonon mode ~296 cm^{-1}, arising from disordered shallow layer of Ge near hetero-interface, cannot be attributed only to the Ge out-diffusion.

(2) **Fano effect due to doping**: It has been studied that doping of Si and Ge by '*n*' or '*p*' type dopants leads to the asymmetric broadening and red-shifting of optical

phonons (of host layer) due to coupling between discrete phonon and continuum of interband electron/hole excitations, termed as Fano interference [116-120]. Depending on the doping concentration, Fano line shape asymmetric broadening is wavelength dependent and becomes more pronounced at larger excitation wavelength [119, 121] for Ge. However, no such behaviour could be observed for the NL hetero-structure, when excitation wavelength is changed from 514.5 nm to 633 nm. Therefore, this possibility for origin of the broadening and softening of Ge-optical phonon of NL is also ruled out.

3) **Inter-diffusion of phosphorous across the hetero-interface:** As discussed above, Ge out-diffusion in GaP epilayer is ruled out as the cause for the origin of phonon mode ~296 cm^{-1}. In this scenario, other candidates considered for diffusion can be Ga and/or P. However, it has been reported that Ga diffusion coefficient in Ge is much less (more than an order) than that of P at similar temperatures [114]. Also, among the common group V dopants, phosphorous has highest solid solubility in germanium [122, 123], further favoring its diffusion. Therefore, inter-diffusion of substrate (Ge) and layer (phosphorous) elements at the hetero-interface is considered to be the most probable cause of disorder leading to the strained hetero-interface. It may be important to recall here that the introduction of dopants in semiconductors is performed widely by implantation technique. However, implantation depending on the dose may damage the material and may result in its partial/complete local amorphization/polycrystallization/nanocrystallization or increase in disorder [124-126]. The crystalline quality of the layer can be re-established by thermal treatment [127-129]. Similar effect is expected to occur for NL on thermal treatment. Prior to the growth of GaP on Ge (111), substrate is exposed to high phosphine (PH_3) flow (for 30 minutes) for creating the favorable phosphorous passivated Ge substrate.

During the epitaxial growth of nucleating layer, high V/III ratio of ~1725 is used. Under such growth condition, excess phosphorus can diffuse in Ge substrate due to its high solid solubility in Ge. Furthermore, it is reported that vacancy mediated diffusion (owing to smaller activation energy) is a dominant mechanism of phosphorous diffusion in Ge [130-132]. The enhanced diffusion is due to singly negatively charged donor-vacancy pair (AV^-) that mediates the donor (P) diffusion in Ge [132]:

$$AV^- <==> A_s^+ + V^{2-}$$

Where A_s^+ and V^{2-} are the singly positively charged substitutional donor with A(P) and doubly negatively charged vacancy (V^{2-}) respectively. The deactivation is related to the formation of inactive donor vacancy clusters, which is favored due to Coulomb attraction between As^+ and (AV^-) via the reaction:

$$AV^- \quad + \quad A_s^+ <==> (A_2V)^0$$

The formation of A_2V (P_2V) and even bigger clusters A_nV_m (P_nV_m) is consistent with the predictions of density functional theory calculations [132]. Such A_2V and A_nV_m clusters formation can lead to tensile strain in the host lattice. It can be recollected here that no change in Ge optical phonon is observed for GaP/Ge(111) TL grown at ~770°C. To mimic this growth, thermal treatment at ~700°C (close to thick layer growth temperature) is provided to NL, which leads to the improvement of the crystalline quality of NL. This occurs due to desorption of phosphorus, leading to annihilation of P_2V and higher order clusters, and thus results in the improvement of disordered Ge at the hetero-junction. It is known that at this temperature P out-diffusion will dominate over Ge [133, 134]. This is indeed observed as shown in Fig. 3.3.6(b), wherein the frequency and FWHM of Ge-optical phonon are restored to near wafer values. Further, no significant change in spectral features of Ge-optical phonon of TL could be observed on thermal treatment at ~700°C, which confirms that phosphorous out-diffusion from the substrate surface during the step-II of MOVPE growth is responsible for the improved Ge layer near hetero-interface. It must be mentioned here that, it is not only the thermal factor, which is responsible for the in-diffusion of phosphorous. The surface passivation of Ge (prior to growth) under high phosphine flow and high V/III flux ratio (~1725 for NL and only ~100 for TL) employed during the nucleating layer growth are also playing vital role in the diffusion of P in Ge, giving rise to disordered Ge layer near hetero-interface of NL. However, when thermal energy is introduced in the nucleating layer hetero-structure (either during the growth of TL at ~770°C or during the external thermal treatment like we have performed at ~500°C and ~700°C), the re-ordering of the affected (disordered) region take place following the structure of underlying (which acts as seed) crystalline layer. Therefore, experimental results confirm that the out-diffusion of P is the predominant cause for improving the crystalline quality of Ge at the interface. This is primarily because of the fact that during high temperature thermal treatment, there is no over-pressure of phosphorous, as it was in the case of nucleating layer growth. Furthermore, in the light of above discussion, the Gaussian lineshape of phonon mode ~296 cm^{-1} can be attributed to inhomogeneity of the hetero-interface due to inter-diffusion. Thus, all observed effects can be consistently explained in the terms of inter-diffusion of phosphorous near surface layers of Ge substrate during the low temperature epitaxial growth. It is noteworthy to mention that phosphorous incorporation in the substrate will certainly modify the surface energy of the non-polar substrate which should be beneficial for the growth of polar layer on non-polar substrate [80, 81].

Thus Raman spectroscopy, combined with AFM measurements on the same site, has revealed unique information on the interface of GaP/Ge(111); (i) the co-existence of WZ/ZB crystal phases and (ii) formation of shallow disordered Ge layer near the hetero-interface of nucleating layer hetero-structure. The study paves the way for probing the crystal phase coexistence and inter-diffused layer in the hetero-structures at sub-micron length scales, without requiring any specific sample preparation.

3.4 Conclusion

Combining Raman and AFM, we have investigated GaP/Ge(111) hetero-structures to understand effect of hetero-polarity, lattice mismatch, substrate passivation and growth kinetics on structural and physico-chemical properties of the GaP epilayer and substrate.

The variation in the peak intensity of additional feature ~358 cm^{-1} w.r.t. TO phonon are uniquely correlated with the topographical changes using Raman and AFM mapping on the same site, which facilitate stimulant for Raman spectroscopy from CSS. Crystal phase co-existence in GaP epilayer, with dominance of WZ phase GaP near the hetero-junction interface giving rise to phonon mode ~358 cm^{-1} and that of ZB phase near the surface, is established using spatially resolved polarization dependent Raman measurements from CSS of hetero-structure. The consistency between the spectral information obtained from growth and the CSS is brought out as a natural consequence. The results of this work provide the direct experimental evidence for the presence of WZ crystal phase at GaP/Ge(111) interface, using an optical technique that does not require any specific sample preparation. Therefore, the study provides a clear basis for future experimental investigation of interfacial polytypism in various advanced hetero-structures.

Furthermore, the mechanism responsible for anomalous red-shift and broadening of Ge-optical phonon of GaP/Ge(111) hetero-structure are delineated in the light of inter-diffusion of epilayer and substrate elements across the hetero-interface. The coexistence of the disordered inter-diffused Ge layer (~20 nm) below the GaP nucleating layer, resulting in softening and broadening of Ge-optical phonon, is ascertained from wavelength dependent Raman measurements and the recovery of affected region following the thermal treatment (~700°C) of NL hetero-structure. The qualitative and quantitative analysis of possible mechanisms show that the diffusion of P in Ge substrate, giving rise to the disordering of the shallow layer of Ge in NL hetero-structure, is jointly governed by kinetics, pre-growth passivation of substrate under high phosphine flux, and high V//III ratio. The results indicate that growth challenges associated with polar/non-polar epitaxy can be solved by diffusing the phosphorous in group IV substrates for the nucleating layer growth, and after desorption of P at high temperature; the actual growth structures can be formed.

Journal publications based on this chapter

(1) Raman spectroscopy and atomic force microscopy study of interfacial polytypism in GaP/Ge(111) hetero-structures, **R. Aggarwal**, A. A. Ingale and V. K. Dixit, *Appl. Surf. Sci.*, **2018**, 427, 754-762.

(2) Raman spectroscopy investigation of inter-diffusion in GaP/Ge(111) hetero-structures, **R. Aggarwal**, A. A. Ingale, V. K. Dixit, and V. Sathe, *Superlatt. Microstruct.*, **2019**, 125, 190-197.

Chapter 4: Structural properties of closely lattice-matched GaP/Si system and the impact of substrate orientation

4.1 Introduction and background

The investigations on epitaxially integrated polar/non-polar GaP/Ge(111) hetero-structures, having large lattice mismatch (~4%), were presented in the last chapter. Interfacial polytypism and atomic inter-diffusion near GaP-Ge hetero-interface are discovered to be the dominant effect in GaP epilayers grown on Ge(111) substrates. In the view of the results obtained for GaP/Ge(111), it becomes imperative to understand the structural attributes of GaP layer grown on closely lattice matched (~0.4%) and technologically important Si(111) substrate, wherein hetero-polarity is expected to play the primary role in determining the structural properties. Owing to small lattice-mismatch for GaP/Si, the epitaxially grown GaP layer is expected to have lower density of dislocations compared to GaP/Ge. Furthermore, for the same hetero-polar material combination GaP/Si, the effect of substrate orientation and hence the surface energy on nucleation during initial stages of growth, morphology, and evolution of ZB/WZ polytypes is ascertained through the investigation of GaP layer grown on another most widely used Si substrate orientation in microelectronic *i.e.*, (001). Accordingly, this chapter is structured into two parts. In first part, the surface and micro-structure variations in technologically important GaP/Si(111) hetero-structures are investigated using the spatially resolved polarized and wavelength dependent Raman measurements from growth and cross-sectional surface (CSS). The large variation in optical phonon frequencies of GaP (arising from

GaP/Si(111)) in spatially resolved Raman spectra from the growth surface is very intriguing. The spatially resolved Raman spectroscopy from the orthogonal surface (cross-sectional surface), as stimulated by AFM and wavelength dependent Raman measurements, identifies the strain distributed zinc-blende (ZB) GaP phases as well as the structural allotropes along the depth of GaP/Si(111) hetero-structure. In the second part, crystallographic morphed surface and hetero-interfaces of GaP/Si(001) hetero-structures are investigated, through unique implementation of combining the information on variation in spatially resolved polarization dependent Raman spectra and surface topography of grown layer. The mechanisms responsible for variation in ratio of Raman spectral weight of symmetry forbidden to allowed optical phonons of GaP are elucidated using azimuthal angle-dependent polarized Raman measurements by allowing for the contribution of energetically favorable higher-index {111}and{112} defect facets to light scattering. In the following section, we present the results obtained using Raman spectroscopy which provide insights into strain-gradients along the depth of GaP/Si(111) hetero-structure.

4.2 Strain variations along the depth of GaP/Si(111) hetero-structure: spatially resolved polarized and wavelength dependent Raman measurements

Representative Raman spectra (schematic: Fig. 4.2.1(a)) arising from (111) growth surface of GaP/Si(111) thick layer hetero-structure is shown in Fig. 4.2.1(b). Raman spectroscopy and AFM measurements are performed using SPM integrated Raman spectroscopy system (*Alpha 300S,* WiTec, Germany). Raman spectra are measured in backscattering geometry, using 514.5 nm (Ar ion laser) and 442 nm (He-Cd laser) laser excitations. The wavenumber per pixel coverage of Raman spectrograph is ~0.5 cm^{-1} at 514.5 nm. The laser focal spot size at the wavelengths of interest, using 100x objective (N.A. = 0.9), is ~0.6 μm.

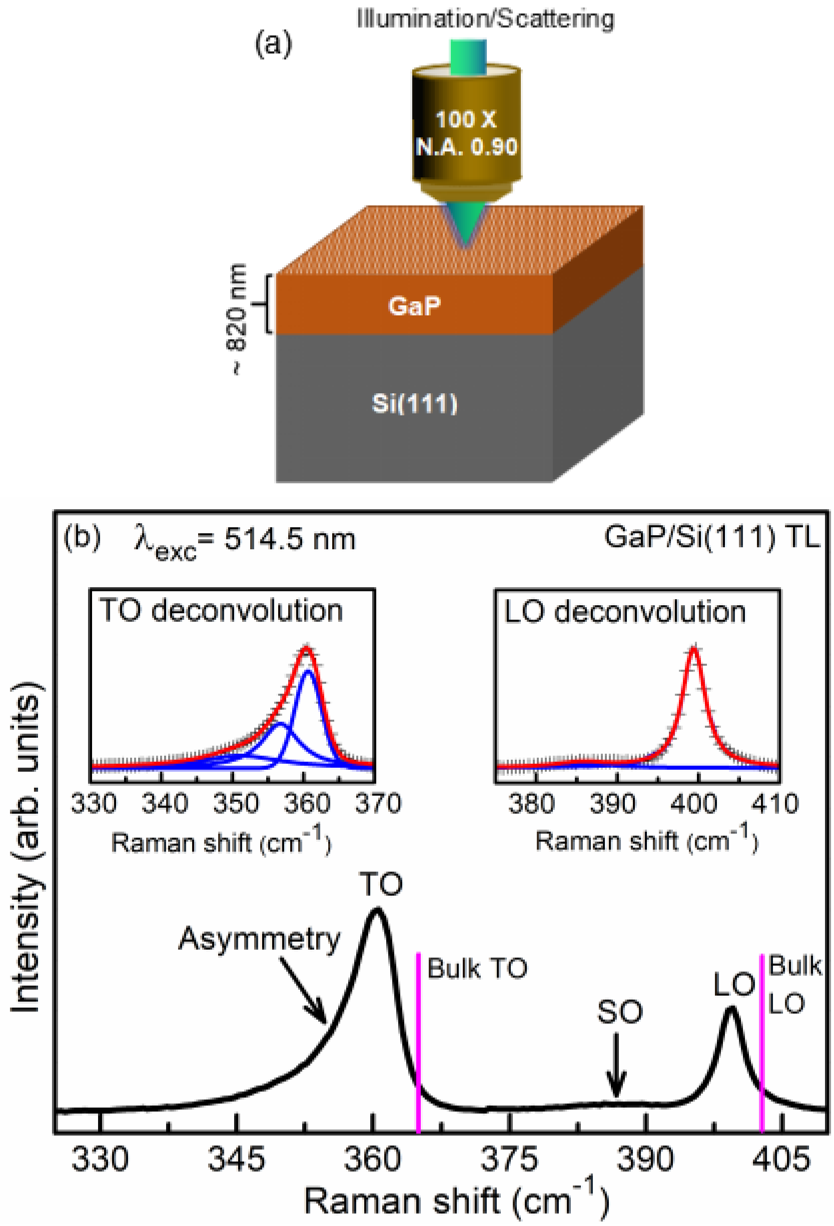

Fig. 4.2.1. *(a) Schematic for Raman back-scattering from growth surface (b) Raman spectra of GaP/Si(111) thick layer (TL) in back-scattering geometry. Inset shows deconvolution of various phonon contributions to TO and LO phonon bands, using minimum required Lorentzian and Gaussian lineshapes (blue). Red color line shows total fit to data (+).*

Laser power density at the sample surface is kept constant for all Raman spectra presented in this work with 514.5 nm and 442 laser excitations. Inset of Fig. 4.2.1(b) shows the deconvolution of the contributions of various modes to Raman spectra in the transverse optical (TO) and longitudinal optical (LO) phonon spectral range, separately. TO and LO phonons stemming from GaP layer are observed ~361 cm^{-1} and ~399 cm^{-1}, respectively. TO phonon spectral range has been fitted with three peaks (inset of Fig. 4.2.1(b)) *i.e.*, using minimum required Lorentzian/Gaussian line-shapes:

(i) The phonon mode ~350 cm^{-1} stems from the third order anharmonic interaction between TO and acoustic phonons, and it is observed even for bulk GaP [97, 98],

(ii) Phonon mode ~ 356 cm^{-1} may be related to E_{2H} phonon of the wurtzite (WZ) phase of GaP, as it was established for GaP/Ge(111) in chapter 3, and

(iii) Phonon mode ~361 cm^{-1} is attributed to TO phonon of GaP (Gaussian profile).

Similarly, the spectral range 375-410 cm^{-1} containing the LO phonon is de-convoluted using two phonon peaks:

(i) Broad phonon mode ~385 cm^{-1} is attributed to surface optical (SO) phonon of GaP [96], and

(ii) LO phonon of GaP ~399 cm^{-1}.

It is worth mentioning here that the contributions to phonon band in the spectral range 330-370 cm^{-1} (Fig. 4.2.1(b)) are first deconvoluted with only TO phonon, and the low frequency mode used to explain the asymmetry of the bulk GaP TO phonon [97, 98]. However, good fit could not be obtained with this. The fit is considerably improved, once the additional peak ~356 cm^{-1} is accounted for the observed (additional) asymmetry in the above spectral range. Based on our earlier understanding of GaP/Ge(111) hetero-structures, this phonon mode is expected to be the E_{2H} phonon arising from WZ phase GaP. The origin of additional modes and red-shift in optical phonon frequencies is discussed in the following.

4.2.1 Spatially resolved Raman spectroscopy from (111) growth surface

GaP is closely lattice-matched to Si and grown layer thickness (~820 nm) is beyond the critical thickness (~70 nm) for GaP/Si material combination. Despite this, it is observed that both TO and LO phonons are considerably red-shifted with respect to their bulk values (TO ~365 cm^{-1}, LO ~403 cm^{-1}).

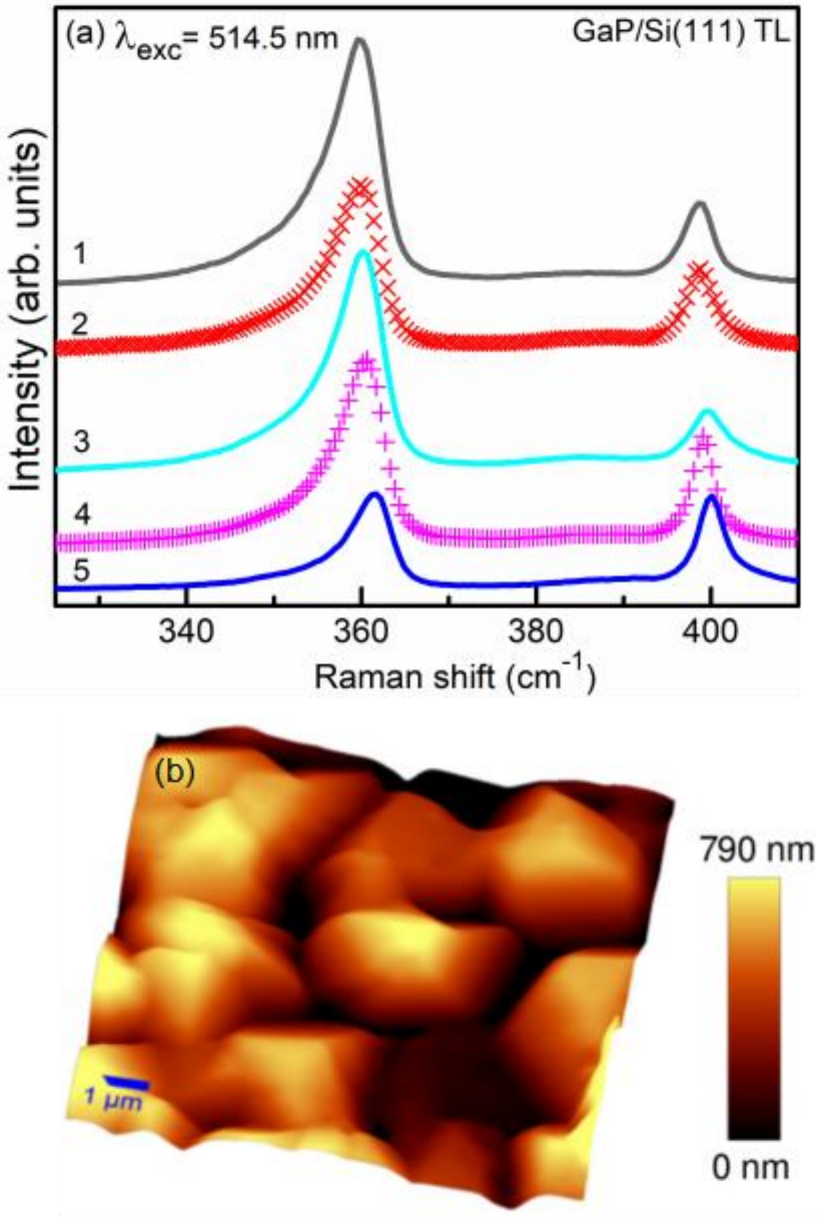

Fig. 4.2.2. (a) Raman Spectra recorded at randomly chosen five different spatial positions '1' to '5' across the GaP/Si(111) thick epilayer and (b) 3-D AFM scan of thick layer hetero-structure.

In order to understand the observed red-shift and examine its uniformity, spatially resolved Raman spectroscopy is performed on GaP/Si(111) TL hetero-structure from growth surface. Representative Raman spectra at five different (randomly chosen) spatial positions over the thick layer, exhibiting variation in optical phonon frequency and the peak intensity ratio of TO-to-LO phonons, are shown in Fig. 4.2.2(a). It can be further noticed that there exists variations in LO phonon line-shape and full width at half maximum (FWHM ~3-5 cm^{-1}). This indicates the spatial variations in strain and crystalline quality at different probed regions of the hetero-structure. The other two possibilities, generally considered as the cause of red-shift in phonon frequencies, are increase in temperature of the sample due to laser heating and the phonon confinement effect, both of which are not pertinent in the present case. Laser irradiation of GaP layer will not cause the heating and hence the phonon softening, as GaP ($E_{g(T)}$~ 2.78 eV) [86] does not have significant absorption at 514.5 nm ($E_{514.5\ nm}$= 2.41 eV) excitation. It may also be noted that for the laser power density (~300 kW/cm^2) employed in the present measurements, GaP wafer does not exhibit any red-shift in phonon frequencies. The effect of phonon confinement is also discarded as the GaP epilayer dimensions are much higher than 10 nm, below which confinement of phonons is expected.

Larger region of the sample is surveyed by spatially resolved Raman spectroscopy measurements, which confirm spatial variations in strain and crystalline quality across the thick GaP epilayer. Further, AFM map (Fig. 4.2.2(b)) of thick layer hetero-structure shows that GaP film growth occurs in form of micro-structures (size ~1 μm) having topographical variations in their height. Thus in order to identify, if this spatial non-uniformity is due to strain variation over lateral region or along the depth, wavelength dependent Raman spectroscopy is performed.

4.2.2 Wavelength dependent Raman measurements

The penetration depth of 514.5 nm laser, used for recording the Raman spectra in Fig. 4.2.1 and Fig. 4.2.2, is much larger than the GaP epilayer thickness. Therefore, using 514.5 nm laser excitation, the entire thickness (~820 nm) of GaP layer, and a limited depth of underlying Si(111) substrate is probed. Keeping this in mind, Raman spectroscopy from growth surface of GaP/Si(111) thick layer hetero-structure is performed in back-scattering geometry, using 442 nm excitation having penetration depth ~300 nm in GaP layer. The objective of employing 442 nm laser is to examine the difference (if any) in Raman spectra arising from GaP microstructures having topographical height smaller and larger than ~300 nm. Also, this may prompt whether the observed spatial non-uniformities in Raman spectra are correlated with variations along the depth of epilayer.

Indeed, mainly two different types of Raman spectra are observed (Fig. 4.2.3(a)): type 'A' from positions, where Si optical phonon (arising from underlying substrate) is also observed along with GaP optical phonons, and type 'B' from positions, which register only the GaP optical phonons in the Raman spectra. It can be seen from Fig. 4.2.3(a) that the optical phonons of GaP arising from type 'A' position, which also records the Si-optical phonon, are more red shifted (TO ~359.5 cm^{-1}, LO ~397 cm^{-1}) compared to that from type 'B' (TO ~362 cm^{-1}, LO ~400 cm^{-1}). Figure 4.2.3(b) shows the deconvolution of the spectral contributions (in Fig. 4.2.3(a)) to LO phonon envelope. It is also interesting to note that in type 'A' spectra, two LO phonon modes are observed at ~396 cm^{-1} and 400 cm^{-1}, whereas only single LO phonon mode ~400 cm^{-1} is observed in type 'B' Raman spectra. Also, the FWHM of all these three LO phonons are nearly similar.

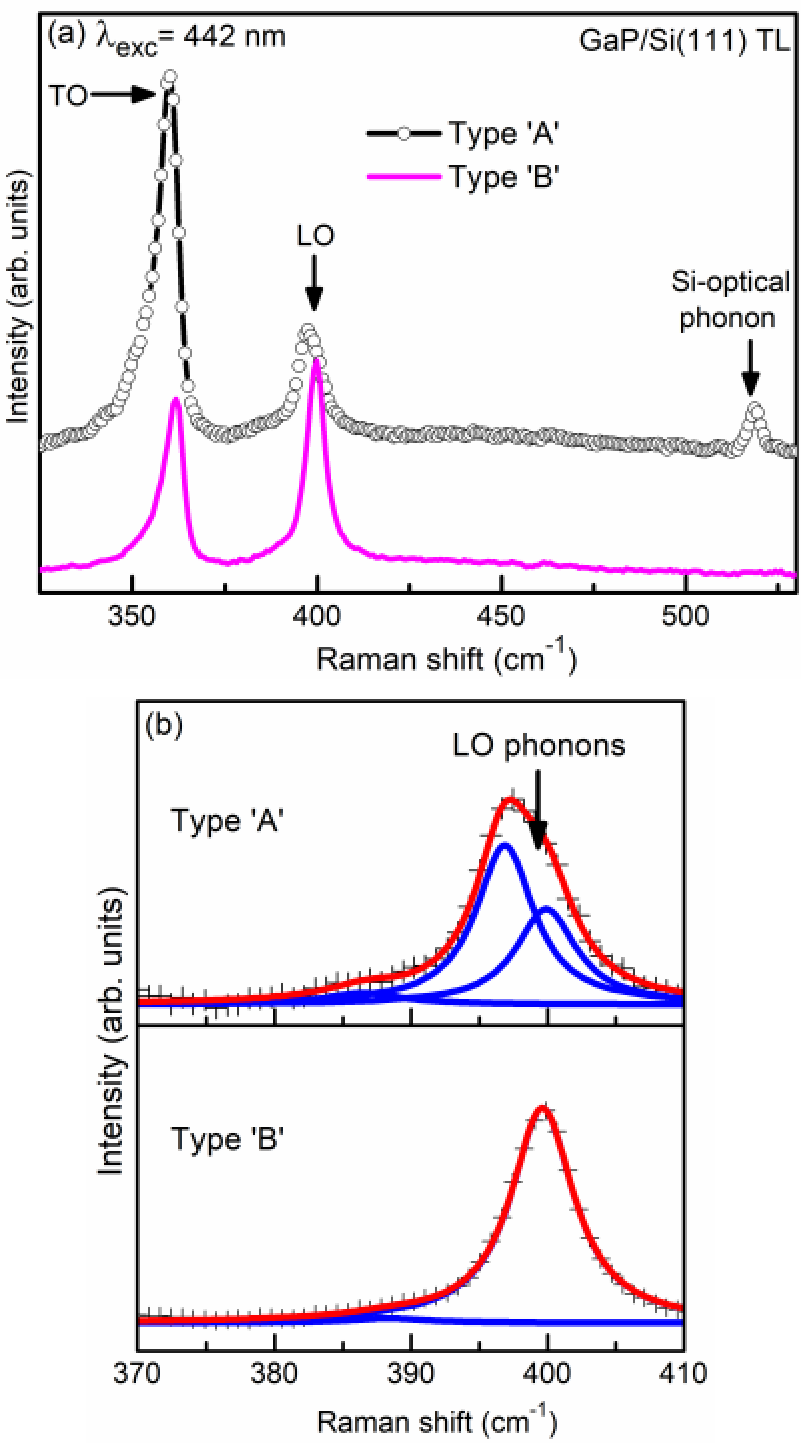

Fig. 4.2.3. *(a) Raman spectra arising from two types of regions over GaP/Si(111) thick layer, in back-scattering geometry (along growth axis), type A) having smaller thickness of GaP and type B) having larger thickness of GaP (b) deconvolution fit showing the doublet and singlet LO phonon features arising from type 'A' and 'B' regions, respectively.*

From the above discussion, it can be inferred that spectra of type 'A' arises from microstructures having thickness smaller than ~300 nm, whereas, type 'B' arises from thicker (>300 nm) microstructures. The different level of red-shift and other observed differences noted in these two types of spectra suggest the possibility of the presence of differently strained regions of GaP, along the depth. This is further investigated by spatially resolved Raman spectroscopy from the cross-sectional surface (CSS) *i.e.*, along the depth of the hetero-structure.

4.2.3 Spatial Raman sampling (~100 nm) across the cross-sectional surface: Strain distributed zinc-blende phases and allotropes

To substantiate the above interpretation, cleaved cross-sectional surface-interface of GaP/Si(111) hetero-structure is investigated by spatially resolved Raman spectroscopy, performed at a lateral step of ~100 nm (Fig. 4.2.4 (a) & (b)). Figure 4.2.4(b) shows Raman spectra observed at seven spatial positions across the cross-sectional surface (CSS), starting from near interface region to the GaP surface. It can be observed from Fig. 4.2.4(b) that at near interface position ‘1’, only one dominant phonon mode ~395 cm^{-1} is observed in the LO phonon spectral range. As the probe moves towards the surface (from position 1 to 7), another phonon mode ~399 cm^{-1} starts appearing and its peak intensity relative to ~395 cm^{-1} mode becomes nearly equal at intermediate (between surface and interface) spatial positions ‘4’ and ‘5’. Moving further to positions ‘6’ and ‘7’, the intensity of mode ~395 cm^{-1} diminishes, whereas the phonon mode ~399 cm^{-1} becomes dominant.

In this context, it will be useful to examine corresponding variation observed in TO phonon structure. For all the spectra presented, lowest frequency broad mode (~345-350 cm^{-1}) inherent to bulk GaP as noted earlier in relation to Fig. 4.2.1, will not be considered in the following discussion. For near interface position ‘1’, two modes ~353 cm^{-1} and ~358 cm^{-1} are observed in Raman spectra shown in Fig. 4.2.4(b). The phonon mode ~358 cm^{-1} is attributed to TO phonon stemming from strained (tensile) ZB phase GaP region of GaP microstructure near GaP-Si interface.

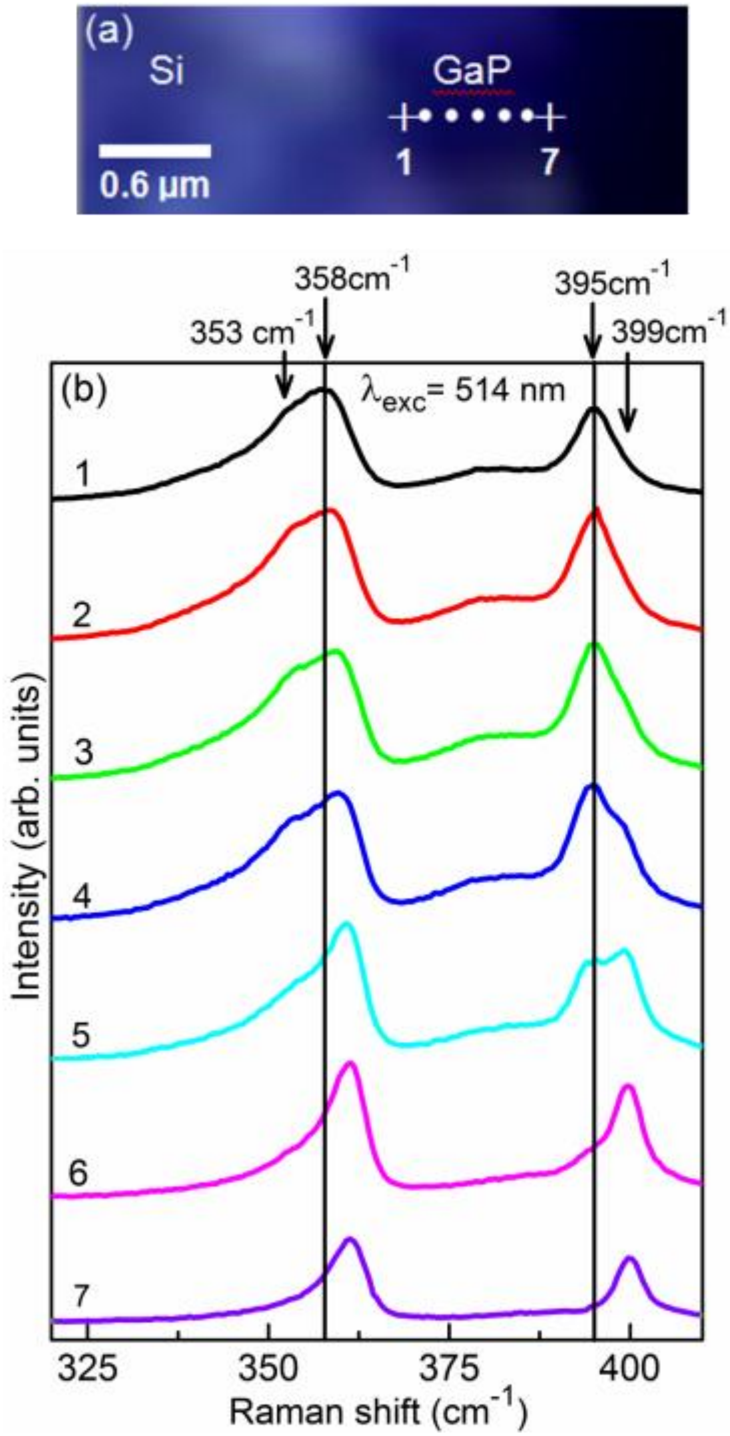

Fig. 4.2.4. *(a) Optical image of cross-sectional surface of GaP/Si(111) thick layer and (b) Raman spectra arising from seven spatial positions (marked in optical image (a)) across the cross-sectional surface.*

It can be noted from Fig. 4.2.4(b) that the line-shape of TO phonon structure in Raman spectrum arising from intermediate position '4' is markedly different to that from position '1'. Here, an additional phonon ~361 cm^{-1} is observed along with phonons ~353 cm^{-1} and ~358 cm^{-1}. Interestingly, at positions away from interface, phonon ~361 cm^{-1} starts appearing along with LO phonon ~399 cm^{-1}. This suggests that both these phonons ~361 and ~399 cm^{-1}, may have common origin. This is further confirmed from Raman spectra at spatial position '7' (Fig. 4.2.4 (b)), where only phonons ~361 cm^{-1} and ~399 cm^{-1} are dominant. Similarly, the dominance of phonons ~358 cm^{-1} and 395 cm^{-1} at near interface position '1', indicates that both these (TO, LO) phonons also have same origin.

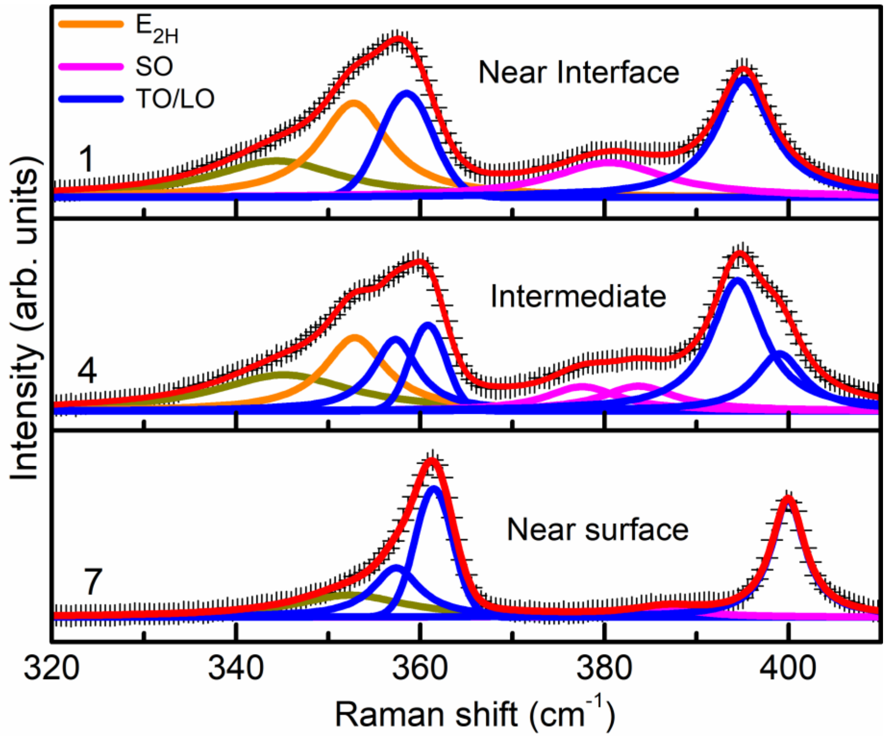

Fig. 4.2.5. *Deconvolution of contributions to Raman spectra in Fig. 4.2.4(b), recorded at positions '1', '4' and '7', using minimum number of Lorentzian and Gaussian line-shapes.* E_{2H}*, surface optical (SO) and TO/LO phonons contributions are shown in orange, magenta and blue colors, respectively. Red color curve is the total fit to data (+).*

Deconvolution in Fig. 4.2.5 shows the contributions of different phonon modes (of GaP) to Raman spectra (in Fig. 4.2.4(b)) arising from near interface region (position 1), intermediate region (position 4) and near surface region (position '7'). It can be deduced from Fig. 4.2.4(b) and Fig. 4.2.5 that Raman shift frequencies and line-shape of spectra stemming from these three positions are appreciably different from one another. Furthermore, the comparison of the red-shift (with respect to bulk GaP values) in frequencies of TO and LO phonons arising from positions ‘1’ and ‘4’ suggests that GaP layer near GaP-Si hetero-interface is more strained as compared to that near the GaP surface. Therefore, the phonon pairs ~358 & 395 cm^{-1} and ~361 & 399 cm^{-1} are attributed to TO & LO phonons stemming from ZB phases of GaP having different tensile strains, in accordance with its proximity to WZ phase along the depth of a micro-structure.

The co-existence of WZ and ZB crystalline phase in the grown structure *i.e.*, polytypism, generates strain in each crystal phase due to presence of the other phase. The different atomic arrangements at the boundaries between the ZB and WZ phases can have different chemical potential and free energy per atom in these systems. This leads to new minimum energy configuration (stable) unit cells, which germinate tensile strain in ZB and compressive strain in WZ phase of the material. Such variations in the ZB and WZ phases are more prominent in III-V nanowires, as reported by *Vandana et. al*, which may be referred to for further details of correlation between strain and polytypism [49]. In order to probe this possibility further, a crystal phase (ZB/WZ) quantum structures of GaP can be investigated, which is beyond the scope of the present work. Also, Raman spectra from position ‘7’ (near GaP surface) closely mimics the spectra from (111) surface of GaP/Si(111) hetero-structure. Although, LO phonon is symmetry forbidden in scattering from the cross-sectional surface *i.e.*, $(1\bar{1}0)$ plane, its appearance in the Raman spectra can be attributed to morphological variations in micro-structured GaP thick layer sample. The AFM map (Fig. 4.2.2(b)) of thick layer hetero-structure exhibits that the micro-structure edges have inclination with respect to surface normal, which may lead to observation of forbidden LO phonon. Consistently, the phonon mode ~353 cm^{-1}, prominent in near interface Raman spectra, is attributed to WZ phase (E_{2H} phonon) of GaP. To further understand this aspect of growth leading to formation of differently strained ZB phases, the nucleating layer is examined by Raman spectroscopy and AFM. The growth of nucleating layer significantly impacts the formation of thick GaP layers. Figure 4.2.6(a) and (b) show Raman spectra and AFM map of ~60 nm thick GaP/Si(111) nucleating layer hetero-structure.

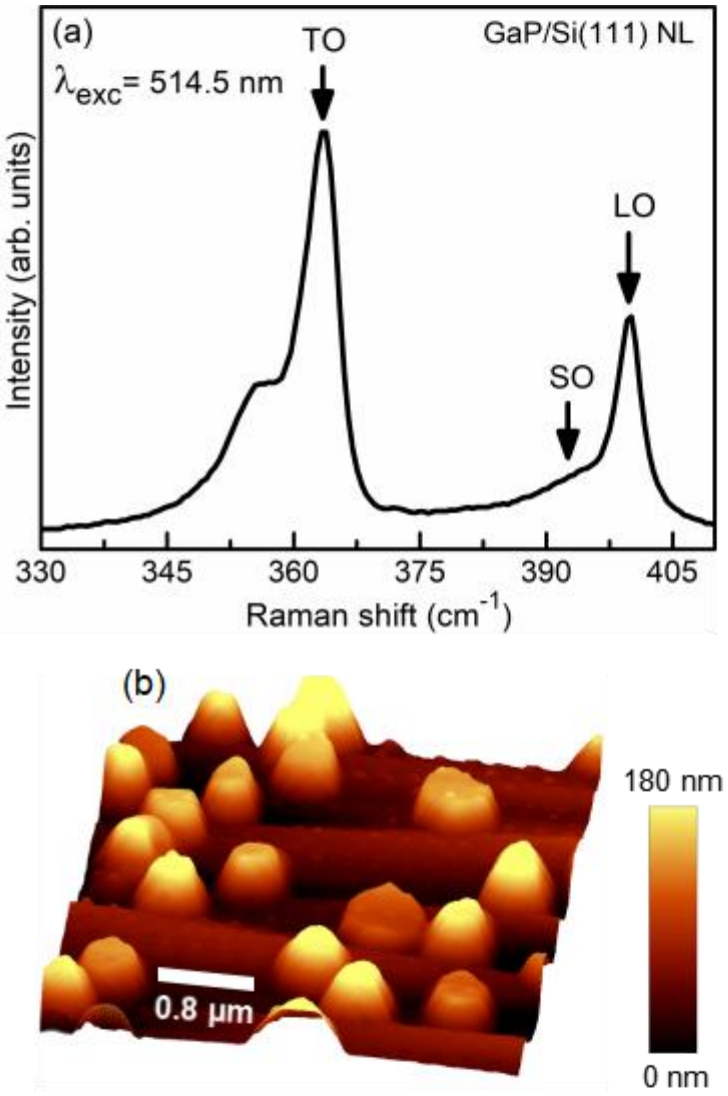

Fig. 4.2.6. (a) Raman spectra of GaP/Si(111) nucleating layer (NL), recorded from growth surface in back-scattering geometry (b) 3-D AFM map of nucleating layer hetero-structure.

AFM image (Fig. 4.2.6(b)) of the nucleating layer shows that the growth occurs in form of hexagonal and triangular shaped GaP micro-structures (size ~400-700 nm) having nearly flat morphology, and without inclination on the edges. Raman spectra show that both TO and LO phonons are red-shifted (by ~3 cm^{-1}) with respect to their observed bulk values. For GaP/Si combination, the GaP layer of thickness less than or close to critical thickness is expected to undergo compressive strain. Despite that GaP NL having layer thickness close to critical thickness is tensile strained, since TO and LO phonons of GaP NL are red-shifted. However, the red-shift in optical phonon frequencies of nucleating layer are smaller than those observed for thick layer hetero-structure. More importantly, the additional phonon signature ~355 cm^{-1} on low frequency side of TO phonon appear distinctively in Raman spectra of nucleating layer. Most of the region (>80%) of nucleating layer sample registers this kind of Raman spectra. Based on our discussion in chapter 3, the phonon mode ~355 cm^{-1} is attributed to the E_{2H} mode of the WZ phase GaP. In order to confirm the presence of WZ phase, polarization dependent Raman spectroscopy from CSS of thick epilayer (Fig. 4.2.7) is performed. The polarization configuration ($X(YY)\bar{X}$), which allows both E_{2H} (WZ) and TO (ZB/WZ) phonon shows red-shifted TO* phonon structure (combined peak) with respect to the other configuration ($X(ZZ)\bar{X}$), which allows only the TO phonon. Thus, TO* phonon structures under these two configurations differ from each other in spectral shift and line-shape, when both WZ and ZB phases are present. However, in case of only the ZB phase prevailing near the surface, same Raman spectra (lower spectra in Fig. 4.2.7) is observed in two polarization configurations.

The existence of WZ phase GaP is independently confirmed for nucleating layer hetero-structure, by generating the polar Raman plots for TO, LO phonon of ZB and

E_{2H} phonon in parallel polarization configurations. Polar Raman measurements are performed from growth surface of GaP/Si(111) nucleating layer in back-scattering geometry. The azimuthal dependence of the intensity of Raman phonon/s is measured in parallel configuration by rotating (by finite angles) the incident ($\boldsymbol{e}_i$) and scattered light ($\boldsymbol{e}_s$) polarizations in such a way that they remain parallel to each other.

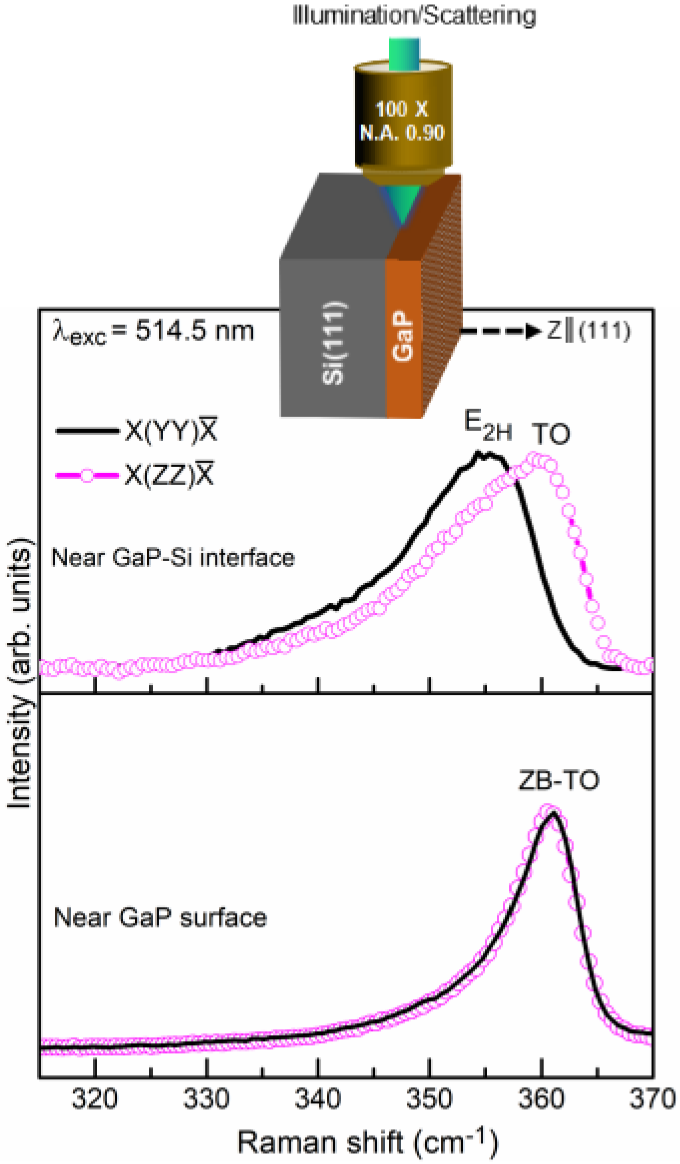

Fig. 4.2.7. *Polarization dependent Raman spectra (at 514.5 nm excitation) from near-interface and near-surface region of cross-sectional surface of GaP/Si(111) thick layer hetero-structure, under scattering configurations* $X(YY)\bar{X}$ *and* $X(ZZ)\bar{X}$.

The incident laser polarization is rotated by using a half wave plate and scattered light polarization is selected by rotating an analyzer in the output. Figure 4.2.8 shows polar plots of these phonons in parallel configuration, for back-scattering from (111) surface of nucleating layer.

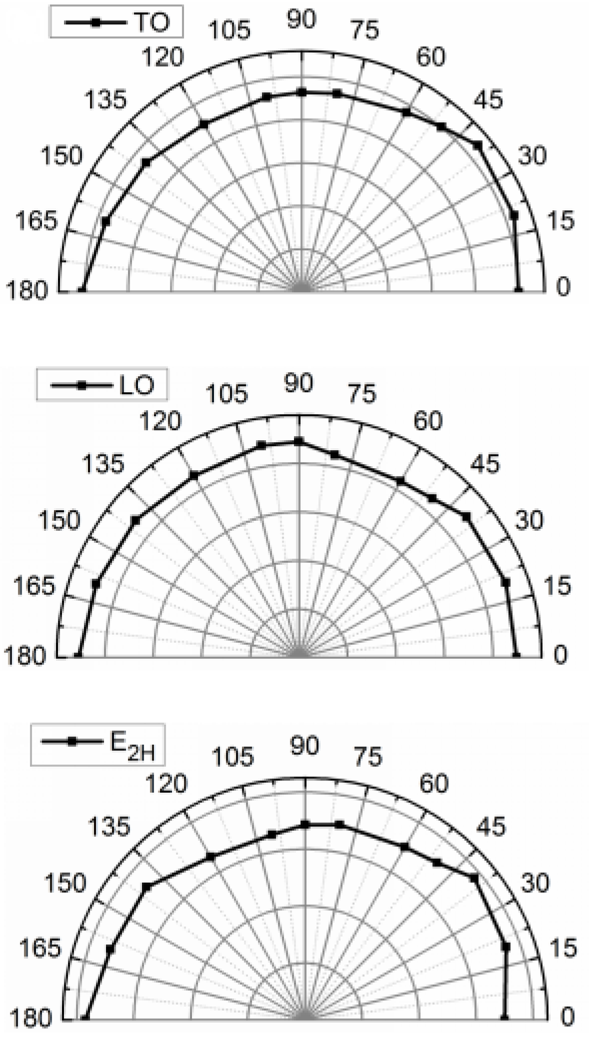

Fig. 4.2. 8. *Polar Raman plots of TO, LO and* E_{2H} *phonons of GaP/Si(111) nucleating layer in parallel polarization (* $\hat{e}_i \parallel \hat{e}_s$ *) configuration.*

Raman scattered intensity of TO and LO phonons are expected to have circular azimuthal dependence, and the observed polar plots are in accordance with it (Fig. 4.2.8). Furthermore, the observed Raman scattered peak intensity of phonon ~355 cm^{-1} *i.e.*, E_{2H}, is also independent of in-plane azimuthal rotation of incident and scattered light polarizations, as expected (Fig. 4.2.8) [135]. In the view of the understanding thus developed, we revisit and inspect the consistency between the spectral features arising from cross-sectional and growth surface, as discussed in next sub-section.

4.2.4 Correlation between Raman spectra from growth and cross-sectional surface

It is important to note that TO phonon ~358-362 cm^{-1} fits only with Gaussian for all Raman spectra arising from GaP/Si(111), and the same can be discerned from line-shape of raw spectra also. This is attributed to inhomogeneous distribution of defects seen in ZB structure due to presence of WZ phase. It is relevant to mention here that Raman spectra from bulk GaP wafer show a Lorentzian/Voigt line shape for TO phonon peak. With this understanding, we revisit the observed variations in Raman spectra in Fig. 4.2.2, which show that larger the red-shift in TO phonon structure, more are the peak intensity ratios of TO-to-LO and Si-to-TO phonons. This can now be corroborated with higher red-shift (as observed in Fig. 4.2.3) in the frequency of TO phonon arising from thinner region of GaP epilayer. Thus, there is larger contribution of E_{2H} phonon of WZ phase closer to interface and for the same reason; the spectra simultaneously show stronger Si phonon intensity due to higher laser power density reaching the underlying Si substrate. On the other hand, thicker region shows lesser contribution from WZ phase thus introducing small red-shift in frequency of ZB phonons and consequently the decreased Si phonon peak intensity. With reference to thick layer hetero-structure, the results obtained above can be schematically represented as shown in Fig. 4.2.9. Here, it may be pertinent to discuss the blue shift in frequency of surface optical phonon frequency from near GaP-Si interface to surface region (Fig. 4.2.4(b)). The intensity of surface optical mode increases with surface/volume ratio (i.e., surface roughness) and its frequency depends on the TO phonon frequency and dielectric constant of the surrounding medium [96]. Consistently, the surface optical phonon in the Raman spectra of near GaP-Si interface region is observed to be more red-shifted as compared to that arising from near surface region.

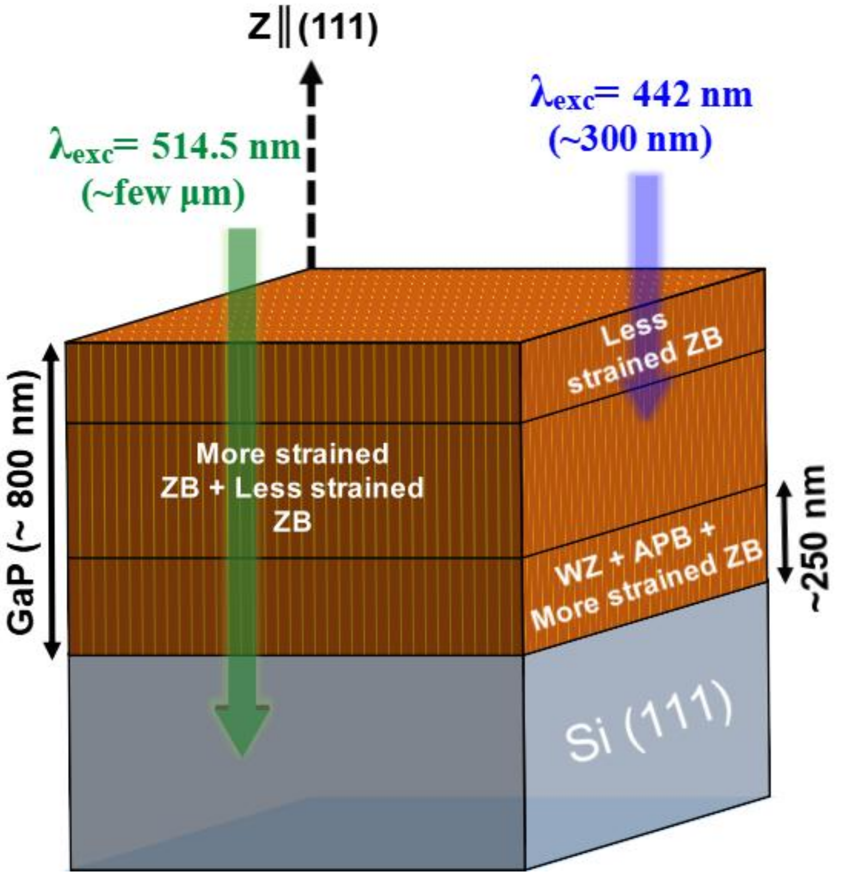

Fig. 4.2.9. *Schematic representation of results of this study, showing variations in strain/crystal structure along the depth of GaP/Si(111) TL hetero-structure.*

Thus, in-plane and cross-sectional Raman measurements along with AFM elucidate that the variations of spectral features along the depth of hetero-structure manifest itself in the spatial variation of the in-plane Raman spectra.

For the same hetero-polar GaP/Si material combination, a differently (other than (111)) oriented substrate is expected to play the role in nucleation during initial stages of growth, surface topology, and formation of ZB/WZ polytypes. Consequently, the investigations on the hetero-epitaxial integration of GaP on another most widely used Si substrate orientation in microelectronics *i.e.*, (001), are discussed in the second part of this chapter.

4.3 Interfacial nucleation of higher-index defect facets in GaP/Si(001) hetero-structures using polar Raman measurements

As discussed in chapter 1, the surface energy of the substrate is expected to impact the initial nucleation, surface morphology and crystalline properties of the overgrowth layer. Consequently, the influence of substrate crystallographic orientation and therefore the surface energy on the structural properties of grown layer is explored by investigating the epitaxy of GaP on extensively used (001) oriented Si substrate orientation *i.e.*, GaP/Si(001) hetero-structures. Polar Raman measurements on GaP/Si(001) hetero-structures reveal that interfacial nucleation and subsequent coalescence of faceted epiltaxial micro/nano-structures give rise to higher-index ({111} and {112}) defect facets in the overgrowth layer.

Figure 4.3.1 shows the unpolarized Raman spectra of nucleating layer (NL) and thick layer (TL) GaP/Si(001) hetero-structures, along with deconvolution fittings in the inset. Raman measurements are performed at 514.5 nm laser excitation using SPM integrated Raman system (*Alpha 300*, WiTec, Germany) and Trivista triple monochromator system *TR557* equipped with air cooled CCD detectors. The wavenumber per pixel coverage of Raman spectrograph is ~0.5 cm^{-1} at 514.5 nm. For the wavelengths of interest, the laser focal spot diameter using 50x objective (N.A.=0.75) is ~0.7 μm. Laser power density incident on the sample surface is kept constant (~300 kW/cm^2) for all the Raman measurements. According to Raman selection rules for a ZB crystal structure (discussed in chapter 2), TO phonon is symmetry forbidden for back-scattering from a (001) crystallographic plane. However, along with the symmetry allowed LO mode, the symmetry forbidden TO phonon with noticeable presence is also observed for both nucleating and thick GaP layers, as shown in Fig. 4.3.1.

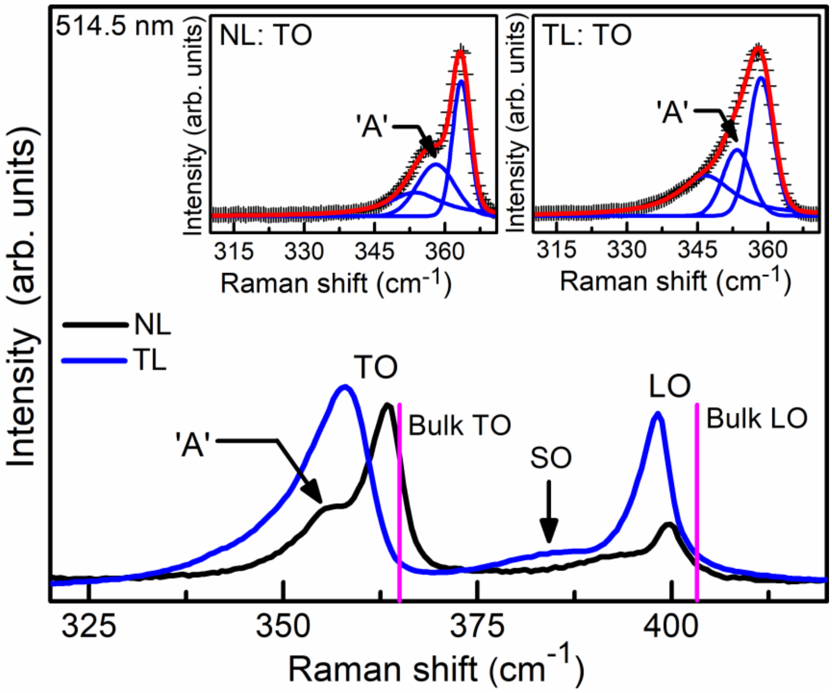

Fig. 4.3.1. *Unpolarized Raman spectra of nucleating (NL), and thick layer (TL) hetero-structures. Inset shows deconvolution of contribution to TO phonon spectral range using minimum number of Lorentzian and Gaussian line-shapes. Red color fit to data (+) shows the total fit.*

The frequencies of TO and LO phonons stemming from NL and TL are red-shifted with respect to GaP wafer (TO ~365 cm^{-1} and LO ~403 cm^{-1}). It should be pointed out here that the thickness of GaP nucleating layer is close to critical thickness and consequently, the grown layer is expected to be either relaxed or compressively strained. However, despite this a finite (~2 cm^{-1} for TO and ~3 cm^{-1} for LO phonon) red-shift (*w.r.t.* bulk GaP) is observed in frequencies of TO and LO phonon of GaP nucleating layer. The phonon mode ~385 cm^{-1} and ~392 cm^{-1} lying between TO and LO phonons of TL and NL samples respectively, are attributed to surface optical (SO) phonon arising from GaP layer [96]. In addition to TO and LO phonons of GaP, an asymmetric feature ~355 cm^{-1} (designated as mode ‘A’ in Fig. 4.3.1) on low frequency side of TO phonon is also observed, as discerned from the deconvolution shown in inset of Fig. 4.3.1. Before getting into the source of additional feature ‘A’, we focus our attention to the origin of symmetry forbidden TO phonon, having appreciably large scattering cross-section, and perform several micro Raman surveys (Raman mapping) on GaP/Si(001) TL.

4.3.1 Unpolarized and polarized Raman mapping of GaP/Si(001) thick layer hetero-structure

In order to understand the origin of the symmetry forbidden TO phonon having large scattering cross-section, several Raman mapping experiments are performed on thick layer hetero-structure. Owing to higher epilayer thickness of TL and hence the expected larger scattering cross-section of optical phonon/s arising from it, the TL hetero-structure is preferred for Raman spectral imaging. Raman map of a 10μm × 10μm region of GaP/Si(001) TL sample, obtained by integrating the intensity of optical phonons in spectral range 330-410 cm^{-1} (TO + LO phonon region), is shown in Fig. 4.3.2(a). Based on the spatial variation of spectral features as observed from Raman spectral image in Fig. 4.3.2(a), largely three different types of Raman spectra emerge, spectra having: 1) Peak intensity ratio of TO to LO phonons *i.e.*, $R = I_{TO}/I_{LO}<1$, 2) $R = I_{TO}/I_{LO} \sim 1$ and 3) $R = I_{TO}/I_{LO}>1$. The corresponding Raman spectra for such three spatial regions are shown in the Fig. 4.3.2(b). It is evident that for Raman back-scattering from growth surface, the contribution of allowed LO phonon relative to symmetry forbidden TO mode is dominant at spatial positions of type ‘1’. However, at spatial position of type ‘2’ and ‘3’ the peak intensity ratio ‘*R*’ are close to unity and greater than two, respectively. Such variations in the ratio ‘*R*’ cannot be explained by considering the scattering from (001) surface, alone.

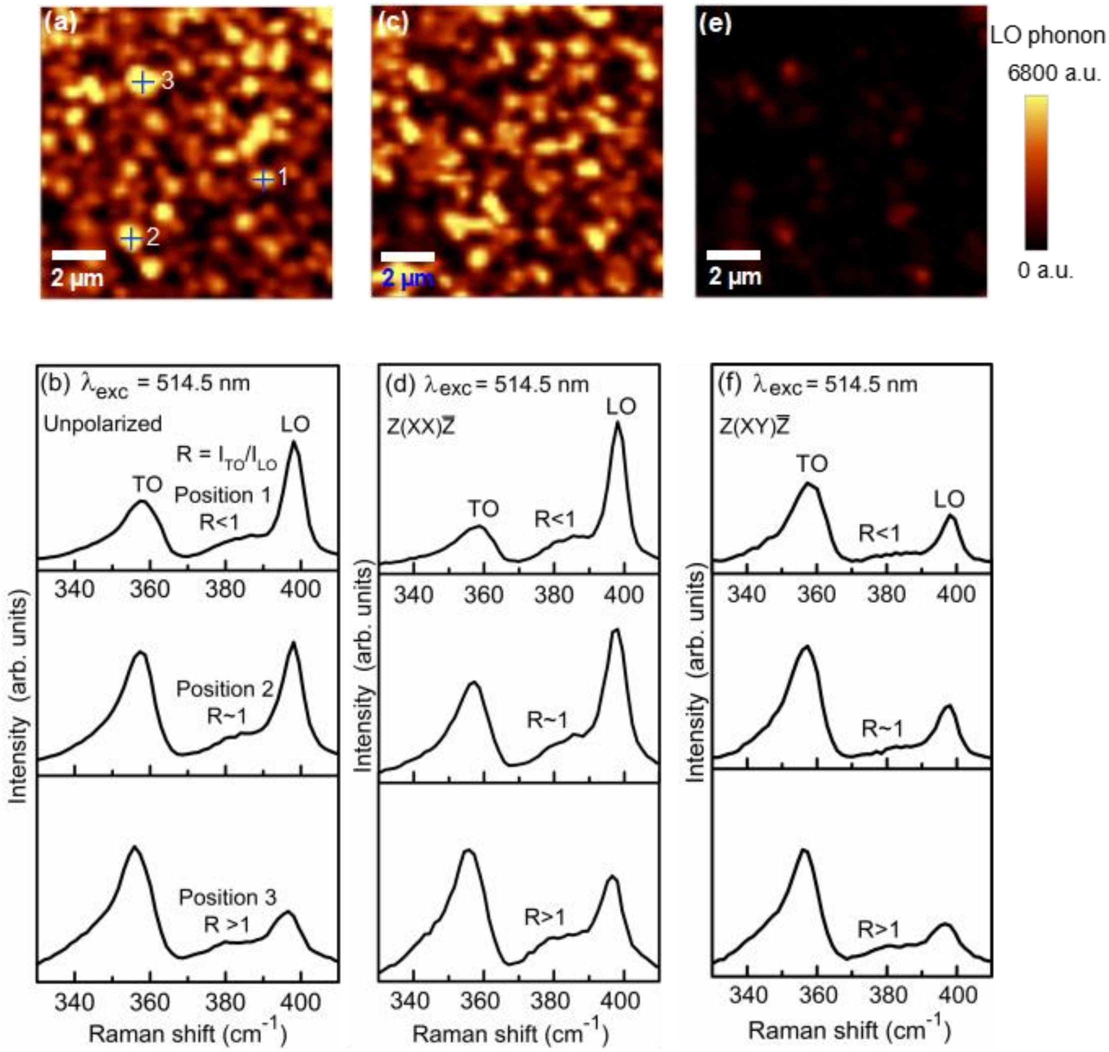

Fig. 4.3.2. *(a) Unpolarized Raman map of 10 μm×10 μm region of GaP/Si(001) thick layer, obtained by integrating over the spectral range: 330-410 cm*$^{-1}$*. (b) Raman spectra from three spatial positions types '1', '2' and '3' as denoted in (a). Polarization dependent Raman maps constructed by integrating the LO phonon along with spectra arising from the same spatial region and position types (as imaged in (a)) in (c, d) parallel (*$Z(XX)\bar{Z}$*) and (e, f) perpendicular (*$Z(XY)\bar{Z}$*) configurations. Polarized Raman maps in (c) and (e) are shown using the same scale for counts in arbitrary units (a.u.).*

Furthermore, to examine whether the LO phonon obeys Raman selection rules for back-scattering from (001) surface, polarized Raman mapping in parallel $Z(XX)\bar{Z}$ and cross $Z(XY)\bar{Z}$ configurations is performed (Fig. 4.3.2(c) and 4.3.2(e)) on the same region of TL. Polarized Raman maps for LO phonon in parallel (Fig. 4.3.2(c)) and cross (Fig. 4.3.2(e)) polarization configurations are obtained by integrating the Raman intensity in the spectral range 396-400 cm^{-1} (LO phonon range). Raman spectra in parallel and perpendicular (cross) polarization configurations, arising from spatial positions of types ‘1’, ‘2’ and ‘3’ (as marked in Fig 4.3.2 (a)), are shown in Fig. 4.3.2 (d) and 4.3.2(f) respectively, These spatial position types ‘1’, ‘2’ and ‘3’ in polarized Raman map exemplify the locations, where the peak intensity ratios ‘R’ are <1, ~1 and >1, respectively in the unpolarized image. We observe that for all three spatial position types (marked as‘1’ ‘2’ and ‘3’ in Fig. 4.3.2(a)), the peak intensity ratio $R = I_{TO}/I_{LO}$ changes from less than half or near unity in parallel configuration to greater than one in cross polarization configuration. As per Raman selection rules for ZB crystal, TO phonon is symmetry forbidden for back-scattering from (001) growth surface, irrespective of polarization configuration. Therefore, the variations in peak intensity of LO phonon are analyzed independently, in parallel and cross polarization configurations. It can be discerned that the peak intensity of LO phonon is high in parallel (Fig. 4.3.2 (c) and (d)) configuration $Z(XX)\overline{Z}$ and it gets reduced to nearly half or even less in cross (Fig 4.3.2 (e) and (f)) polarization configuration $Z(XY)\overline{Z}$ for all three spatial position types discussed above. This polarization dependent response of LO phonon (Table 2.1) indicates that one of the cleaved in-plane crystallographic orientation of grown epilayer is along $[1\overline{1}0]$(or an equivalent direction) or at some very small angle to this direction. It should be mentioned here that all the unpolarized and polarized Raman measurements in Fig. 4.3.2 above have been performed by positioning the GaP/Si(001) hetero-structure with its cleaved in-plane direction along the one of the lab coordinate axes. It is also known that (001) oriented plane of ZB type crystal requires minimum energy for cleavage along $[1\overline{1}0]$ or an equivalent crystallographic direction. Therefore, considering the crystallographic basis [X ≡ $[1\overline{1}0]$, Y ≡ [110] and Z ≡ (001)], the polarization dependent Raman spectral mapping in parallel and cross configurations confirm that allowed LO phonon nearly follows the Raman selection rules for back scattering from (001) surface for a ZB crystal structure. In both parallel and cross polarization configurations measurements, the laser power density on sample surface is kept same. It is important to note here that peak intensity of TO phonon remains nearly the same (within ±5%) in both parallel and cross polarization configurations at all the three types of spatial positions. Insensitivity of TO phonon peak intensity to polarization configurations suggests that it may be disorder activated zone edge (DAZE) phonon, feasibility of which is discussed in the following sub-section.

4.3.2 Disorder activated zone edge phonon

It is worth mentioning here that in the only other existing (to the best of our knowledge) report on Raman spectroscopy of GaP/Si(001), the forbidden TO phonon arising from molecular beam epitaxy (MBE) grown GaP/Si(001) hetero-structures has been observed [136]. They have attributed this to disorder activated zone edge TO phonon arising due to breakdown of wave-vector selection rules [136]. Taking this into consideration, the possibility of this phonon being a disorder activated zone edge (DAZE) is analyzed. The DAZE phonon may appear due to activation of $|\boldsymbol{q}| \neq 0$ phonons as a consequence of the presence of disorders in grown layer and large density of phonons at the Brillouin zone edge. In view of the Raman data discussed above, the possibility of TO phonon being DAZE mode is vitiated because; (1) for bulk GaP, the zone-edge phonon frequency is ~355-359 cm^{-1} [137] and for a strained (tensile) GaP thick layer, corresponding bulk DAZE frequency should be red-shifted. Furthermore, it is worth noticing that forbidden TO phonon arising from nucleating layer hetero-structure is observed ~363 cm^{-1} *i.e.*, close to the zone center TO phonon frequency of bulk GaP, and (2) the crystalline quality of GaP film (for NL and TL:

$\mathrm{FWHM_{LO}}$ ~4 cm^{-1}) is nearly same as that of doped GaP wafer. Also, the possibility of disorder activated mode appearing with larger scattering cross-section than allowed LO mode is remote, even for the highly disordered film, which is certainly not the case here. Therefore, the feasibility of forbidden TO mode being DAZE phonon to the extent that its spectral weight exceeds that of allowed LO phonons is discarded. This led us to consider another plausibility of TO mode being allowed owing to morphological variations in micro-structured GaP epilayer grown on Si(001), as observed in optical image of TL hetero-structure while performing the Raman mapping. Therefore, the topographical contributions to the Raman scattering cross-section of the observed TO phonon are analyzed in the following sub-section**.**

4.3.3 Morphological variations in the GaP/Si(001) hetero-structures

The topological variations in the epilayer can give rise to allowed scattering contribution from the inclined surfaces, and hence one may observe the large scattering cross-section of the apparently forbidden TO phonon, which actually is the allowed contribution for those facets. This aspect of surface morphology variations is investigated by performing the AFM mapping of both NL and TL hetero-structures. The AFM maps of NL and TL (Fig. 4.3.3(a) and (b)) exhibit that the nucleating and thick epilayers consist of micro/nano-structures (island shaped) having sizes in the range 300-1000 nm. From AFM scans in Fig. 4.3.3, the average roughness of nucleating and thick layer hetero-structures are ~25 nm and ~85 nm respectively. Also, the roughness of individual micro-structures (of TL) *i.e.*, the regions having similar spatial dimension as the Raman probe, is even less and lies in the range 15-35 nm. Most of the micro/nano-structures in NL are elongated triangular (pyramidal) shaped islands with side wall having finite inclination with respect to the surface normal. Interestingly, the formation of islands (width ~300-500 nm, length ~600-900 nm) elongated along a particular [*hkl*] direction is the typical feature of GaP nucleating layer, as seen in Fig. 4.3.3(a). However, the TL (Fig. 4.3.3(b)) consists of triangular, hexagonal and irregular shaped micro-structures having nearly flat morphology.

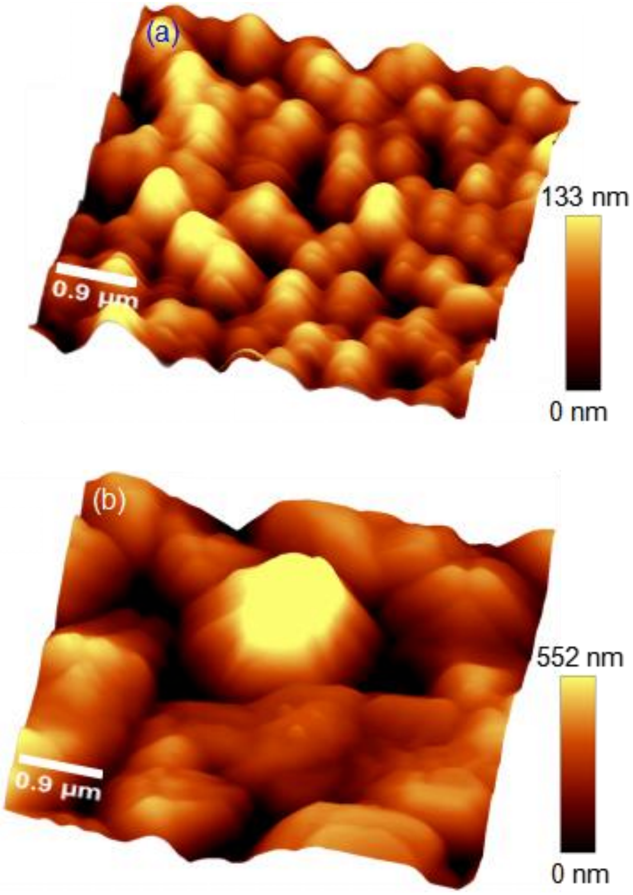

Fig. 4.3.3. *AFM scan of (a) nucleating layer and (b) thick layer hetero-structures showing the surface morphology.*

In the nucleating layer, observation of TO phonon due to scattering from side edges of the nanosized islands may be a possibility. However, the TL consisting mostly of micro-structures that have nearly flat topography, also exhibits the dominance of spectral weight of forbidden TO over that of LO phonon. Such mutual exclusiveness impelled us to contemplate the scattering contributions from crystallographic facets other than (001), wherein TO phonon is symmetry allowed even in apparent absence of facets. This is explored further by angle-resolved polarized Raman measurements from growth surface of thick layer (in back-scattering geometry), for ascertaining the various allowed scattering contributions.

4.3.4 Polar dependence of Raman spectra from GaP/Si(001)

Scattering contribution of non-(001) facets is investigated by obtaining the polar Raman plots *i.e.*, measuring the dependence of the TO and LO phonons intensity on the azimuthal rotation of incident and scattered light polarizations. Figure 4.3.4(a) shows the schematic of the Raman back-scattering configuration employed for obtaining the polar Raman dependence of GaP optical phonons. For this, polar dependence of optical phonons of TL hetero-structure is measured in parallel $(e||e_s)$ and cross $(e_i \perp e_s)$ polarization configurations.

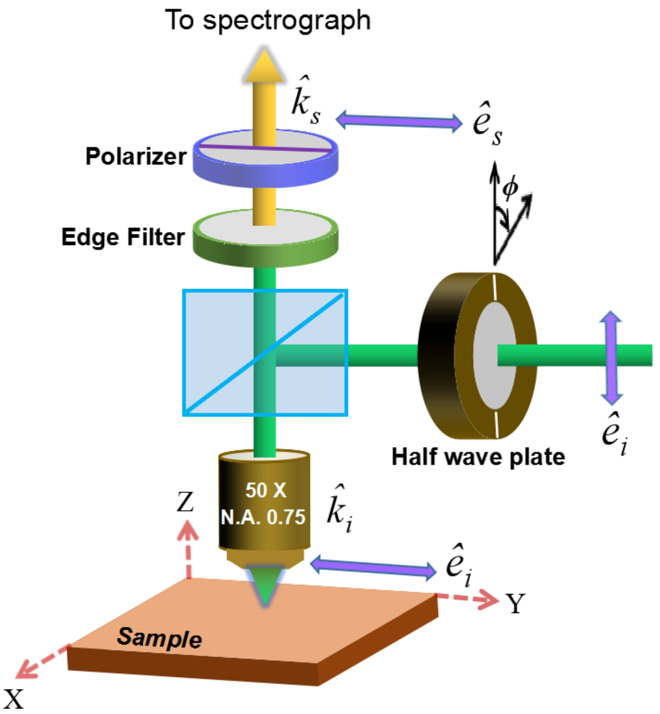

Fig. 4.3.4. *Typical schematic diagram of Raman back-scattering configuration utilized for determining the azimuthal angle dependence of intensity of optical phonons scattered from a given crystal orientation.* $(\mathbf{e}_i, \mathbf{k}_i)$ *and* $(\mathbf{e}_s, \mathbf{k}_s)$ *are the incident and scattered light polarization and propagation wave vectors respectively.*

In order to assess the shape of observed polar Raman plots for certain polarization configuration, the general expression determining the theoretical polar dependence of intensity of optical phonons from given (*hkl*) crystal orientation, is calculated using the following expression:

$$I_s = \left|\hat{e}_i .\ R.\ \hat{e}_s\right|^2 \tag{4.1}$$

where, $\boldsymbol{e}_i$ and $\boldsymbol{e}_s$ are the polarization directions of incident and scattered radiations, respectively, and '*R*' is the second rank Raman tensor, whose elements depend on crystal symmetry. For a ZB crystal having T_d symmetry, Raman tensors along the main crystallographic basis (x ≡ [100], y ≡ [010] and z ≡ [001]) can be expressed as [87]:

$$R(x) = \begin{pmatrix} 0 & 0 & 0 \\ 0 & 0 & d \\ 0 & d & 0 \end{pmatrix} \quad R(y) = \begin{pmatrix} 0 & 0 & d \\ 0 & 0 & 0 \\ d & 0 & 0 \end{pmatrix} \quad R(z) = \begin{pmatrix} 0 & d & 0 \\ d & 0 & 0 \\ 0 & 0 & 0 \end{pmatrix} \tag{4.2}$$

Raman tensors for a given coordinate axes system *e.g.*, X = $[1\bar{1}0]$, Y = [110] and Z= [001] can be obtained by transforming (Appendix-B) the basis from main crystallographic axes to experimental coordinate system. In laboratory coordinate system, the incident and scattered light polarization vectors can be expressed as:

$$\hat{e}_i = \hat{e}_s = \begin{pmatrix} \sin\phi \\ \cos\phi \\ 0 \end{pmatrix} \ \hat{e}_i \parallel \hat{e}_s \quad and \quad \hat{e}_i = \begin{pmatrix} \sin\phi \\ \cos\phi \\ 0 \end{pmatrix} \ \hat{e}_s = \begin{pmatrix} \cos\phi \\ -\sin\phi \\ 0 \end{pmatrix} \ \hat{e}_i \perp \hat{e}_s \tag{4.3}$$

where, azimuth angle ϕ is measured with respect to the 'Y' axes. The angle ϕ is changed by rotating the half wave plate as shown in Fig. 4.3.4 (a). From equations (4.1), (4.2) and (4.3), the azimuthal angle dependence of Raman intensity of optical phonons under back-scattering from given [*hkl*] crystal orientation can be written as:

$$I_{LO,TO} \propto \left|R_{XX}\sin^2\phi + R_{XY}\sin(2\phi) + R_{YY}\cos^2\phi\right|^2 \quad \hat{e}_i \parallel \hat{e}_s \tag{4.4}$$

$$I_{LO,TO} \propto \left| \frac{1}{2} R_{XX} \sin(2\phi) + R_{XY} \cos(2\phi) - \frac{1}{2} R_{YY} \sin(2\phi) \right|^2 \quad \hat{e}_i \perp \hat{e}_s \qquad (4.5)$$

where, 'R_{IJ}' are the IJ^{th} elements of Raman tensors calculated for laboratory coordinate system. For a given crystal orientation (*hkl*), the complete polar dependence of the scattering cross-section of TO and LO phonons (under back-scattering geometry) in parallel and cross polarization configurations can be determined using the above equations (4.4) and (4.5). The polar Raman plots presented in this study are obtained by plotting the peak intensity of optical phonons against the azimuthal-angle ϕ. For further verification, the polar dependence (in some of the cases) is also inspected by depicting the deconvoluted oscillator strengths of Raman phonons against the azimuthal-angle. The polar patterns so obtained closely resemble the peak-intensity versus ϕ plots. Taking into consideration the sources of error in peak intensity, the experimental plots are accurate within ~5%. Also, the role of numerical aperture (NA=0.75) in obeyance of Raman selection rules is ascertained, as the peak intensity ratio I_{TO}/I_{LO} observed for bulk GaP(001) wafer is significantly smaller (<0.015) than that for GaP/Si(001) hetero-structures. As specified above, the roughness of the spatial region, probed by Raman spectroscopy, is more than an order of magnitude smaller than the wavelength of incident excitation. This validates the far-field treatment of electric field and hence the Raman tensors, as presented in this study.

Polar Raman plots of LO phonon of TL hetero-structure in parallel polarization configuration measured at the spatial positions of type '1' and type '2' & '3',where the ratio $R= I_{TO}/I_{LO}$ is less than unity or near unity (in unpolarized data of Fig. 4.3.2(b)), are shown in Fig. 4.3.5(a) and 4.3.5(b) respectively. Azimuthal dependence of optical phonons arising from spatial positions of type '2' & '3' are closely similar and therefore, for the sake of brevity, hereinafter they have not been shown separately.

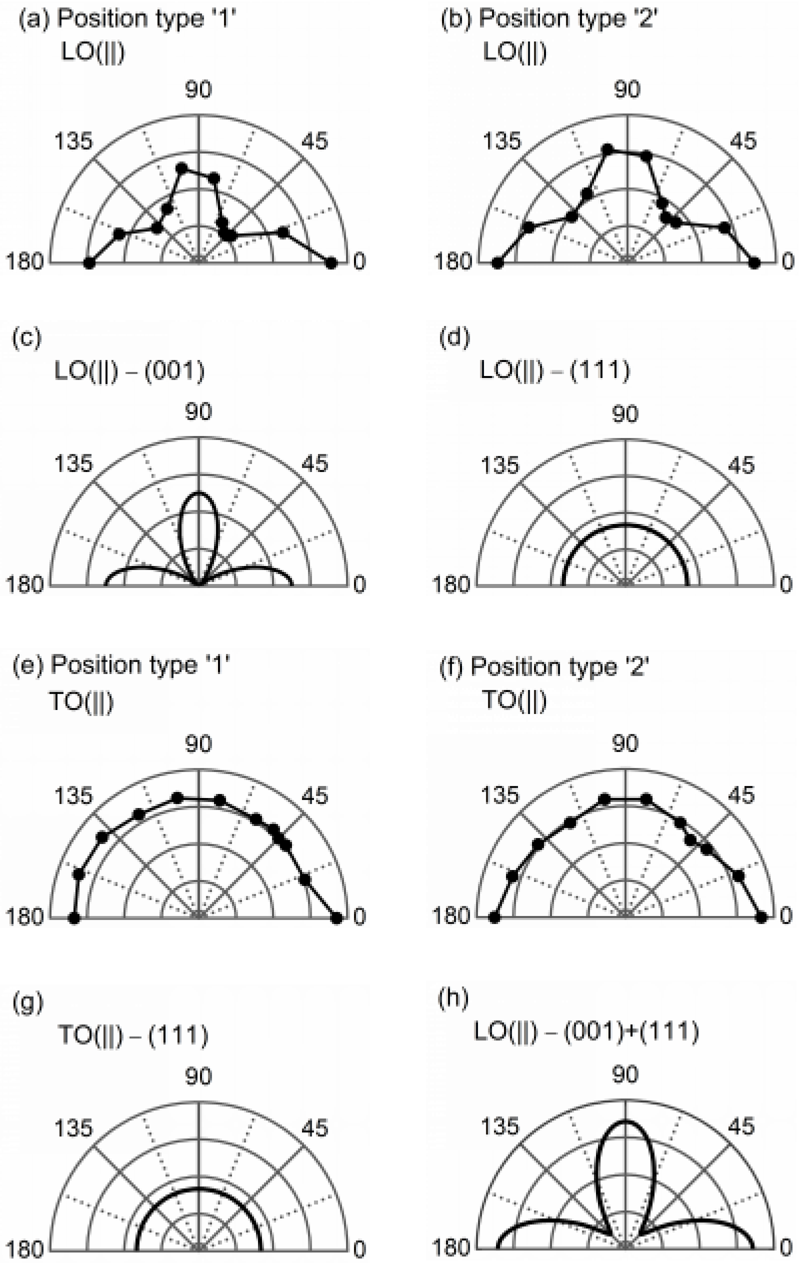

Fig. 4.3.5. *Observed polar dependence of LO phonon of GaP/Si(001) thick layer in parallel* $(\mathbf{e}_i||\mathbf{e}_s)$ *polarization configuration, arising from spatial position of (a) type '1' (where peak intensity ratio* $R = I_{TO}/I_{LO}$ *is less than unity in Fig. 4.3.2(a) and (b)), and (b) type '2' (where the ratio R~1 in Fig. 4.3.2(a) and (b)) Calculated azimuthal angle-dependence of LO phonon intensity for scattering from (c) (001) and (d) (111) planes. Observed polar plots of TO phonon of thick layer in parallel configuration at position of (e) type '1' and (f) type '2'. Calculated polar pattern of TO phonon for scattering from (g) (111) facets and (h) combination of (001) and (111) facets.*

In parallel polarization configuration, polar Raman plots of allowed LO phonon closely resemble the theoretically calculated (Fig. 4.3.5(c)) azimuthal variation for back-scattering from (001) surface. However, the deviation we observe (in configuration $e_i||e_s$) from calculated plot is that the LO phonon scattering cross-section does not vanish for angle ϕ = 45° (here 'ϕ' is measured w.r.t. to coordinate axis 'Y') as predicted from Fig. 4.3.5(c). This is consistent with polarization dependent Raman spectral mapping in Fig. 4.3.2 and suggests that there may be scattering contribution from different crystallographic facets of the ZB crystal structure, having circular shaped polar Raman plots. The AFM scan (Fig. 4.3.3(a)) of nucleating layer hetero-structure shows that the most probable crystallographic facets are {111}. Therefore, there is strong possibility that epitaxial micro-structures, particularly in GaP nucleating layer during the initial nucleation, are faceting to lowest energy crystallographic facets, and for a ZB crystal structure these are expected to be closed pack {111} crystallographic planes. Using equation (4.4), the Raman intensity of TO and LO phonons for scattering from (111) plane (in parallel configuration) is calculated and is found to be invariant to change in angle *'ϕ' i.e.*, it exhibits a circular polar Raman plot as shown in Fig. 4.3.5(d). Also, we have already shown in section 4.2 that the Raman scattering cross-section of the optical phonons of GaP/Si(111) nucleating layer features circular azimuthal dependence. For GaP/Si(001) TL, this attribution is further confirmed by measuring and analyzing the polar Raman plots of TO phonon arising from position types '1' (Fig. 4.3.5(e)) and '2' (Fig. 4.3.5(f)), in parallel configuration. At spatial position type '1', the peak intensity of TO phonon exhibits circular azimuthal-angle dependence, as shown in Fig. 4.3.5(e). However, slight deviation from circular polar Raman plot is observed at spatial position type '2' (Fig. 4.3.5(f). Further, it should be noted that calculated polar Raman plot of TO phonon (Fig. 4.3.5(g)) scattered from (111) surface is also circularly symmetric, as discussed above.

Taking into account the intensity contribution from (111) facet, the simulated combined polar Raman plot of LO phonon in parallel configuration is shown in Fig. 4.3.5(h), which has non-vanishing intensity at 45° and 135° like the observed azimuthal dependence in Fig. 4.3.5(a). The simulated polar pattern in Fig. 4.3.5(h) is obtained by adding the contribution of (001) and {111} facets in ratio of 70%-to-30%. Nevertheless, the azimuthal dependence does not match exactly with the observed (Fig. 4.3.5(a)) pattern. From further calculations, the better match with the observed (Fig. 4.3.5(a)) variation is obtained for ~50% contribution of {111} facets, which seems impractical to some extent. The possible causes of this discrepancy will become apparent as the presence of stacking faults is revealed, in the later part of this discussion. Concerning the spatial position type ‘2’, polar Raman plot of TO phonon (Fig. 4.3.5(f)) shows slight deviation from circular symmetry. This is explored into further by inspecting the azimuthal angle-dependent variation of TO phonon intensity in cross polarization configuration, which is also expected to have circular symmetry like parallel (Fig. 4.3.5(g)) configuration. Figure 4.3.6(a) and (b) show the observed polar Raman dependence of the peak intensity of TO phonon (in cross polarization configuration) arising from positions of type ‘1’ and ‘2’, respectively. It is worth emphasizing here that at spatial position type ‘2’ (& ‘3’), where the peak intensity ratio $R= I_{TO}/I_{LO}$ is near or greater than unity (in unpolarized Raman data in Fig. 4.3.2(b)), polar Raman plot of TO phonon shows noticeable deviations from circular pattern. This suggests that there might be the contribution of additional crystal facet/s at spatial positions types ‘2’ & ‘3’.The evidences for the formation of higher-index {111} facets in epitaxially grown layers on (001) substrate are searched for, and it is found that they exist in literature [84, 138]. *Villa and Naryanan et. al.,* have reported the formation of higher-index {112} and {113} faceted islands in chemical beam epitaxy grown GaAs and GaP epilayers on Si(001), using high resolution transmission electron microscopy (HRTEM) [84, 138].

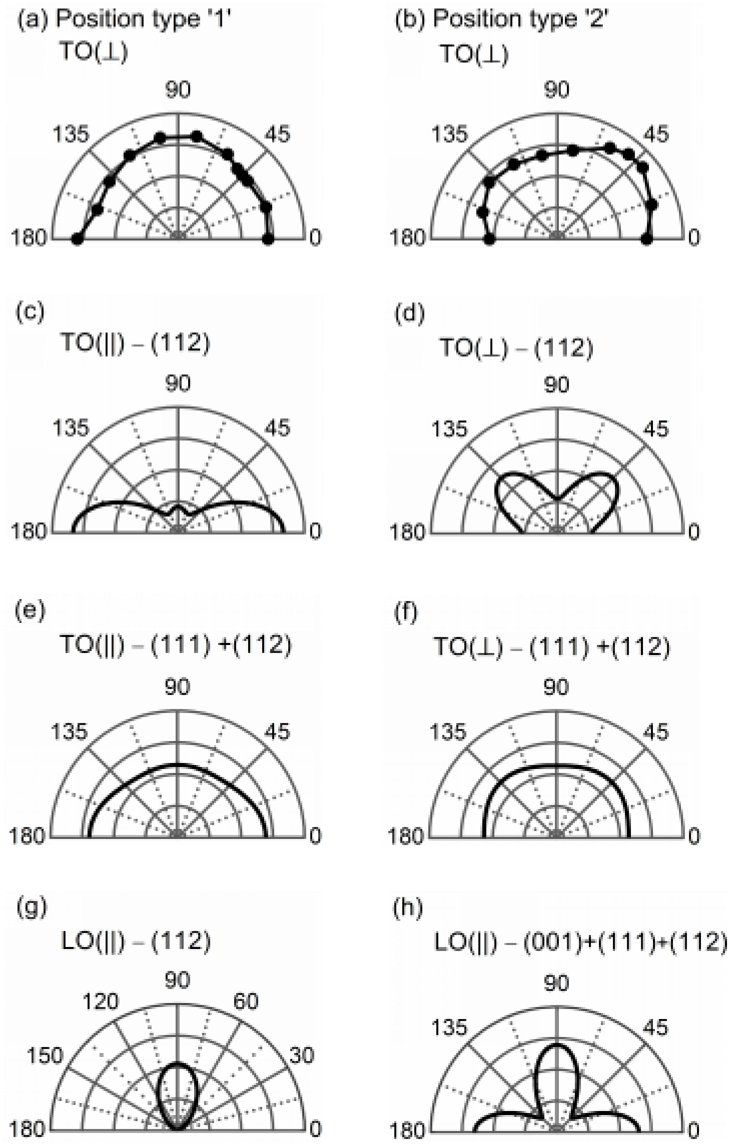

Fig. 4.3.6. *Observed polar Raman intensity dependence of TO phonon of GaP/Si(001) thick layer hetero-structure in cross polarization configuration, at spatial position (a) type '1' and (b) type '2'.Calculated azimuthal-angle dependence of TO phonon for Raman scattering from (112) facets in (c) parallel ($\mathbf{e}_i||\mathbf{e}_s$) configuration and (d) perpendicular ($\mathbf{e}_i\perp\mathbf{e}_s$) configuration. Simulated combinational polar Raman plot for scattering from (111) and (112) facets in (e) parallel and (f) cross polarization configurations. Calculated polar pattern of LO phonon in parallel configuration for Raman scattering from (g) (112) surface and (h) combination of (001), (111) and (112) facets.*

Among the possible crystallographic facets *e.g.*, {113}, {112} and {111}, the existence of {111} facets in epitaxially grown GaP/Si(001) TL hetero-structure is already established above via analyzing the polar dependence of the Raman scattering cross-section of optical phonons (Fig. 4.3.5). The deviation from circular symmetry, observed in polar intensity plots of TO phonon arising from position type '2' (Fig. 4.3.5(f) and Fig. 4.3.6(b)) may be associated with the existence of these higher-index planes like {112}, {113} etc. This consideration incited the examination of the scattering contributions from next higher-index facets {112}. As discussed earlier, the Raman tensors for (112) oriented crystal are evaluated by basis transformation, and consequently the intensity dependence of allowed TO and LO phonons on polarization rotation angle 'ϕ' is calculated using equations (4.4) and (4.5). The calculated polar Raman plots of TO phonon for scattering from (112) oriented crystal, in parallel and cross polarized configuration are illustrated in Fig. 4.3.6 (c) and (d), respectively. In the light of preceding discussion, the observed deviations in azimuthal dependence of the intensity of TO phonon from spatial position type '2' can now be elucidated by taking into account the contributions (with appropriate weighting factor) of (111) and (112) facets to Raman scattered intensity. Using equation (4.4) and (4.5), the expression for Raman scattered intensity of TO phonon from (111) and (112) planes is expressed as:

$$I_{TO(111)} \propto \left| \sqrt{\frac{2}{3}} d_{TO} \right|^2 \quad \hat{e}_i \parallel \hat{e}_s \tag{4.6}$$

$$I_{TO(112)} \propto \left| \sqrt{\frac{1}{3}} d_{TO} \sin(2\phi) \right|^2 + \left| \sqrt{\frac{1}{3}} d_{TO} \sin^2\phi - \frac{2}{\sqrt{3}} d_{TO} \cos^2\phi \right|^2 \quad \hat{e}_i \parallel \hat{e}_s \tag{4.7}$$

$$I_{TO(111)} \propto \left| \sqrt{\frac{2}{3}} d_{TO} \right|^2 \quad \hat{e}_i \perp \hat{e}_s \tag{4.8}$$

$$I_{TO(112)} \propto \left|\sqrt{\frac{1}{3}} d_{TO} \cos(2\phi)\right|^2 + \left|\frac{\sqrt{3}}{2} d_{TO} \sin(2\phi)\right|^2 \quad \hat{e}_i \perp \hat{e}_s \tag{4.9}$$

On summing the equations (4.6) & (4.7) and (4.8) & (4.9),

$$I_{TO(||)} \propto p.I_{TO(111)} + q.I_{TO(112)} \tag{4.10}$$

$$I_{TO(\perp)} \propto p.I_{TO(111)} + q.I_{TO(112)} \tag{4.11}$$

Using *p ~1*, *q ~0.15* in equations (4.10) and (4.11), the simulated combinational polar Raman plots obtained for parallel and cross configuration are shown in Fig. 4.3.6(e) and (f) respectively. This combination is decided by matching the distinctive shape of polar plots in Fig. 4.3.6(f) with that of Fig. 4.3.6(b). Furthermore, the corresponding combinational plot in Fig. 4.3.6(e) also resembles the observed polar dependence in Fig. 4.3.5(f), stemming from spatial position type ‘2’. On comparing Fig. 4.3.6(e) with Fig. 4.3.5(f), and Fig. 4.3.6(f) with Fig. 4.3.6(b), it is evident that observed deviation in circular dependence arising from spatial position of type ‘2’ (and ‘3’), can be explained consistently. For both parallel and cross polarization configurations, polar Raman intensity plots of TO phonon resulting from these position types can be elucidated, only if the contributions from higher-index (112) facets (although dormant) are taken into account. It can be noticed that the simulated (Fig. 4.3.5(h), Fig. 4.3.6(h)) and observed (Fig. 4.3.5(a),(b)) polar patterns of LO phonon for position type ‘1’ and ‘2’ are nearly similar, as expected, because of the dormancy of {112} facets. Thus, the observation of forbidden TO phonon and its spectral strength relative to allowed LO phonon of GaP/Si(001) thick layer hetero-structure can be consistently explicated to the scattering from higher-index {111} and {112} facets. Based on the values (*p~1*, *q~0.15*) of weighting factors in equation 4.10 and (4.11), the simulated percentage contribution of {111} and {112} facets (to TO phonon scattering) are ~85% (a=0.85) and ~15% (b~0.15) respectively. In order to estimate the accuracy of these parameters, we calculate the combined polar dependence (using equation 4.10) for different percentage combinations e.g., (75%, 25%)$_{\{111\},\{112\}}$ and (95%, 5%)$_{\{111\},\{112\}}$. The polar plots so obtained (Fig. 4.3.7) exhibit marked deviations from the observed (Fig. 4.3.5(f), Fig. 4.3.6(b)) and simulated (Fig. 4.3.6(e), Fig. 4.3.6(f)) patterns. This shows that simulated plots have an agreement of less than ±10% with the observed azimuthal dependence.

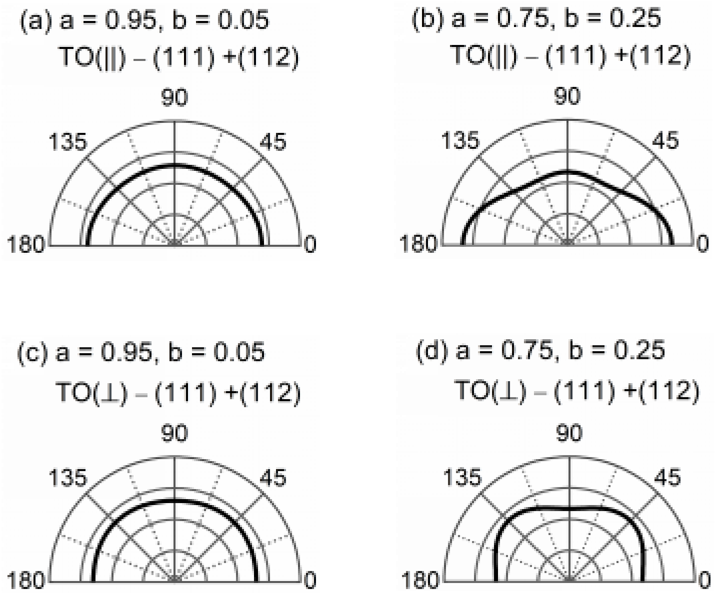

Fig. 4.3.7. *Calculated combined polar dependence of TO phonon for different percentage contributions of {111} and {112} facets in (a-b) parallel and (c-d) cross polarization configurations.*

Further, it should be noted that LO phonon is symmetry forbidden for back-scattering from {111} plane in cross polarization configuration. However, the observed azimuthal variation shown in Fig. 4.3.8(a) and (b) do have non-vanishing intensity at 0^0, 90^0 and 180^0 unlike the calculated polar Raman plot of LO phonon resulting from (001) (Fig. 4.3.8 (c)) and (112) (Fig. 4.3.8 (d)) planes in cross configuration. Despite this, it can be discerned From Fig. 4.3.8(a) and (b) that there is large reduction in peak intensity of LO phonon at these vanishing angles, which evinces the partial agreement with Raman selection rules. These non-zero contributions to LO phonon may also be related to approximate matching between simulated (Fig. 4.3.5(h), Fig. 4.3.6(h)) and observed plots (Fig. 4.3.5(a), (b)) of LO phonon in parallel configuration, as discussed above. The possible causes for this will be discussed later in this section. From calculation of polar dependence of optical phonons in cross polarization configuration, it is inferred that the LO phonon cross-section for scattering from (112) facets is much smaller (Fig. 4.3.8(d)) compared to that from (001) and (111) crystal planes, and therefore, its scattering contribution to the combined plot of LO phonon can be safely ignored.

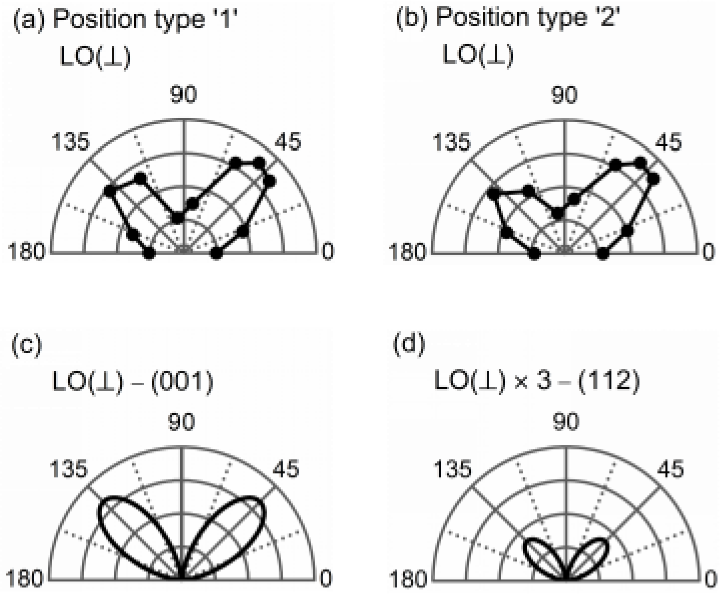

Fig. 4.3.8. *Observed azimuthal angle-dependence of LO phonon intensity of thick GaP epilayer in cross (*$\mathbf{e}_i \perp \mathbf{e}_s$*) polarization configuration, arising from the spatial position of (a) type ‘1’ and (b) type ‘2. Calculated polar pattern of LO phonon in cross polarization configuration for Raman scattering from (c) (001) facet and (d) (112) facet.*

Since the nucleation step critically affects the crystalline quality and morphology of overgrown layer, the formation of higher-index crystallographic facets in thick layer is expected to originate in the GaP/Si(001) nucleating layer. Therefore, to comprehend the origination of these higher-index facets, the GaP nucleating layer is also investigated by Raman spectroscopy. Figure 4.3.9(a) shows the typical unpolarized Raman map (from growth surface) of 5μm× 5μm region of NL hetero-structure. Three different kinds of Raman spectra arising from NL, exemplified by position types ‘1’, ‘2’ and ‘3’, are shown in Fig. 4.3.9(b).

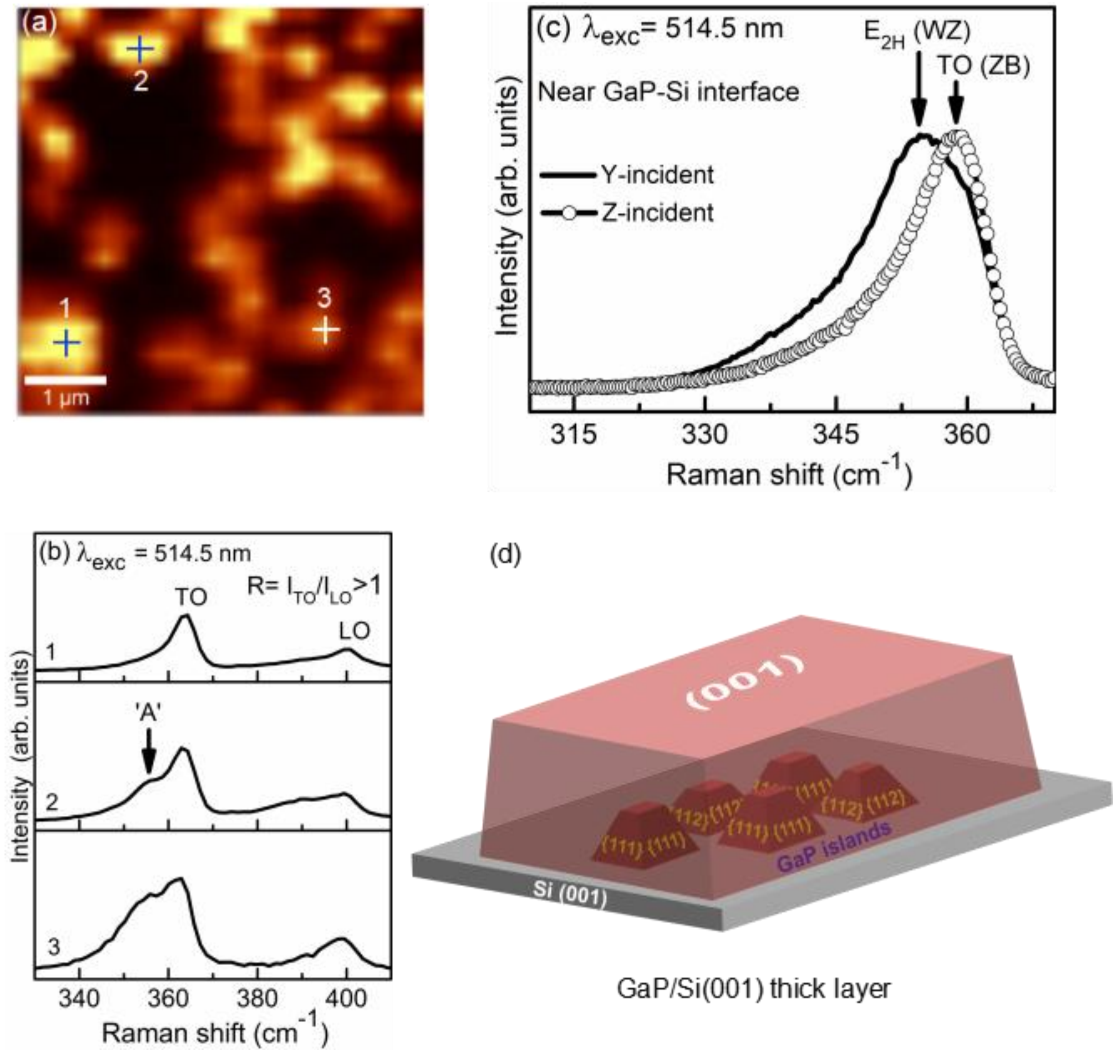

Fig. 4.3.9. *(a) Unpolarized Raman map of GaP/Si(001) nucleating layer obtained by integrating the intensity over the spectral range 330-410 cm^{-1} (b) observed Raman spectra from three different spatial positions (marked in (a)) across NL (c) Polarization dependent Raman spectra from near interface region of cross-sectional surface of thick layer hetero-structure, in Y-incident and Z-incident (where ‘Z’ is along the growth direction) polarization configurations (d) schematic diagram illustrating the nucleation of GaP islands terminating on higher-index {111} and {112} facets.*

Raman spectra stemming from spatial position of type ‘1’, characterize only the 10% of the mapped regions of NL, wherein both TO and LO phonon have weak asymmetric feature on their lower frequency side. Most of other spatial regions of NL records the Raman spectra of type ‘2’/’3’, having an additional phonon ~ 355 cm^{-1} (mode ‘A’) on low frequency side of TO mode. This additional mode exhibits spatial variation in its spectral weight *w.r.t.* that of TO phonon. Similarly, a strong feature on low frequency side of LO phonon can also be seen in Fig. 4.3.9(b). It is important to note that GaP Raman signal is not observed in the black regions of Raman spectral image shown in Fig. 4.3.9(a), which suggests that either growth of GaP has not occurred in these regions, or its thickness is too small to detect the Raman scattered light. Unlike TL hetero-structure, Raman map of GaP NL shows that peak intensity ratio $R = I_{TO}/I_{LO}$ is consistently larger than two for all the spatial positions. Such a large scattering contribution of symmetry forbidden TO phonon over the allowed LO mode, further strengthens the possibility of the existence of higher-index facets, as inferred in case of thick layer hetero-structure. Another noteworthy finding from Fig. 4.3.9(b) is that the phonon mode ~355 cm^{-1} (designated as phonon mode ‘A’ in Fig. 4.3.1), which is observed as an asymmetry (at red-shifted frequency) on low frequency side of TO phonon for TL, appears as a distinctive mode in Raman spectra of NL. This suggests that the phonon mode ‘A’, observed in Raman spectra (Fig. 4.3.1) of overgrowth layer, has the origin in the the GaP islands formed during the initial nucleation step and hence sited near the GaP-Si interface.

Pertaining to the origin of phonon mode ‘A’ observed ~355 cm^{-1}, it could be either DAZE TO phonon expected ~355-359 cm^{-1} or the E_{2H} phonon arising from WZ phase GaP. From the investigations on GaP/Ge(111) and GaP/Si(111) hetero-structures (chapter 3 and section 4.2), it can be recollected that E_{2H} phonon of WZ phase GaP is also expected ~355 cm^{-1}. The peak intensity ratio I_A/I_{LO} is greater than unity for most of the spatial positions across the NL. Also, the GaP LO phonon of NL has similar FWHM as that of GaP wafer. Therefore, the possibility of phonon mode ‘A’ being DAZE TO phonon is discarded. Subsequently, we examine whether this phonon stems from WZ crystal phase (E_{2H} mode) of GaP. Owing to the growth kinetics and small energy of transformation required, stacking sequence near the (111) facets of ZB phase GaP may change to that of (0001) facets of WZ GaP [49, 107, 109]. Existence of higher-index ZB {111} and {112} facets resulting in scattering contribution from symmetry forbidden TO phonon has already been established for TL hetero-structure. Furthermore, the AFM scan of NL in Fig 4.3.3(a) shows that GaP epilayer growth occurs in the form of nano-sized islands, making an angle of ~60°/40° with growth surface (001), which also indicates that these islands terminate on {111}/{112} facets. It is also known that atomic arrangement along (111) of ZB and (0001):c-plane of WZ crystal structures is similar. Thus, one can argue that there is a good probability for the observed mode ‘A’ being the WZ phase GaP phonon (E_{2H}), which may arise due to scattering from (0001) facets (c-plane).

In order to confirm that spectral feature ~355 cm^{-1} (mode ‘A’) is the E_{2H} phonon of WZ phase GaP, polarized Raman measurements from cross-sectional surface (CSS) of cleaved interface of GaP/Si(001) thick layer hetero-structure are performed. Figure 4.3.9(c) shows Raman spectra from near interface region of CSS of TL hetero-structure in *Y-incident* (both WZ and ZB modes expected to be dominant in intensity) and *Z-incident* (only TO phonon of ZB expected to have major contribution) [49] polarization configurations, where ‘Z’ is along the growth direction. Polarization dependence brings out differences in the lineshape of TO* (the combined [E_{2H} (WZ) + TO (ZB)]) phonon structure near interface in two chosen configurations, owing to different spectral weight of E_{2H} w.r.t. TO phonon and different Raman selection rules for these two modes. Further, TO* structure is red shifted in *Y-incident* configuration due to the stronger presence of E_{2H} (WZ) phonon in near interface region. However, the same TO* phonon structure emerging from the near surface region shows no change in both configurations, as there is dominance of ZB structure near the surface (section 4.2). This suggests that the mode ‘A’ is indeed the E_{2H} phonon, which arises due to formation of a WZ phase of GaP near the GaP-Si(001) interface. The comprehension is summarized in the schematic (Fig. 4.3.9(d)) of GaP/Si(001) TL. Figure 4.3.9(d) illustrates the evolution and contribution of higher-index {111} and {112} faceted micro/nano-structures (islands) resulting in the symmetry forbidden optical phonons in Raman spectra, with WZ/ZB stacking faults occurring along [111] direction. The presence of stacking faults can give rise to additional scattering contribution (for LO phonon), and consequently be responsible for the approximate agreement between simulated and observed azimuthal dependences of LO phonon, as discussed above. The determination of the contribution of LO phonon (including Frohlich-interactions) to {111} facets is more involved, since it arises from region having structural defects and major contribution is from the allowed part. This analysis could be attempted in future. However, since TO phonon is forbidden for back-scattering from (001) surface, its azimuthal-angle dependent behavior is more sensitive to presence of defect facets and thus provide the more clear picture of the same. This aspect of stacking fault and defect-exposed facets is further investigated using HRTEM, which is a standard technique to obtain this kind of information.

4.3.5 Cross-sectional HRTEM measurements

The findings of polarized Raman spectroscopy are further confirmed via cross-sectional high resolution transmission electron microscopy (HRTEM) study of GaP/Si(001) thick layer hetero-structure.

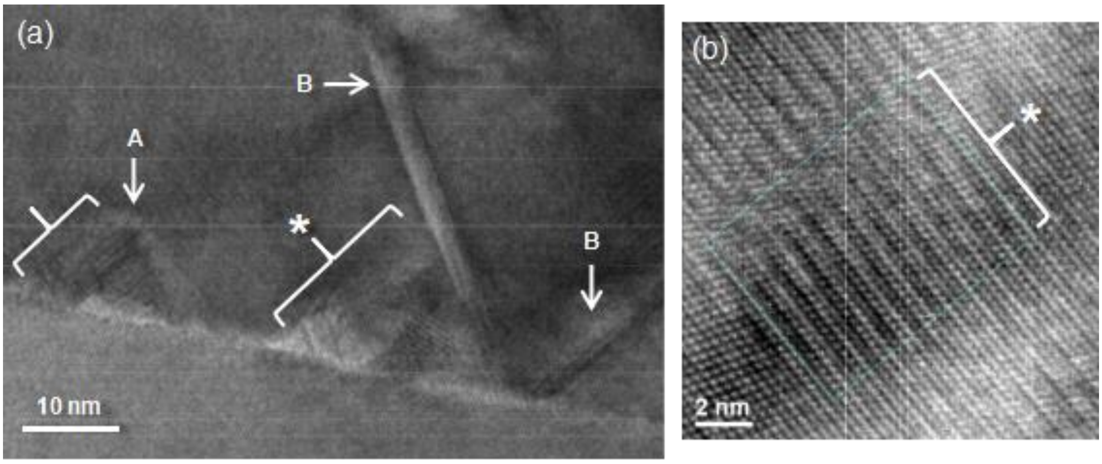

Fig. 4.3.10. *(a) Cross-sectional HRTEM image of GaP/Si(001) thick layer hetero-structure (b) Magnified HRTEM image of the triangular region shown in (a).*

Figure 4.3.10(a) shows the cross-sectional HRTEM image of the near-interface region of GaP/Si(001) thick layer hetero-structure. It can be observed from Fig. 4.3.10(a) that the triangular shaped islands (marked as 'A') formed near the GaP-Si interface, having different contrast than the surrounding, are terminating on higher-index {111} facets, as determined from interfacial angle (~55°) between growth plane and island facet. Similarly, the bright contrasting patch marked by 'B' in Fig. 4.3.10(a), extending deeper into the GaP layer, also subtends an angle of ~55° with the growth plane. These contrasting regions stem from the presence of crystal defects lying on {111} plane. The nature of these defects can be ascertained from the magnified (Fig. 4.3.10(b)) image of the region 'A' and 'B' in Fig. 4.3.10(a). Figure 4.3.10(b) clearly illustrates the presence of stacking faults along {111} direction, arising due to WZ discontinuity in predominant ZB lattice. The inter-planar spacing for these planes (Fig. 4.3.10(b)) also matches to that for {111} planes of GaP ZB crystal. Therefore, it can be inferred from HRTEM measurements that the structural defects (stacking faults) in GaP epilayer grown on Si(001) lie along {111} crystal planes, which is concurrent with the findings of azimuthal angle-dependent polarized Raman spectroscopy. This comparative study thus establishes one-to-one corroboration between Raman spectroscopy, an optical microscopy technique, and TEM which is an electron microscopy technique having angstrom level resolution, at least for III-V/Si and III-V/Ge hetero-structures.

4.4 Conclusion

As an extension of the results presented on polar/non-polar GaP/Ge(111) in earlier chapter, we have investigated closely lattice-matched and technologically important GaP/Si(111) hetero-structures. Spatially resolved wavelength dependent Raman and AFM measurements suggest that the observed in-plane spatial non-uniformity in strain is related to variations along the depth of GaP thick layer. This is substantiated further by sampling the cleaved cross-sectional surface of thick layer hetero-structure from near-interface to near-surface region, at a separation of ~100 nm. Raman sampling of cross-sectional surface revealed that presence of WZ phase near interface leads to differently strained regions of ZB GaP, with ZB region closer to interface being more strained due its proximity to dominant WZ phase. The ZB phase near surface is less strained, being away from WZ phase. Besides, Raman scattered intensity dependence of the optical phonons of GaP/Si(111) nucleating layer on the rotation of incident and scattered light polarization also endorses the dominance of WZ phase at the interface, which is consistent with topological features. We believe that these experimental findings open pathways for future investigations on the variation of optical, structural and physical attributes (crystal structure, crystalline quality, strain, etc.) along the depth of technologically important hetero-structures, using Raman spectroscopy.

Furthermore, the impact of substrate orientation on the nature of structural complexities, nucleating at hetero-polar interface, is ascertained through the investigation of GaP layers grown on Si(001) substrate. The unusual observation of symmetry forbidden TO phonon, having large Raman scattering cross-section, is analyzed by taking into account the crystallographic disorders and topographical variations in the GaP epilayer. Invariance of scattering cross-section of symmetry forbidden TO phonon along with the partial obeyance of allowed LO phonon RSRs, as observed in polarization dependent Raman spectral mapping, incites the azimuthal angle-dependent polarized Raman measurements. The spatially resolved polar Raman dependence of TO and LO phonon spectra in parallel and perpendicular polarization configurations is explicated to scattering contributions from locally present high index {111} and {112} defect facets in thick epilayer. These higher-index facets in overgrown layer stem from the coalescence of faceted islands formed during the initial nucleation as inferred via topographical mapping of nucleating layer. Also, the polarization dependent Raman measurements from cross-sectional surface of cleaved interface of thick GaP layer grown on Si(001), establish the WZ/ZB crystal phase coexistence with dominance of WZ phase near the interface. The intriguing presence of WZ phase in GaP/Si(001), is expectedto be the result of manifestation of stacking faults along the sets of thermodynamically favorable intermixed high-index <111> direction. The study proposes to establish that a versatile combination of Raman and AFM gives an immediate response to address the role of substrate orientation and hence the initial nucleation, on crystalline structure of GaP/Si(001) overgrowth layer. One-to one correlation studies based on Raman and HRTEM measurements further establish Raman spectroscopy as a non-destructive and non-cumbersome alternative to time-consuming HRTEM for understanding the structural properties of these hetero-structures.

Journal publications based on this chapter

1. Investigations on the origin of strain variation in the zinc-blende phase along the depth of GaP/Si(111) using spatially resolved polarized and wavelength dependent Raman spectroscopy, **R. Aggarwal**, A. A. Ingale and V.K. Dixit, *Appl. Surf. Sci.,* **2020**, 514, 145933(1)-145933(6).
2. Elucidating the interfacial nucleation of higher-index defect facets in technologically important GaP/Si(001) by azimuthal angle-resolved polarized Raman spectroscopy, **R. Aggarwal**, A. A. Ingale and V. K. Dixit, *Appl. Surf. Sci.,* **2021**, 554, 149620(1)-149620(10)

Chapter 5: Application of Raman spectroscopy for the reduction of defects in GaP/Si and GaP/Ge hetero-structures

5.1 Introduction and background

The central theme of the work presented in this chapter has evolved from the understanding developed in the previous two chapters, using Raman spectroscopy and atomic force microscopy (AFM). In earlier chapters, we have established the coexistence of wurtzite (WZ)/zinc-blende (ZB) GaP crystal phases and interfacial atomic-diffusion in GaP/Ge(111) hetero-structures. Further, strain distributed ZB phases along the depth and the nucleation of higher-index defect facets near the hetero-polar interface of GaP/Si have been discovered. Along with the impact of polar/non-polar epitaxy, the role of initial nucleation and growth kinetics in interfacial evolution and bulk-propagation of afore-discussed complexities has also been addressed through the exploration of surface topology and vibrational characteristics of nucleating layer. It is deduced that understanding the nature of nucleation and the growth of the initial few monolayers of polar GaP on non-polar Si and Ge is of utmost importance for improving the quality of actual structures. Since, the structure of the hetero-interface is expected to depend on the kinetics and chemical environment during initial growth, the nucleation stage of this two-step procedure plays the central role in controlling the defects generated at the polar/non-polar interface and hence in the overgrowth layer. Also, it has been reported that low temperature migration enhanced epitaxy fosters the charge neutral interface and the two dimensional growth of GaP on Si(001) [71]. In the absence of two dimensional nucleation, the polar nucleating layer growth occurs in form three-dimensional faceted islands and coalescence of these islands during the over layer growth results in the formation of structural defects like stacking faults and microtwins, as we have established in chapter 4. In such growth, the surface nucleation and kinetics play vital role in establishing the charge neutral interface and hence the two dimensional growth, by providing optimal mobility to adatoms and controlling their adsorption [15, 79] on substrate surface.

Taking these into consideration, efforts are made towards achieving the defect-reduced hetero-epitaxial integration of GaP on Si and Ge substrates. In order to realize this, the two-step MOVPE procedure for the growth of GaP/Si and GaP/Ge hetero-structures is adopted, in which the kinetics of the adatoms are further optimized by varying the growth temperature of the substrate. The growth temperature of the nucleating layer is controlled within a particular range, keeping other growth parameters nearly similar to those for previously grown hetero-structures.

5.2 New hetero-structures: Motivation and configuration

At temperatures below <~400°C, appropriate GaP nucleation sites favorable for two-dimensional growth may not be created owing to the low decomposition of Gallium precursor and reduced pyrolysis of phosphine under phosphorous rich conditions, thereby resulting in very low growth rate. Furthermore, phosphine does not pyrolyse largely even at ~425°C, which is compensated by high precursor flux V/III ratio adopted during the initial nucleation as in the case of previously grown hetero-structures. Also, we have already elucidated the defect-structures evolving near hetero-interface of GaP/Si and GaP/Ge overgrowth layer grown under nucleation at ~425°C. With this insight, the three new hetero-structures are grown by varying the nucleation temperature: (i) For set-I, nucleation temperature (T_n) is kept same as that for previously grown hetero-structures *i.e.*, T_{n1} ~425°C(ii) For set-II, sample is grown under nucleation at an incremental step of ~100°C *i.e.*, T_{n2} ~525 °C (iii) For set-III, the influence of high temperature on overgrowth layer quality is also examined by performing the nucleation at T_{n3} ~770°C.

In chapters 3 and 4 we have demonstrated, how Raman spectroscopy in combination with AFM can provide the immediate feedback on the nucleation of structural defects at the interface of polar/non-polar GaP/Si and GaP/Ge hetero-structures. Therefore, the role of nucleating layer in the GaP/Si and GaP/Ge hetero-structures is examined by analyzing the spectral features of the optical phonons of GaP, which can provide guidelines to achieve the optimized growth condition.

It has already been established in chapter 4 that the higher-index non-(001) crystal facets, bearing stacking faults, can be readily identified in GaP/Si(001) using angle-dependent polarized Raman measurements, through the analysis of the ratio of symmetry forbidden to allowed optical phonons. However unlike (001) oriented epitaxial layer, both TO and LO phonons are symmetry allowed in case of GaP(111) epilayer. Therefore, the identification of structural defects (higher-index defect facets) merely on the basis of the peak intensity ratio of TO and LO phonons requires the measurement of complete polar dependence of oscillator strength of optical phonons under different scattering configurations. Considering these complexities, we initially undertake the epitaxial growth and investigation of GaP layer grown on (001) oriented substrate. At first a nucleation layer of thickness ~60 nm is grown at the nucleation temperature in a horizontal metal organic vapor phase epitaxy reactor (AIX-200) at 20 mbar pressure. Thereafter, a GaP epi-layer of thickness ~500 nm is grown at a higher temperature (T_g ~770ºC) with V/III ratio ~100. The samples have been grown by our collaborator *Dr. V K Dixit* at *SML (MSS, RRCAT)*. A summary of the growth parameters of the samples is given in the Table 5.1.

Table 5.1. *Growth parameters of MOVPE grown GaP/Si(001) hetero-structures prepared under different nucleation temperatures.*

Sample	Step-I			Step-II		
	Nucleation temperature T_n (°C)	V/III ratio	Layer thickness	Thick layer growth temperature T_g (°C)	V/III ratio	Layer thickness (nm)
GaP/Si(001) (KS1)	~425	~1550	~60 nm	~770	~100	~500 nm
GaP/Si(001) (KS2)	~525	~1550	~60 nm	~770	~100	~500 nm
GaP/Si(001) (KS3)	~770	~1550	~60 nm	~770	~100	~500 nm

In order to avoid effect of pre-growth variations, growth of GaP nucleation layer on Si(001) substrate is also performed at same temperature (~425°C, hetero-structure KS1) as that in the previously grown epitaxial structures [79]. The GaP/Si(001) samples grown under kinetic controlled conditions are referred to as KS1, KS2 and KS3. In the following, we discuss the findings of Raman and AFM performed on these three hetero-structures.

5.3 Crystalline and surface properties

Crystalline and surface properties of hetero-structures are investigated by Raman spectroscopy and AFM. The measurements are performed using SPM integrated Raman system (*Alpha 300S*, WiTec, Germany) set-up described in chapter 2. Raman spectra are recorded in back-scattering geometry using 514.5 nm laser line. The wavenumber per pixel coverage of Raman spectrograph is ~0.5 cm^{-1} (514.5 nm). The spatial resolution at wavelengths of interest is ~1 μm. Laser power density at the sample surface is kept constant for all the Raman measurements presented.

5.3.1 Raman spectroscopy of GaP/Si(001) hetero-structures

Figure 5.1 shows Raman spectra of sample KS1 grown under low temperature nucleation (*i.e.*, previous growth conditions), in back-scattering geometry. Spatially resolved Raman spectra are acquired at numerous spatial positions on this sample. On the basis of variation in peak intensity ratio of TO and LO phonons *i.e.*, $R = I_{TO}/I_{LO}$, the observed spectra arising from the most of the regions are exemplified by positions '1' and '2' (Fig. 5.2).

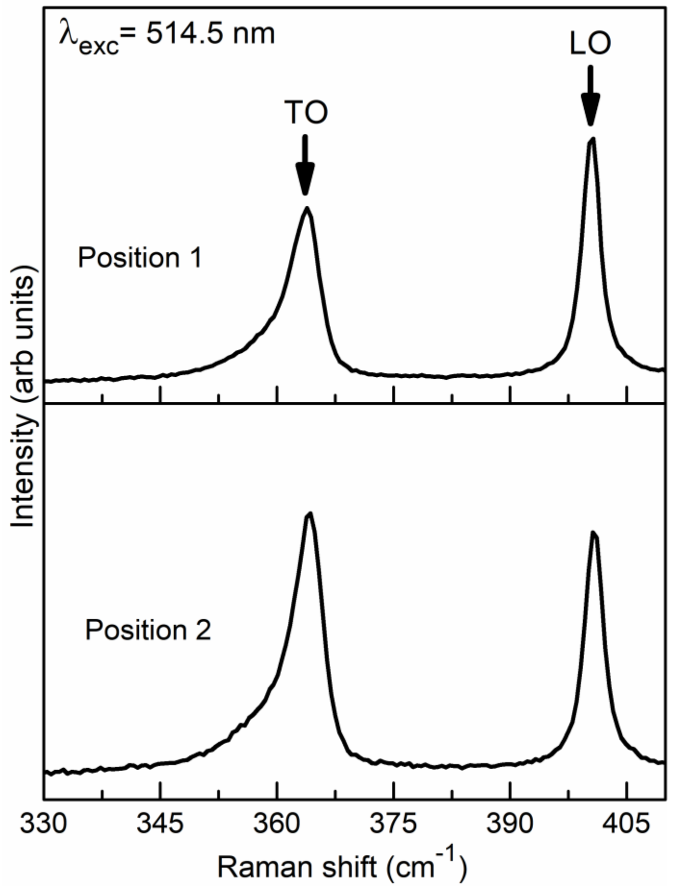

Fig. 5.1. *Raman spectra arising from two different spatial positions, typified by '1' and '2' on hetero-structure KS1.*

It can be observed that along with the allowed LO phonon, symmetry forbidden TO phonon of GaP having comparable spectral weight ($R = I_{TO}/I_{LO}$~1) is also present in both spectra. Also, TO and LO phonons are red-shifted (by ~1.5 cm^{-1}) w.r.t. the bulk

GaP wafer, suggesting the tensile strain in the grown layer. In resemblance to the previously grown GaP/Si(001) sample as discussed in chapter 4 (section 4.3), the peak intensity ratio '*R*' is either less than or near the unity, showing position dependent variations. For most of the regions of the sample KS1, the ratio '*R*' is near unity. The origin of symmetry forbidden TO is attributed to the scattering contributions from higher-index defect facets {111} and {112}, as explained in chapter 4.

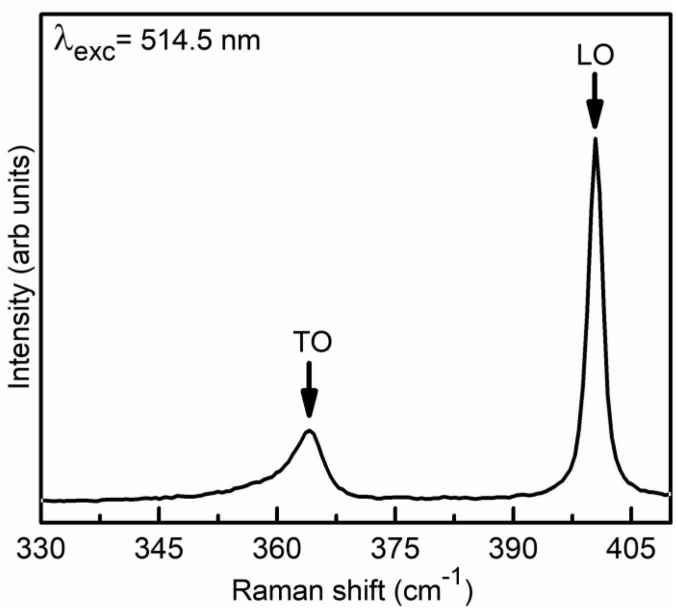

Fig. 5.2. *Raman spectra of hetero-structure KS2, grown under intermediate (T_{n2} ~525°C) nucleation temperature.*

Furthermore, the crystalline quality of GaP layer is almost similar to that of previously grown sample, as evidenced from the FWHM ~3.5 cm^{-1} of LO phonon. However, for hetero-structure KS2, the peak intensity ratio (*R*) of TO-to-LO phonon is significantly less (~0.2) than unity for most of the regions on the sample as seen in spatially resolved Raman measurements (Fig. 5.2) performed over the sample. This shows that in sample KS2, the density of defect facets (and stacking faults) giving rise to forbidden TO phonon is decreased substantially as compared to KS1. In addition, the observed FWHM of GaP LO phonon is ~2.2 cm^{-1}, showcasing the considerable improvement in crystalline quality of KS2 over KS1, as a consequence of the reduced density of defect facets. Another intriguing feature of KS2 is that it exhibits the similar red-shift in GaP optical phonons as that for KS1.

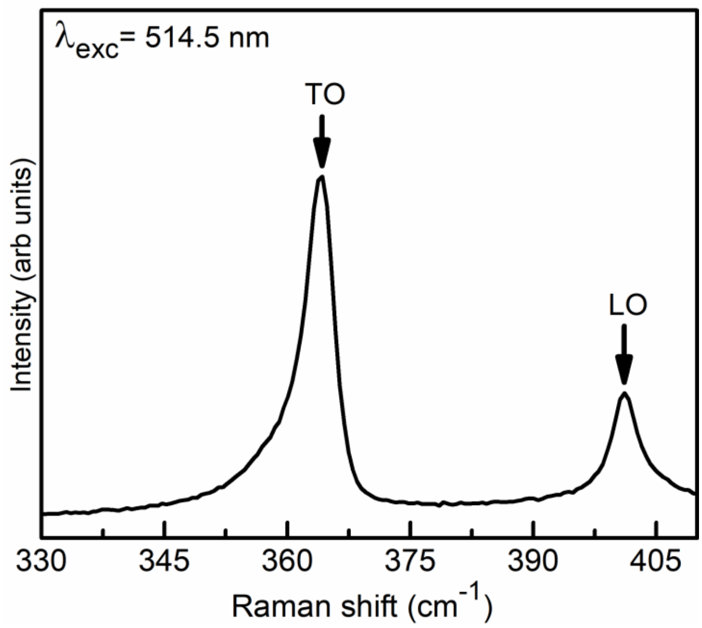

Fig. 5.3. *Raman spectra of hetero-structure KS3.*

Figure 5.3 shows Raman spectra stemming from GaP layer of hetero-structure KS3 grown under nucleation at higher temperature T_{n3} ~770°C. The spectral weight of the symmetry forbidden TO phonon is considerably increased ($R = I_{TO}/I_{LO}>2$), and is much greater than the allowed LO phonon over the entire region of sample KS3. In conformity with the results obtained in chapter 4 (section 4.3), this occurs due to higher density of structural defects lying on higher-index crystal facets {111} and {112} in hetero-structure KS3, compared to that in KS1 and KS2. Raman spectra show that the further acceleration of growth kinetics of the nucleating layer results in the broadened (FWHM ~4.5 cm^{-1}) GaP LO phonon of KS3, evidencing the deterioration in crystalline quality of overgrown layer. This finding is consistent with large TO-to-LO phonon peak intensity ratio ($R = I_{TO}/I_{LO}>2$). Thus, from Raman spectroscopy measurements on samples KS1, KS2, and KS3, it is evident that the impact of growth kinetics on the nucleating layer is the basis to control the structural defects.

The study shows that the understanding developed in chapter 4 enables us to use even the basic Raman spectroscopy for improving the hetero-polar epitaxial integration, and extract important and in-depth information on grown hetero-structures. Raman spectroscopy of three GaP/Si(001) samples KS1, KS2 and KS3 reveal that hetero-structure KS2 grown at intermediate nucleation temperature has the superior crystalline quality. In the following, we discuss the investigations on the surface characteristics of hetero-structures KS1, KS2 and KS3 using optical and AFM imaging.

5.3.2 AFM measurements on GaP/Si(001) hetero-structures

Before, getting into the quantification of surface properties, we examine the optical micrographs (Fig. 5.4) of these three hetero-structures KS1, KS2 and KS3, in order to obtain a general overview of surface characteristics.

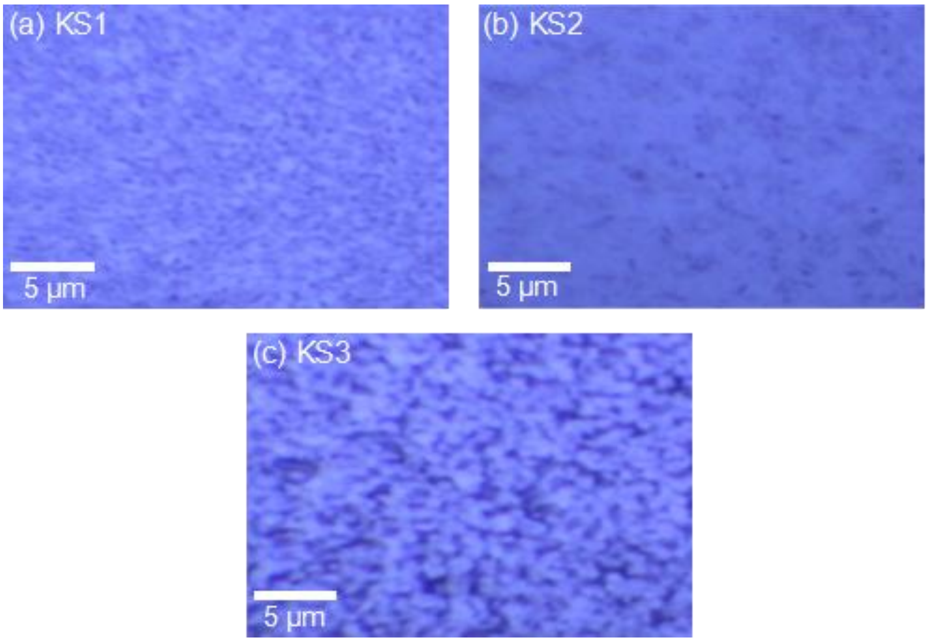

Fig. 5.4. *Optical images of three hetero-structure samples, (a) KS1 (b) KS2 and (c) KS3.*

Optical images in Fig. 5.4 reveal that GaP epilayer of KS2 exhibits a smoother surface with minimum surface undulations, in contrast to sample KS1 and KS3. From Fig. 5.4(c), it is apparent that the surface of GaP epilayer of hetero-structure sample KS3 has the greater degree of unevenness as compared to KS1.

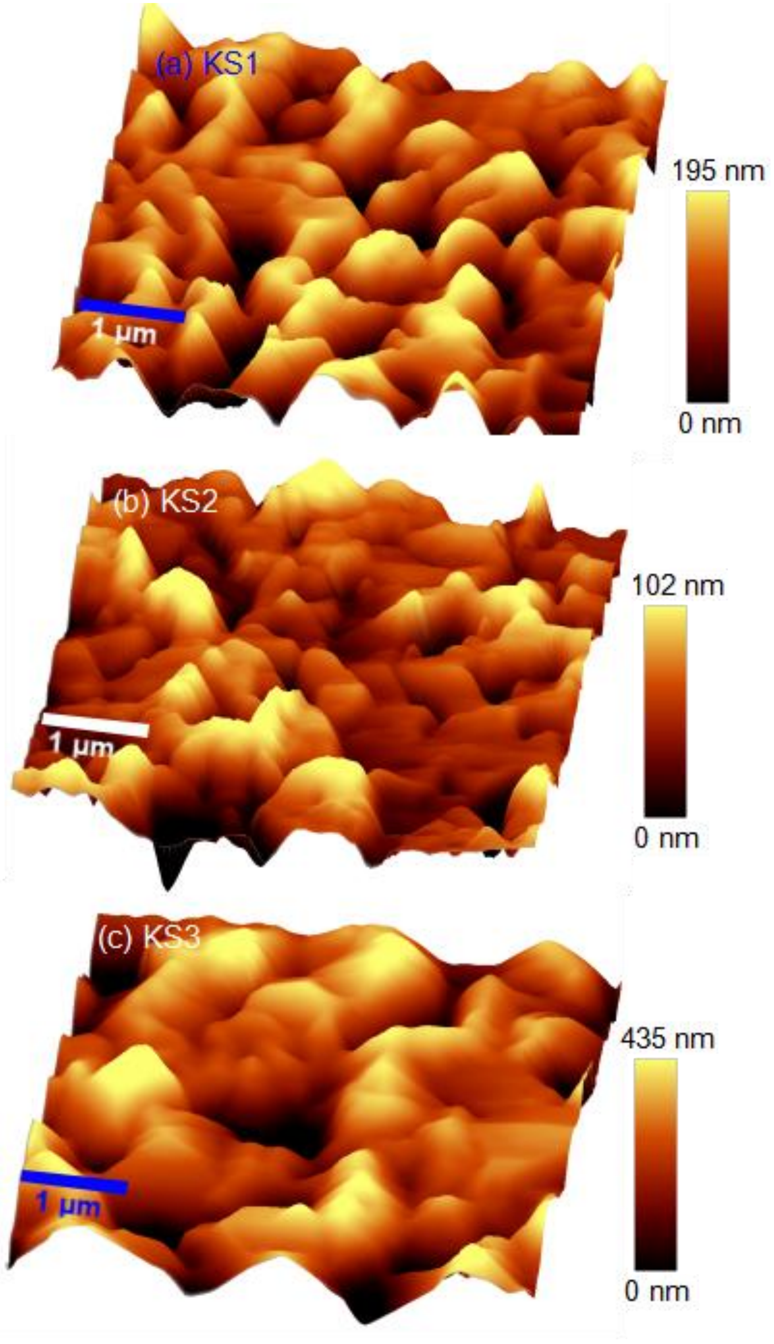

Fig. 5.5. *AFM scans of hetero-structure (a) KS1 (b) KS2 and (c) KS3.*

Furthermore, the AFM map of sample KS1 in Fig. 5.5(a) consistently shows that overgrowth GaP layer is characterized by significant surface undulations and high surface roughness (~55 nm r.m.s.). However, the nucleation at ~525°C followed by high temperature fill layer epitaxy results in much smoother (roughness ~25 nm r.m.s.) surface features as evident from AFM map in Fig. 5.5(b). In agreement with optical images, the hetero-structure KS3 (Fig. 5.5(c)) is characterized by much higher surface roughness (~120 nm r.m.s.) as compared to KS1 and KS2.

5.3.3 Raman spectroscopy of GaP/Si and GaP/Ge(111) grown under intermediate nucleation temperature

Following the results on kinetics-controlled growth of GaP/Si(001), the epitaxial integration of GaP thick layer (~560 nm) is subsequently performed on (111) oriented Si and Ge substrates by emulating the nucleation conditions of hetero-structure KS2. Figure 5.6(a) and (b) show the Raman spectra of GaP/Si(111) and GaP/Ge(111) thick layer (~560 nm) hetero-structures respectively, grown under intermediate (~525°C) nucleation kinetics. Similar to hetero-structure KS2, both TO and LO phonons of GaP are red-shifted (by ~1.5 cm^{-1}) w.r.t. bulk GaP wafer values. The FWHM of LO phonon of both GaP/Si(111) and GaP/Ge(111) epilayers is ~2.6 cm^{-1}. This suggests that the crystalline quality of these layers is remarkably improved over the previously (FWHM ~4.0 cm^{-1}) grown samples, wherein the GaP structures were nucleated at ~425°C. These observations are consistent with that of hetero-structure KS2, and thus establish that the nearly continuous GaP overgrowth epilayers, having much smoother uniform surface morphology and upgraded crystalline quality, can be grown under intermediate nucleation temperature ~525°C.

From chapter 4, it can be recalled that GaP/Si(111) hetero-structure grown under identical growth conditions as that of KS1 features the coexistence of WZ/ZB crystal phases of GaP with WZ phase extending up to surface layer. Similar to earlier grown samples, an asymmetric feature on lower wave-number side of TO phonon is present in Raman spectra of these newly grown GaP/Si and GaP/Ge hetero-structures also. Therefore, the presence of WZ phase (if any), which occurs as discontinuity to the thermodynamically favorable ZB crystal phase of GaP, is analyzed in freshly grown GaP/Si(111) sample.

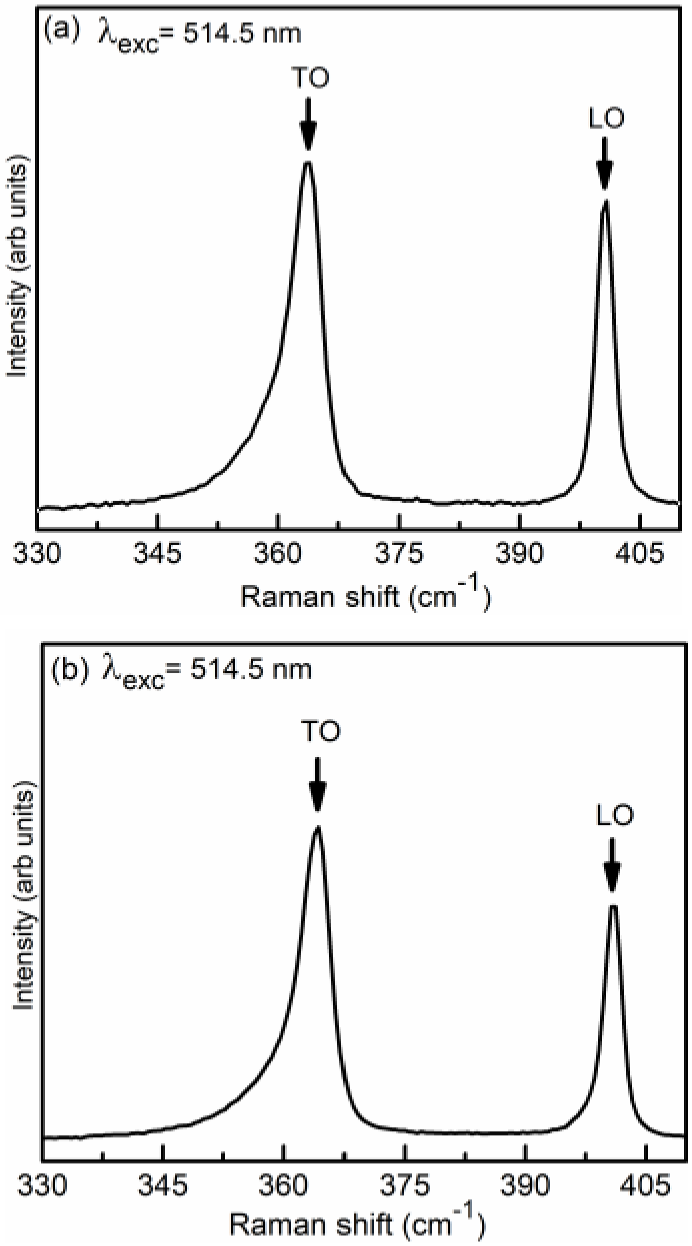

Fig. 5.6. *Raman spectra of (a) GaP/Si(111) and (b) GaP/Ge(111) hetero-structures grown under same kinetics as the hetero-structure KS2.*

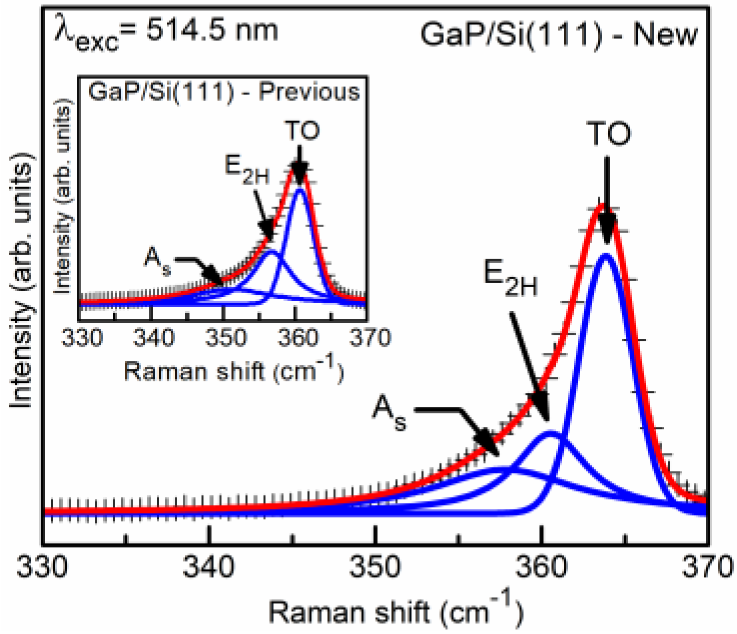

Fig. 5.7. *Deconvolution of phonon contributions to Raman spectra of GaP/Si(111) in TO phonon spectral range, using minimum required Lorentzian and Gaussian line-shapes (blue). Red color line shows total fit to data (+).*

To comprehend the relative dominance of WZ/ZB crystal polytypes in freshly grown GaP/Si(111), its TO phonon envelope is deconvoluted as shown in Fig. 5.7. Apart from the inherent asymmetric feature (A_s) and TO phonon arising from ZB phase GaP, the additional mode ~360 cm^{-1} (Fig. 5.7) is also observed. This additional feature (~360 cm^{-1}) is expected to be the E_{2H} phonon of WZ phase GaP. However, in contrast to the deconvolution fit (Inset of Fig. 5.7) of earlier hetero-structure, the peak intensity ratio of E_{2H}-to-TO phonon is smaller, as evident from the Fig. 5.7. This demonstrates that relative content of WZ and ZB in GaP/Si(111) hetero-structure, grown under controlled nucleation kinetics (T_{n3} ~525°C), is lower than that in earlier samples. Similar deconvolution analysis has been performed for Raman spectra arising from many other spatial locations on GaP/Si(111), which is consistent with Fig. 5.7. This further substantiates that newly grown GaP epilayers posses significantly superior crystalline features.

This study systematically addresses the role of surface kinetics in nucleation and bulk-propagation of structural defects in epitaxially grown GaP/Si and GaP/Ge hetero-structures. Keeping other processing parameters *e.g.*, precursor flux ratio and pre-growth substrate preparation method nearly same, the migration and adsorption of adatoms, which play the crucial role in the formation of interface during the initial growth and structure of subsequent epilayer, is critically influenced by nucleation temperature. At low temperatures (below <~400°C), GaP growth rate is significantly reduced due to very low decomposition of trimethyl gallium and phosphine in this temperature range. Phosphine does not pyrolise significantly large even at nucleation temperature ~425°C, used for previous growth, and this is counterbalanced by maintaining high V/III ratio (~1725/1550) during initial nucleation. Also, we discussed in chapter 3 (section 3.3) that elemental diffusion causing cross-doping effects is substantially diminished at low temperatures. However, for high temperature (~770°C) nucleation, there would be uncontrolled migration and desorption of adatoms due to breakage of less-stable Ga-Si and even the stronger P-Si bonds, which is expected to result in formation of largely separated three-dimensional islands. When, subsequent GaP epitaxial growth is performed on such a nucleation layer during step-II, there occurs the coalescence of these three-dimensional faceted islands, leading to the formation of structural defects e.g., stacking faults, microtwins and anti-phase boundaries. The overgrowth layer, thus formed, has highly roughened surface morphology as evident from Fig. 5.5(c). In the view of this, the optimization of growth kinetics, particularly the pivotal nucleation step, was planned by increasing it in a small incremental step of ~100°C. At the intermediate nucleation temperature (~525°C) which is favorable for sufficient decomposition of gallium precursor precursor under phosphorous rich conditions, there occurs the optimal mobility and controlled adsorption of the Ga and P adatoms. This, possibly, gives rise to nearly charge-neutral interface and hence much smoother, defect-reduced GaP epilayer as evident from Fig. 5.4(b) and Fig. 5.5(b). This suggests that in order to suppress the formation of structural defects at the hetero-polar interface, one needs to optimize the nucleation temperature in such a way that precursor decomposition, adatoms migration to optimal sites and diffusion across hetero-interface occur in counterbalanced manner. The understanding and generalization established from Raman spectroscopy can provide the timely inputs for controlling the nucleation kinetics and other growth parameters, thereby controlling the interface-originated defect-structures. This will lead to the efficient integration of III-V compound semiconductors on technologically important Si and Ge substrates.

5.4 Conclusion

Based on findings of earlier chapters, the efforts are made towards achieving the defect-reduced hetero-epitaxial integration of polar GaP on non-polar group IV substrates, by applying the Raman spectroscopy. Thick GaP epilayers grown via a two step MOVPE procedure on Si(001) substrate under varied nucleation kinetics (~425°C, ~525°C and ~770°C), keeping the overgrowth layer temperature (~770°C) same, have been investigated using Raman spectroscopy and AFM. The nucleation sites created using continuous epitaxy at lower (~425°C) and higher (~770°C) temperatures results in highly roughened GaP epilayers with large density of interface-originated structural defects, as inferred from Raman spectroscopy. Interestingly, the GaP fill epilayer deposition atop the nucleating layer grown at intermediate (~525°C) temperature results in much flatter and uniform surface features, and the significant suppression of interfacial defects as deduced from the Raman and AFM measurements. The intermediate nucleation conditions extrapolated to epitaxy of GaP on Si(111) and Ge(111) substrates, consistently yields the high-quality GaP epilayers having the reduced density of WZ discontinuity in predominant equilibrium ZB crystal phase of GaP. It is worth noting that although the type of defects are different in GaP epilayer grown on Si(001) and Si, Ge(111) substrates, they feature similar trend in optimal growth conditions. This suggests that structural intricacies originate from *i.e.*, polar/non-polar (hetero-polar) growth, although its manifestations are different for different orientations of growth template. Findings of this study further suggest that suitable mobility and controlled adsorption of the Ga and P atoms on substrate surface at intermediate nucleation temperature fosters the nearly charge-neutral interface during the growth of initial few monolayers, which results in nearly two-dimensional and defect-reduced GaP epilayers.

These findings advance Raman spectroscopy as an expeditious alternative to other standard techniques e.g., *in situ* reflection anisotropy spectroscopy and HRTEM measurement, for the optimization of pivotal nucleation step and actual growth. This may also be implemented to other III-V polar semiconductors for high-quality and efficient monolithic integration of devices on existing Si and Ge technology.

Chapter 6: Conclusion and future outlook

6.1 Summary of the thesis work

The work presented in this thesis is principally motivated with the necessity to understand nature and origin of structural complexities associated with epitaxial integration of polar III-V compound semiconductors on non-polar group IV substrates using a contact-less, nondestructive and relatively expeditious optical technique *i.e.*, Raman spectroscopy. A way further, atomic force microscopy (AFM) is coupled with Raman spectroscopy measurements to explore into the correlation between the vibrational signatures and surface topology of grown epilayer. Furthermore, the results of Raman spectroscopy measurements are also substantiated by high resolution transmission electron microscopy (HRTEM) study of hetero-structures. In order to combine the best of both *i.e.*, III-V compound semiconductors and group IV substrates for technological and economical interests, the hetero-polar epitaxial integration of GaP on Si and Ge is undertaken. The interest in studying the structural and topographical intricacies is driven by the fact that they determine the functional properties of opto-electronic devices based on these technologically significant GaP/Si and GaP/Ge hetero-structures. Effect of polar/non-polar and lattice mismatch, surface energy and growth kinetics on crystalline (structural), physical, physico-chemical and surface properties of these hetero-structures is investigated. The Nucleating (~60 nm) and thick (~820 nm) layer GaP/Ge(111), GaP/Si(111) and GaP/Si(001) hetero-structures for this investigation are grown (Collaborator: Dr. V. K. Dixit, SML, RRCAT) by MOVPE technique using a two step approach. The nucleation layer for each of these hetero-structures is investigated to comprehend the role of nucleating surface on the growth and properties of overgrown thick GaP layer.

In the beginning, GaP epilayer grown on Ge(111) substrate is investigated to delineate the role of large lattice-mismatch and hetero-polar interface in determining the properties of combined structure. The lack of sufficient reports on the study of GaP-on-Ge material combination was another driving force for addressing these hetero-structures first. Until the investigations presented in this thesis, very few reports existed on GaP/Ge hetero-structures, and these reports discuss about the charge transport and electronic band alignment behavior of GaP/Ge hetero-junction [26, 95]. Probing deeper, sub-micron level strain variations in the grown epilayers are discovered and determined by spatially resolved Raman spectroscopy. The origin of additional spectral feature in the TO phonon band, and its correlation with surface topology is investigated by same-site Raman spectroscopy and scanning probe microscopy measurements. It is shown that unique conjunction of AFM and Raman mapping performed on the same sites gives a cutting-edge to the analysis of micro/nano-structured epilayer, while advancing the understanding of the origin of additional phonon mode/s. The inferences of this combinational study effectuated the spatially resolved polarization dependent Raman spectroscopy of the cross-sectional surface of hetero-structures. Spatially resolved polarized measurements enabled the revelation of the coexisting structural allotropes of GaP, with predominance of wurtzite (WZ) phase in proximity to the hetero-junction interface and that of zinc-blende (ZB) phase near the surface. The additional asymmetric feature in TO phonon envelope is shown to stem from the wurtzite phase of GaP. This study based on Raman spectroscopy is the first direct experimental evidence for the occurrence of thermodynamically less favorable wurtzite phase at the GaP/Ge(111) interface.

Furthermore, physico-chemical aspects of GaP/Ge hetero-interface governed by growth kinetics, precursor flow rate and phosphine passivation are investigated. It is observed that Ge-optical phonon mode of underlying substrate of nucleating layer is anomalously broadened and softened. Using wavelength dependent Raman spectroscopy, the cause of this peculiar effect is elucidated in terms of the occurrence of shallow inter-diffused Ge layer (thickness ~20 nm) underneath the GaP epilayer nucleated at ~425°C under high V/III (~1725) ratio. From thermal treatment of hetero-structures and qualitative evaluation of probable mechanisms responsible for inter-diffusion, it is established that vacancy mediated diffusion of phosphorous in Ge substrate give rise to disordered shallow layer of Ge in the close vicinity of GaP-Ge hetero-interface. The result bears particular importance as it signifies that growth challenges for polar/non-polar epitaxy can be resolved by diffusing the phosphorous in group IV substrates for nucleation, and growth of actual structures can be performed after desorption of phosphorous at high temperature.

Following the thread of findings on GaP/Ge(111), we then examined the technologically important and closely lattice-matched GaP/Si(111) material combination wherein hetero-polarity is expected to be the key determinant of the structural aspects of epilayer. Significant spatial non-uniformity in strain and crystalline quality of grown layer is corroborated with variations along the depth of hetero-structure by spatially resolved- and wavelength dependent-Raman measurements from growth surface. Strain-distributed zinc-blende GaP phases are discovered along-the-depth of hetero-structure via nanometer-scale (~100 nm) spatially resolved Raman sampling of cross-sectional surface. These variations in physical properties are analyzed to originate from the deeply co-existing wurtzite phase GaP along the depth of hetero-structure. It is found that the ZB crystal in proximity to WZ phase, having predominance near the hetero-interface, is additionally strained. The co-dominance of wurtzite phase is further substantiated by polarization dependent Raman spectroscopy and AFM study of nucleating layer. The experimental findings manifest the effective implementation of Raman spectroscopic tool for resolving and probing the sub-micron level variation of physical, structural and optical properties *e.g.*, strain, crystal structure, crystalline quality, etc., even along the depth of hetero-structures. In order to delineate the impact of interplay between hetero-polarity and surface energy on nucleation during initial stages of epitaxy, surface properties and polytypic behavior, the work is extended to the investigation of GaP layer grown on (001) oriented Si substrate, another most widely used Si wafer in micro-electronic processing. The emergence of symmetry forbidden TO phonon of GaP is examined using polarize Raman imaging and AFM, which helped in realizing the contribution of non-(001) crystal facets to Raman scattering. The mechanisms responsible for significantly large scattering cross-section of forbidden optical phonon are identified with locally existing higher-index {111} and {112} defect facets using azimuthal angle-resolved polarized Raman spectroscopy. It is revealed that the orientation moderated coalescence of faceted micro/nanosized islands crystallized in nucleating layer results in the structural defects lying on energetically favorable higher-index planes in overgrowth layer. Furthermore, highly intriguing WZ/ZB crystal phase coexistence in the vicinity of GaP-Si(001) interface is inferred via Raman spectroscopy of cross-sectional surface under carefully chosen polarization configurations. It is further substantiated via cross-sectional HRTEM that WZ/ZB stacking faults along nearly indistinguishable $(111)_{ZB}/(0001)_{WZ}$ planes gives rise to forbidden and additional spectral features in the Raman spectra. The novel implementation of angle-dependent polarized Raman spectroscopy elevates this optical technique to a different level for determining the orientation of defect-exposed facets in other advanced semiconductor hetero-structures.

Based on Raman spectroscopy and AFM study of GaP/Si(001), it is ascertained that initial nucleation plays the key role in evolution and bulk propagation of structural defects in the thick epilayer grown atop the nucleated surface. Eventually, the two step MOVPE growth of GaP layer on Si and Ge substrates is undertaken afresh by tweaking the kinetics of the nucleation in controlled manner in a well-thought-out temperature range. Using the understanding developed on earlier hetero-structures, and through the application of Raman spectroscopy, it is shown that nucleation at intermediate (~525°C) temperature results in nearly two-dimensional and high crystalline quality overgrowth layer with reduced density of defect facets and WZ discontinuity in equilibrium ZB phase of GaP. It is understood that the kinetics-controlled mobility and adsorption of adatoms on growth template influences the charge-neutrality along interface and hence the nature of growth and crystalline properties of epilayer.

We could thus resolve the sub-micron length scale defect-structures nucleating at the hetero-polar interface and their propagation into the overgrown epitaxial layer via innovative applications of a fully optical technique *i.e.*, Raman spectroscopy, which was the primary motivation behind this thesis. Crystalline and surface properties of these hetero-structures are shown to follow the thread of interplay between hetero-polarity, lattice mismatch, surface energy and growth kinetics. The information thus extracted from Raman spectroscopy in conjunction with AFM can be used as an immediate feedback for the improvement of hetero-interface/s of the epitaxially integrated structures. The study proposes Raman spectroscopy and its variants as non-invasive, non-destructive and expeditious alternative to time-consuming and cumbersome HRTEM/*in situ* reflection anisotropy spectroscopy measurements for probing the surface and interface properties of such hetero-structures.

6.2 Future work

During the course of work presented in this thesis, the efficacy of a purely optical technique in comprehending the nature of interface-originated defect structures, which control the functional properties of GaP/group-IV hetero-structures, is established. As a logical outcome of the present study, the succeeding experimental work would involve to further establish the one-to-one correspondence between Raman spectroscopy and HRTEM. This will establish Raman spectroscopy as a standard and expeditious methodology to obtain important information on hetero-structures as well as in their evaluation for device fabrication. Another future study could be to ascertain the nature and orientation of interfacial defect-structures in GaP/Si and GaP/Ge hetero-structures grown under kinetically controlled growth conditions, by angle-resolved polarized Raman spectroscopy. This would be beneficial for gaining further insight into the role of nucleation kinetics on surface reconstructions at hetero-polar interface so that hetero-structures with enhanced functionality could be designed.

No other Information to be provided In this file.

Thesis Highlight

Name of the Student: Rahul Aggarwal

Name of the CI/OCC: RRCAT, Indore **Enrolment No.:** PHYS03201404005

Thesis Title: Raman spectroscopy study of epitaxially integrated polar GaP on non-polar Si and Ge substrates

Discipline: Physical Sciences **Sub-Area of Discipline:** Raman and scanning probe microscopy

Date of viva voce: 19/07/2021

The best of both the GaP and group IV (Si, Ge) semiconductors for technological and economical interests can be combined through their epitaxial integration, and tremendous efforts are being made for many years to realize this. However, the high-quality epitaxial integration of III-V compound semiconductors (*e.g.*, GaP) on Si and Ge substrates unavoidably poses challenges due to polar/non-polar interface, lattice mismatch and diffusion at the hetero-interface. In this work, a novel approach towards Raman spectroscopy technique in conjunction with AFM has been employed to investigate bulk, crystallographic morphed surfaces and interfaces of epitaxially grown GaP/Si and GaP/Ge hetero-structures.

Through uniquely employed co-localized Raman-AFM and spatially resolved polarized Raman measurements from cross-sectional surface, it is discovered that the wurtzite/zinc-blende crystal phase co-existence at GaP-Ge interface results in additional phonon modes in Raman spectra of GaP/Ge(111) epilayer. Also, the atomic inter-diffusion across the GaP-Ge hetero-interface has been elucidated via wavlength dependent Raman spectroscopy. Further, the one-of-a-kind application of spatially resolved Raman spectroscopy from cross-sectional surface of GaP/Si(111), has enabled the detection of nanometer scale (~100 nm) variations along the depth of hetero-structure. This novel methodology has successfully resolved the structural allotropes and strain distributed zinc-blende GaP phases along the depth of GaP/Si(111) hetero-structure. A complex azimuthal-angle dependent polarized Raman spectroscopy is applied creatively to determine orientation of energetically favorable and defect-exposed higher-index {111} and {112} crystal facets in GaP/Si(001), and thereby the origin of symmetry forbidden and additional phonons of GaP epilayer. To the best of our knowledge, this is first of its kind study on hetero-structures. The inferences made from this study are extrapolated to actualize the integration of new GaP/Si and GaP/Ge hetero-structures having far superior surface and crystalline quality. This study establishes a purely optical technique, *i.e.*, Raman spectroscopy as a standard and expeditious methodology to obtain important information on III-V/group-IV and other advanced hetero-structures as well as in their evaluation for device fabrication.

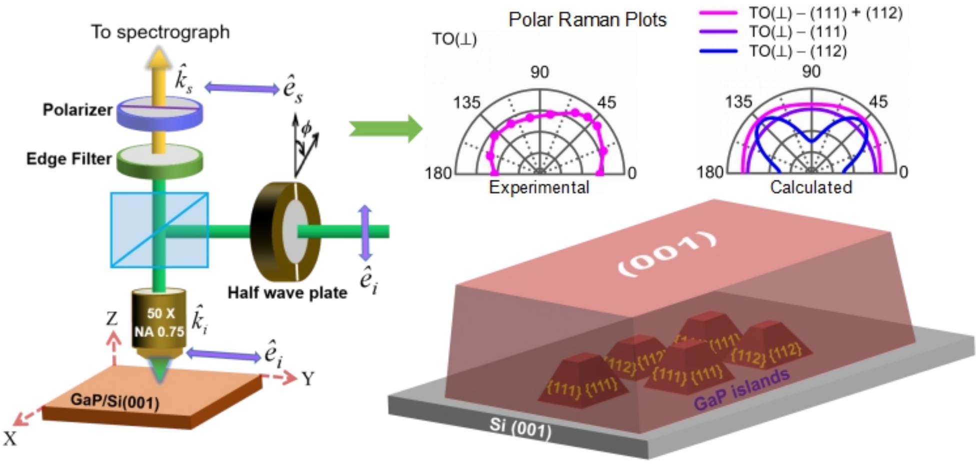

Figure 1. *Azimuthal angle-resolved polarized Raman spectroscopy facilitates the understanding of interfacial nucleation during initial stages of epitaxial growth, and the structural intricacies of overgrowth layer.*